The North Sistan orogen (Eastern Iran): Tectono-metamorphic evolution and significance within the Tethyan realm

Michael Jentzer, Philippe Agard, Guillaume Bonnet, Patrick Monié, Marc Fournier, Hubert Whitechurch, Jafar Omrani, Mohammad Hossein Zarrinkoub, Mohammad Mahdi Khatib, Reza Kohansal, et al.

Gondwana Research

The Sistan orogen (Eastern Iran): Tectonic evolution and significance within the Tethyan realm

--Manuscript Draft--

Manuscript Number:	
Article Type:	GR Focus, Review Article
Keywords:	Sistan, metamorphic sole, obduction, pull apart, Iran, ophiolite
Corresponding Author:	Michael Jentzer, PhD. Sorbonne Université Campus Pierre et Marie Curie: Sorbonne Universite Campus Pierre et Marie Curie paris, FRANCE
First Author:	Michael Jentzer, PhD.
Order of Authors:	Michael Jentzer, PhD.
	Philippe Agard
	Guillaume Bonnet
	Patrick Monié
	Marc Fournier
	Hubert Whitechurch
	Jafar Omrani
	Mohammad Hossein Zarrinkoub
	Mohammad Mahdi Khatib
	Reza Kohansal
	Damien Do Couto
	Camille Godbillot
	Dia Ninkabou
Abstract:	The N-S trending Sistan belt (E Iran) stretches N-S along ~700 km, at a high angle compared to the other Alpine-Himalayan ranges found along the Neotethyan suture zone. The aim of this study is to reappraise both the tectonic evolution of the Sistan orogen and its significance within the Neotethyan realm. The Sistan ophiolite, which started forming since 125 Ma, exhibits all the characteristics of present-day (ultra-)slow spreading environments. Closure of the Sistan ocean occurred through a major NE-dipping subduction zone active at least since 90 Ma, as indicated by (i) the location and age of bimodal juvenile arc magmatism, (ii) the regular SW vergence of the orogen and (iii) the location and age of subducted fragments. The discovery of 74-72 Ma metamorphic soles (~750°C-0.65 GPa) at the base of the ophiolite argues for the initiation of an intra-oceanic thrust/subduction zone, which ultimately led to the SW obduction of the ophiolite onto the Lut Block (mostly over by 50 Ma). Subsequent collision was marked by a drastic change of the Eocene sedimentation yet by only moderate shortening until the Oligocene (~30-40 km). Since the Late Miocene, post-collisional deformation appears strongly controlled by far-field stresses emanating from the Zagros collision. Given its orientation, petrological characteristics and age, the Sistan ocean probably opened as an independent pull apart basin along an inherited transform fault. The Sistan ocean also appears to have recorded the major geodynamic events which accompanied the closure of the Neo-Tethys, i.e. the major change in kinematics at ~90 Ma and the northward migration of India at ~75-70 Ma.
Suggested Reviewers:	Jean Pierre Burg jean-pierre.burg@erdw.ethz.ch
	Federico Rossetti federico.rossetti@uniroma3.it

	Ali Mohammadi ali.mohammadi@erdw.ethz.ch
	G.R. FOTOOHI RAD gfotohi@yahoo.com
	Andréa Zanchi andrea.zanchi@unimib.it
Opposed Reviewers:	

The Sistan orogen (Eastern Iran):

Tectonic evolution and significance within the Tethyan realm

Michael Jentzer[1], Philippe Agard[1], Guillaume Bonnet[1], Patrick Monié[2], Marc Fournier[1], Hubert Whitechurch[3], Jafar Omrani[4], Mohammad Hossein Zarrinkoub[5], Mohammad Mahdi Khatib[5], Reza Kohansal[4], Damien Do Couto[1], Camille Godbillot[1], Dia Ninkabou[1]

[1]*Sorbonne Université, CNRS, Institut des Sciences de la Terre de Paris (iSTeP), 4 place Jussieu 75005 Paris, France*

[2]*Université de montpellier, Géosciences montpellier, place Eugène Bataillon 34095 Montpellier France*

[3]*Université de Strasbourg, Ecole et Observatoire des Sciences de la Terre, Institut de Physique du Globe, Institut de Géologie, 1 rue Blessig, 67084 Strasbourg, France*

[4]*Geological Survey of Iran, Mehraj Bd., Tehran, Iran*

[3]*Department of Geology, University of Birjand, University Bd., Birjand, Southern Khorasan, Iran*

Abstract

The N-S trending Sistan belt (E Iran) stretches N-S along ~700 km, at a high angle compared to the other Alpine-Himalayan ranges found along the Neotethyan suture zone. The aim of this study is to reappraise both the tectonic evolution of the Sistan orogen and its significance within the Neotethyan realm. The Sistan ophiolite, which started forming since 125 Ma, exhibits all the characteristics of present-day (ultra-)slow spreading environments. Closure of the Sistan ocean occurred through a major NE-dipping subduction zone active at least since 90 Ma, as indicated by (i) the location and age of bimodal juvenile arc magmatism, (ii) the regular SW vergence of the orogen and (iii) the location and age of subducted fragments. The discovery of 74-72 Ma metamorphic soles (~750°C-0.65 GPa) at the base of the ophiolite argues for the initiation of an intra-oceanic thrust/subduction zone, which ultimately led to the SW obduction of the ophiolite onto the Lut Block (mostly over by 50 Ma). Subsequent collision was marked by a drastic change of the Eocene sedimentation yet by only moderate shortening until the Oligocene (~30-40 km). Since the Late Miocene, post-collisional deformation appears strongly controlled by far-field stresses emanating from the Zagros collision. Given its orientation, petrological characteristics and age, the Sistan ocean probably opened as an independent pull apart basin along an inherited transform fault. The Sistan ocean also appears to have recorded the major geodynamic events which accompanied the closure of the Neo-Tethys, i.e. the major change in kinematics at ~90 Ma and the northward migration of India at ~75-70 Ma.

Keywords

Sistan, metamorphic sole, obduction, pull apart, Iran, ophiolite

1. Introduction

The dominantly E-W trending Alpine–Himalayan mountain belts formed as a result of the long-lived convergence between Eurasia and continental fragments derived from Gondwana. Two main sutures (Figs. 1a, b) outlined by ophiolite belts, high-pressure low-temperature metamorphic relics, magmatic arcs or flexural basins, stand out in this superorogenic complex: (1) a northern suture marking the former location of the Paleotethys ocean, which opened in the Early Devonian and disappeared through N-dipping subduction below Eurasia from the Upper Carboniferous onwards, leading to continental collision in the Late Triassic (e.g. Dercourt et al., 1986; Boulin, 1991; Besse et al., 1998; Stampfli and Borel, 2002; Richards and Şengör, 2017; Barrier et al., 2018); (2) a southern suture marking the former location of the Neotethys ocean, which formed on the northern edge of Gondwana in the Upper Carboniferous or Early Permian, when the Paleotethys ocean was still several thousand km wide (Stampfli and Borel, 2002; Torsvik, 2016). Closure of the Neotethys, through N-dipping subduction below Eurasia, started during the lowermost Jurassic and was followed by collision during the Tertiary (e.g., during the Eo-Oligocene along the Zagros transect; e.g. Berberian and Berberian, 1981; Dercourt et al., 1986; Sengor et al., 1988; Stampfli and Borel, 2002; Agard et al., 2011; Barrier et al., 2018; Burg, 2018).

In detail, however, many issues remain unresolved, such as (i) the precise location of each suture, most markers being discontinuous; (ii) the diachronicity of tectonic events along strike of the same ocean (Stampfli and Borel, 2002); (iii) the exact number of sutures (e.g., Metcalfe, 2013); (iv) the exact number of intervening blocks and their lateral relationships (van Hinsbergen et al., 2012). In particular, the respective location and geometries of the so-called Cimmerian continental blocks, which lied between the two Tethyan oceans after the opening of the Neotethys and before the final closure of the Paleotethys, are fraught with large uncertainties.

These inferred blocks are separated by ophiolite belts, mostly Mesozoic in age, found outside of the two main E-W Tethyan sutures (Figs. 1a, b). These ophiolite belts have commonly been interpreted as marginal basins opened within the upper plate of the Neotethys subduction system but their geodynamic evolution, initial location, spatial extension and mutual relationships are still outstanding questions.

Within this framework, Iran lies in a central position and is one of the best places to constrain Tethyan convergence (Figs. 1), for which contrasting tectonic reconstructions were published (e.g. Berberian and King, 1981; Dercourt et al., 1986; Saccani et al., 2010; Agard et al., 2011; McQuarie and van Hinsbergen, 2013; Ajirlu et al., 2016; Richards and Sholeh, 2016; Barrier et al., 2018; Bonnet et al., 2020), and to assess the significance of its many ophiolite belts (e.g., Nain-Baft, Sabzevar; Torbat-Heydarieh; Sistan; Jaz Murian; Moghadam and Stern, 2015 and references therein).

The Sistan orogen contains an extensive ~700 km long ophiolite belt and is located halfway between the Zagros and Himalayan orogens. It separates the Afghan and Lut continental blocks and appears most intriguing with its north-south orientation (Figs. 1; 2). It is also the only orogen located at the rear of an active subduction system, namely the Makran subduction zone (where the last fragments of Neotethys are presently disappearing; Figs. 1b). The seismically active Sistan orogen was first surveyed in the late 1970s through pioneering geological studies (Tirrul et al., 1983) but never comprehensively studied since.

The aims of the present contribution are to refine our present understanding of the Sistan orogeny and its bearing on the history and geodynamic processes accompanying Tethyan convergence. To this aim we provide (i) detailed cross-sections distributed across the northern sector of the Sistan belt, merged into a first synthetic structural map and crustal scale cross-section and (ii) tectono-metamorphic and geochronological constraints on the poorly studied ophiolite domain and the eastern edge of the Lut block. These observations are combined with

existing magmatic and metamorphic data for the Sistan suture zone (including some recently published by this group; Jentzer et al., 2017, 2020; Bonnet et al., 2018) into 2D lithospheric scale geodynamic reconstructions of the Sistan realm. This study shows, in particular, that the Sistan orogen (1) preserves a large obducted ophiolite with so far unreported metamorphic soles that was only mildly affected by later collision and (2) represents a landmark at the crossroads between the Zagros and Himalayas, recording all the major tectonic events occurring to the East and West of the Neotethys ocean.

2. Geological setting of the Sistan orogen

2.1.Overall architecture

2.1.1. Main geological domains (as defined by Tirrul et al., 1983)

The Sistan belt was mapped at the 1:50.000 scale as part of an extensive regional mapping and mineral exploration program with the Geological and Mineral Survey of Iran. Based on lithostratigraphic (15 logs) and tectonic (three local cross-sections) investigations, Tirrul et al. (1983) recognized five main domains (Figs. 2b):

– (1) The Lut Block to the W and (2) the Afghan Block to the E, characterized by Neoproterozoic to Paleozoic basement. The youngest sediments deposited on top of this basement prior to the Sistan orogeny are mildly deformed Jurassic series and Early Cretaceous (Barremian-Aptian) Orbitolina limestones.

– (3) The Neh Complex, which comprises Aptian to Albian ophiolites and ophiolitic mélanges together with sedimentary rocks of Senonian age, both assumed to be weakly metamorphosed.

– (4) The Ratuk Complex, characterized by the presence of highly deformed, ophiolitic mélange and metasediments locally metamorphosed under HP-LT conditions.

– (5) The Sefidabeh basin overlying both the Ratuk and Neh complexes, which consists of Senonian to Eocene turbiditic sequences and was interpreted as deposited in a fore-arc basin.

2.1.2. Geophysical constraints on the deep structure

Gravimetric data suggest that the Moho depth reaches up to ~52 km below the Sistan orogen. This is slightly deeper than the 40 to 45 km depth reported everywhere else in the adjacent Lut, Tabas, Yazd and Central Iran continental blocks composing the Central East Iran Microcontinent (Figs. 2a; Mousavi and Ebbing, 2018; Eshagh et al., 2019). In contrast, the lithosphere appears to be relatively thin below Sistan, as shown by two independent approaches: (1) heat flow measurements higher than 100 mWm^{-2} (i.e. above the average 67 mWm^{-2} value for continental domains; Davies, 2013; Lucazeau, 2019); (2) inversion of magnetic data, which allows to estimate the 580°C isotherm Curie depth at ~48 km in this area. (Mousavi and Ebbing, 2018).

2.2. Main tectonic events from the Mesozoic onwards

The main tectonic stages which affected the Sistan domain since the Mesozoic, which comprise all the steps of a single Wilson cycle (see Fig. 3), are briefly described here. They will be further discussed below in the light of our results.

2.2.1. Rifting and spreading stages

The onset of rifting of the Sistan ocean is ill-constrained but spreading is attested from the mid-Cretaceous onwards (Figs. 3): K-Ar dating on amphiboles from oceanic gabbros in the ophiolites yield an Aptian age of 124 ± 11 Ma (Delaloye and Desmons, 1980), while U-Pb dating of zircons from oceanic leucogabbros yield Albian ages between 107 ± 1 and 113 ± 1 Ma (Zarrinkoub et al., 2012a). This is coeval with deposition of the Orbitolina limestone in the Lut and Afghan blocks. Biostratigraphic dating of radiolarites deposited on ophiolitic material yield Upper Aptian to Lower Albian ages (Babazadeh and De Wever, 2004;

Ozsvárt et al., 2020), in agreement with isotopic dating. These authors inferred that the rifting of the Sistan ocean started during the Lower (to Middle) Cretaceous.

Petrological and geochemical studies on the ophiolite (Delaloye and Desmons, 1980; Moazzen et al., 2006; Saccani et al., 2010; Zarrinkoub et al., 2012a) show that its mantle section mostly consists of harzburgite (less than 5% of clinopyroxene), affected by variable degrees of serpentinisation. The crustal section dominantly comprises N-MORB gabbros and basalts and rarer E-MORB basalts, respectively attributed to ridge-type magmatism (~5-20% partial melting of DMM) and to an environment where the DMM is mixed with an enriched source (e.g., interaction with a hot-spot; Saccani et al., 2010). Less common mafic rocks bear calc-alkaline series with diagnostic enrichment in LREE, negative anomalies in Nb, Ta suggesting a supra-subduction origin. Contrasting degrees of partial melting of the mantle have been proposed: based on the Cr# [Cr /(Cr+Al)] of spinel in peridotite, Moazzen et al. (2006) inferred it to be high, possibly advocating for fast spreading, whereas based on geochemical modelling Saccani et al. (2010) and Zarrinkoub et al. (2012a) proposed an intermediate to low degree of partial melting.

Berberian and Berberian (1981) proposed that the Sistan basin opened as a back-arc basin above the retreating Zagros subduction zone of the Neo-Tethys ocean, which was still active at that time (Agard et al., 2011). The paleogeographic orientation of the Sistan ocean is still largely speculative, however, ranging from N100 to N160°E (e.g. Saccani et al., 2010; Barrier et al., 2018).

Paleomagnetic data on the Central East Iran Microcontinent (CEIM; Davoudzadeh et al., 1981; Soffel and Förster, 1984; Soffel et al., 1996; Besse et al., 1998; Mattei et al., 2012, 2015; Figs. 3) show that (1) before the opening of the Sistan ocean, the Yazd, Tabas and Lut blocks experienced a homogeneous counter-clockwise rotation of about ~65° between the Upper Triassic and the Middle Jurassic, suggesting that these blocks formed

a single microcontinent at that time; (2) a ~30° counter-clockwise rotation of the CEIM between the Upper Jurassic and the Upper Cretaceous which could be due to the Sistan rifting-spreading formation and propagation.

2.2.2. Subduction stages

Subduction of oceanic lithosphere is attested by the presence of high-pressure low-temperature metamorphic rocks (HP-LT) in the Ratuk complex (Tirrul et al., 1983), which constrain the location of the Sistan suture zone (Figs. 2b, c). Peak P-T conditions for eclogites range between 1.9-2.4 GPa and 435 -650°C (Fotoohi Rad et al., 2005; Angiboust et al., 2013). Most recent estimates point to a relatively cold subduction thermal regime (~7°C/km; Bonnet et al., 2018). Retrograde P-T conditions were estimated from 0.5 to 0.8 GPa and between 470 and 530°C (Angiboust et al., 2013; Kurzawa et al., 2017; Bonnet et al., 2018).

Bröcker et al. (2013) used three methods to date the HP-LT metamorphic rocks along the Ratuk complex: (1) Rb-Sr on phengite, glaucophane, omphacite, biotite, epidote, garnet, albite and garnet from eight samples yield ages between 87.1 ± 0.3 and 84.9 ± 0.6 Ma for the mineral assemblages near the eclogitic peak, while retrograde assemblages yield a younger age at 78.9 ± 0.5 Ma; (2) ^{40}Ar-^{39}Ar plateau ages on five samples, which range between 87.6 ± 0.6 and 81.3 ± 1.3 Ma; and (3) U-Pb on zircons from four samples, which yield ages between 89.3 ± 1.6 and 86.1 ± 1.1 Ma. Bonnet et al. (2018) provided fourteen Ar-Ar ages on phengite and amphibole ranging from 88.4 ± 0.35 to 83.81 ± 0.94 Ma without significant difference between near peak and retrograde assemblages. Most authors agree on an age of peak burial of the eclogites at 86 ± 3 Ma. Somewhat older Ar-Ar ages on phengite and amphibole (between 139 ± 19 Ma and 116 ± 19 Ma; Fotoohi Rad, 2009) were interpreted to result from excess Ar (Bröcker et al., 2013).

Thick deposits of Senonian flysch also imply the presence of a highly subsiding basin, probably related to the existence of a nearby subduction zone (Tirrul et al., 1983). Last, low-K

calc-alkaline magmatic rocks intruding or interbedded with the Senonian flysch, and capped by the Paleocene reef of the Sefidabeh basin, were shown to correspond to subduction-related juvenile arc magmatism (Jentzer et al., 2020). In the same location, Jentzer et al. (2020) described high-silica adakites, producted with a component of slab melting. These authors argued for NE-dipping subduction of the Sistan ocean beneath the Afghan margin since the Turonian (i.e., after ~93 Ma). Subduction polarity has been the matter of debate, however, with authors arguing for either east- (Tirrul et al., 1983) or west-dipping subduction zone (Pang et al., 2013; Boskabadi et al., 2020; Ozsvárt et al., 2020).

2.2.3. Collisional stages

Coarse grained proximal molasse-type Eocene sediments overlying earlier flysch deposits are thought to postdate ocean closure and to constrain the onset of collision between the two continental blocks. Based on unconformities Tirrul et al. (1983) identified two stages of deformation during the Eocene. Eocene deformation is sealed by unconformable, less deformed Oligocene deposits.

Voluminous, mildly deformed syn- to post-collisional Paleogene magmatism cuts across the Lut block and part of the Sistan orogen (Camp and Griffis, 1982; Figs. 2b; 3). Ar-Ar age constraints for these magmatic rocks span from the Mid-Eocene (ca. 46 Ma) to the Lower Oligocene (ca. 25 Ma). This magmatism has been interpreted as the result of the delamination of the lithospheric root following collision (e.g.: Pang et al., 2013; Mohammadi et al., 2016; Omidianfar et al., 2020).

2.2.4. Post collisional stages

Paleomagnetic data suggests that since the Miocene another ~35° counter-clockwise rotation affected the CEIM (Soffel et al., 1996; Mattei et al., 2015). The main horizontal stress rotated around 60° counter-clockwise, probably due to the increasing influence of the “hard” collision in the Zagros (Jentzer et al., 2017 and references therein). The Sistan

orogen is still tectonically active, as shown by several morphologic indicators (e.g., shifts of river waterways) and by instrumental seismicity and paleoseismicity studies of strike-slip faults. The dominant set of active faults comprise N-S right-lateral faults and their conjugate left-lateral NW-SE-trending reverse faults (Berberian et al., 2000; Walker and Khatib, 2006), which are compatible with a N025 orientation of the main horizontal stress (Jentzer et al., 2017). These strike-slip faults also act as major pathways for upper Cenozoic intraplate post-collisional alkali-basalts (ca. 27 to 2 Ma, K-Ar or Ar-Ar dating on whole rocks; Camp and Griffis, 1982; Walker et al., 2009; Pang et al., 2012). This alkaline magmatism has been interpreted as deriving from an asthenospheric upflow following lithospheric delamination (Pang et al., 2012).

2.3. Major unknowns and detailed objectives of this study

Our current knowledge of the Sistan orogen suffers from at least two major unknowns:

(1) Several first-order questions regarding the tectonic evolution of the Sistan orogen are still a matter of debate, including: (i) the determination of the ocean type, ranging from fast to (ultra) slow spreading ocean; (ii) the timing of closure of the ocean basin, during the Upper Cretaceous or the Paleogene, as well as subduction polarity (i.e. NE- or SW-dipping, or both); (iii) the process allowing the emplacement and preservation of the (presumably) unmetamorphosed Neh ophiolite; (iv) the onset (during the Paleocene or Eocene) and termination of collision, the amount of overall shortening and extent of deep basement thrusting (i.e., thin- or thick-skin tectonics). To that end, the architecture and structural relationships of the main domains (Neh complex, Ratuk complex and Sefidabeh basin) need to be refined.

(2) The paleogeography of the Sistan within the Tethyan framework requires further investigations to assess its orientation and potential relationships with nearby marginal basins such as Sabzevar, N-Makran and/or Ras Khoh.

The present study aims at addressing the first set of questions by focusing on dedicated areas (Figs. 2c; 4) and using two major approaches: (1) structural investigation of each domain to constrain their organization and the overall present-day architecture of the Sistan orogen and (2) a metamorphic and geochronologic approach to further characterize the Neh complex and constrain its emplacement as well as metamorphism of the eastern margin of the Lut block.

3. Structural map of Sistan

Regional mapping of the northern part of the Sistan orogen was conducted in 1977 and 1978 by the Geological Survey of Iran (together with the Bureau de Recherches Géologiques et Minières). Results are published in the 1:250 000 scale maps of Qayen, Shahrakht, Birjand, Gazik, Dehsalm and Zabol (and three detailed reports for Qayen, Shahrakht and Gazik). The corresponding 1:100 000 scale maps were published during the 1990's.

We have combined the six 1:250 000 scale maps of the North Sistan belt to produce a comprehensive and homogeneous map (Figs. 4a). To improve readability, some simplifications and specific groupings were necessary:

– All ultramafic rocks (dunite, harzburgite and lherzolite) and their altered or metasomatized products (serpentinite and listvinite), magmatic rocks representing the crustal section of the Sistan ocean (gabbro, basalt and spilite, dolerite and plagiogranite) and ocean floor, deep-sea sediments (radiolarites, phyllites and pelagic carbonates), together with what is mapped as "colored mélange" were merged into what is referred to here as ophiolite.

– Magmatic rocks are shown by age (e.g., Precambrian, Jurassic and Early Cretaceous) except for Tertiary magmatism, which had to be grouped since ages proposed for the same formation on neighbouring maps do not allow to be more precise. In

addition to the volcanic and plutonic rocks, volcano-sedimentary rocks like tuff, volcanic breccia, and ignimbrite have been associated to this group.

– Sedimentary rocks are shown by age. The rare Oligocene and Miocene outcrops were merged because they are mainly continental deposits (red beds and conglomerates) difficult to date accurately.

– Metamorphism is indicated by hatching. Due to the lack of data, metamorphic facies cannot be indicated, except for the more extensively studied HP-LT metamorphism of the Ratuk complex.

This map highlights three main gaps in the knowledge of the structure of Northern Sistan, as defined by Tirrul et al. (1983): (1) the boundary between the Sistan suture zone and the Afghan Block, originally defined by the western extension of the Barremian-Aptian Orbitolina limestone, must be refined due to the discontinuity of the Orbitolina limestone outcrops; (2) despite the sub-division of the Sistan suture zone into three mains units, the relationship between the Neh and Ratuk complexes or the extension and structural position of the Sefidabeh basin are unknowns; (3) the boundary between the Sistan suture zone and the Lut Block, originally defined by the NE limit of the Jurassic pelitic schist, must be refined since Jurassic sediments are overlain by younger Cretaceous deposits in several places.

4. Methodology: from field to P-T-t estimations

This section presents an overview of the methodology used in this study. Details on the analytical protocols, the tools used to estimate P-T conditions or the geochronological methods can be found below in the Appendix (together with relevant references).

Fieldwork consisted in collecting structural data to build cross-sections and samples for metamorphic and geochronologic analysis, mainly on three targets (Figs. 2c ; 4): (1) the eastern side of the Sistan orogen, in order to refine the organization of the Ratuk complex and the

Sefidabeh basin and to constrain the relationships between the main domains; (2) the central domain, to constrain the internal organization of the Neh complex and (3) the border between the Neh complex and the Lut Block, to constrain their mutual relationships and metamorphism.

Textures, mineral occurrences and mineral zoning were determined by optical microscopy and scanning slectron microscopy (SEM, ZEISS Supra 55 VP). Mineral compositions were determined by electron probe micro-analysis (Cameca SX-5 and SX-100; CAMPARIS, Sorbonne Université). Maximum temperatures experienced by organic-rich samples were determined by Raman spectroscopy of Carbonaceous Material (RSCM; Renishaw inVia, Ecole Normale Supérieure), following the method of Beyssac et al. (2002).

Whole-rock major element composition was obtained after crushing and dissolution by Inductively Coupled Plasma Optical Emission Spectrometry (ICP-OES iCap 6 500; ALIPP6, Sorbonne Université).

Ar/Ar isotopic measurements were done on grain separates by laser ablation coupled to a multi-collector noble gas mass spectrometer (Thermo-Fisher Argus VI; Géosciences Montpellier). Titanite U-Pb analyses were performed in-situ in thin sections by laser ablation split-stream inductively coupled plasma mass spectrometry (LASS ICP-MS; Univ. California Santa Barbara).

Different methods were used to estimate P-T conditions depending on each lithology. For mafic samples, the Ti content in Ca-Amphibole (Ernst and Liu, 1998) and the Na-Si vs Ca-Al exchange between amphibole and plagioclase (Holland and Blundy, 1994) were used to estimate temperature. The Al/Si exchange between plagioclase and Ca-Amphibole were used to estimate equilibrium pressure (Ernst and Liu, 1998). The Zr content in titanite was used, in zircon-bearing samples, to place constraints on maximum temperature conditions.

For metasedimentary rocks, maximum temperatures were estimated by the RSCM method. Empirical thermometry based on the Ti content in biotite and Garnet-Biotite Fe-Mg

exchange was also used. Pressure was estimated using Garnet-Biotite-Aluminosilicate-Quartz barometry.

Thermodynamic modelling of selected samples was performed in the NCFMASHTO and MnNCKFMASHTO chemical systems, respectively, with the Perple-X software (Connolly, 2005) using whole-rock compositions. Mineral assemblages and chemistry were then compared to those predicted by thermodynamical modelling.

5. Sedimentary basins: types and burial metamorphism

5.1. Stratigraphy

This section summarizes the observations made by Tirrul et al. (1983) and Maurizot et al. (1990a; 1990b), complemented by ours. Though not representative of all parts of the basins, this description is meant to illustrate the style of sedimentation and the stratigraphic relationships within the Sefidabeh, Ratuk and Neh complexes (Figs. 3).

5.1.1. Stratigraphy of the Sefidabeh basin

The thickness of the Cenomanian to Eocene sedimentary deposits in the Sefidabeh basin (Figs. 3) was estimated at around 8 km (Tirrul et al., 1983). In the Northern Sistan Orogen, the Sefidabeh basin develops on the Afghan margin (see below).

The oldest rocks are mainly Senonian in age but some biostratigraphic markers hint to an Aptian age for the base of this formation (Tirrul et al., 1983). This sequence (Lahnu formation, Figs. 5a) is mainly composed by calci-turbidite with layers of marl and limestone, in places called (calc-)flysh. Calc-alkaline rocks and adakites are intrusive or interbedded in this sequence (Jentzer et al., 2020). In some places, Maastrichtian sediments can be recognized. Their base is a polygenic breccia reworking ophiolite pebbles (Darband-Bad formation; Figs. 5b) evolving upwards into a turbiditic, marl and shale sequence (Nesfandeh formation; Figs. 5c) locally interbedded with a ten-meter-thick Hyppuritic and Orbitoid bearing limestone (Figs.

5d-f). Maastrichtian ages were confirmed, east of Sulabest, by biostratigraphy on microfossil assemblage (Omphalocyclus sp., Lepidorbitoides sp., Orbitoides sp., Siderolites sp; S. Soleimani, GSI, pers. comm.).

The base of the Paleocene is a reefal limestone slightly unconformable on top of the Upper Cretaceous deposits, showing large thickness variations, from ~0 to >600 m (Palang formation; Figs. 5g-h). It is overlain by an Upper Paleocene turbiditic sequence (Chah Chucchu formation; Figs. 5i) locally preserving paleo-channels and Nummulites, especially in the core of synclines.

Eocene sediments are “red beds” polygenic continental puddingstone observed only on the easternmost part of the basin (Figs. 5j). They lie unconformably on top of the Paleocene series. Calc-alkaline affiniy lavas and dykes are present in the Eocene. Oligocene deposits correspond also to “red bed” facies with an increase of the volcano-clastic component from the Eocene magmatic activity. Although both sedimentary sequences are conglomeratic, a major unconformity marks the limit between Eocene and Oligocene deposits. Miocene lavas and dykes are found in a few places (Camp and Griffith, 1983). The latest sediments are Plio-quaternary polygenic continental conglomerates reworking all previous lithologies (Figs. 5k).

5.1.2. Stratigraphy of the Ratuk complex

The metamorphic units of the Ratuk complex (see Geological setting) are unconformably overlain by a Maastrichtian conglomerate evolving upwards into a turbiditic sequence (equivalent to the Darband-Bad formation; Figs. 5b). In some places, Eocene red-beds (equivalent those in Figs. 5j) overly unconformably the Maastrichitain sequence. Plio-quaternary polygenic conglomerates (equivalent of Figs. 5k) are also locally observed.

5.1.3. Stratigraphy of the Neh complex

The total thickness of the sedimentary succession of the Neh basin, from Upper Turonian to Eocene, reaches ~4 km (Tirrul et al., 1983). Half of it is made by phyllite

interbedded with sandstone dated from the Upper Cretaceous to the Early Cenozoic (most likely Paleocene).

The first sedimentary rocks on top or interbedded between lavas of the ophiolite are alternations of radiolarian chert, marl and/or limestone (Figs. 5l). No biostratigraphic dating is available for these rocks but a Lower Cretaceous age could be expected based on the geochronologic ages of the ophiolite (between 124 and 107 Ma, Aptian-Albian).

Upper Cretaceous and Paleocene deposits are fine grained turbidites dominated by phyllite, minor sandstone and locally layers of limestone (Figs..5m-n). These depositis are referred to as flysch in some 1:250000 scale maps. Upper Cretaceous deposits are mostly exposed in the eastern part of the Neh complex, whereas Paleocene sediments dominate in its central part (Figs. 2c).

Eocene sedimentation exhibits a marked increase of the clastic component. In the southern Neh complex, where Eocene deposits are best exposed (Figs. 2c), sediments are silici-clastic turbidite (aka flysch; Figs. 5o) interbedded with Nummulite bearing sandy limestone (Figs. 5p). In the North, the Eocene and Oligo-Miocene deposits are mainly composed by a shallower, massive conglomerate reworking all previous lithologies (Figs. 5q), including andesitic Eocene volcanics. Conglomerates are interbedded with a Nummulite-bearing sandy limestone. A major unconformity marks the limit between Eocene and Oligocene deposits (Tirrul et al., 1983). The latest sediments are Pliocene polygenic channelized continental conglomerate reworking all the previous lithologies (Figs. 5r).

5.2. Maximum temperatures experienced by Sistan sediments

In order to evaluate the amount of differential burial of the various sediments (and estimate either burial depths or heat fluxes), RSCM measurements were performed on samples collected from the Neh complex and from the northern limit of the Lut Block. Out of the 44 samples, about half of them had a too low or oxidized organic content. Results for the other

half, out of which 13 from the Upper Cretaceous and 5 from the Paleocene Neh complex, are shown in Figure 6 (and on Supplementary material 2). None of the Eocene samples yielded results. Three samples come from the Jurassic siltstone of the Lut block. Figure 4 is complemented by three variably metamorphosed Late Cretaceous flysch samples from the HP-LT Ratuk complex (sample 14-38 is not unmetamorphosed; Bonnet et al., 2018). Maximum temperatures (Tmax) can be divided in three groups (Figs. 6):

(1) Tmax obtained throughout the Neh complex, from the Paleocene sample 16-68 in the south to the Cretaceous sample 14-37 in the north, are close to the average 275°C ±50°C value. Tmax from Upper Cretaceous or Paleocene samples are undistinguishable. Only one sample (16-41) gives a higher value, which could be explained by its proximity with several intrusive dykes (which are known to affect Tmax estimates; e.g., Chen et al., 2017).

(2) Except for sample 17-20 with 326°C, samples from the S of the Neh complex (14-07; 14-23a, 15b-10 and 16-80) have a significantly higher Tmax at 515°C on average, close to those obtained in the Jurassic deposits of the Lut Block at 508°C in average. These results will be interpreted in the light of their structural position (see discussion below).

(3) In the north east, sample 14-38 has a Tmax compatible with the average 270°C in the Neh complex while samples 14-39a/b and 14-40 give Tmax 70°C higher.

6. Ophiolitic rocks from the Neh complex

The structures and lithologies of the ophiolitic part of the Neh complex were studied to the south of Birjand and northwest of Nehbandan. Figures 4 and 7-8 show some of the main ophiolite exposures, with special emphasis on the ophiolitic ridge south of Birjand.

6.1.Overall structure and internal organization of the ophiolitic ridge near Birjand

The 1:100 000 map of the Birjand ophiolitic ridge (essentially produced using airplane photographs; Eftekhar Nezhad et al., 1987) features at least three types of colored mélange and

profuse vertical contacts between peridotites, serpentinites, basalts and gabbros. Based on extensive observations (Figs. 4a; and complementary satellite images), we have reappraised the structural organization of the eastern sector of the Birjand ophiolitic ridge, identifying three main units thrust on top of each other (Fig. 7):

(1) The northernmost Unit 1 is characterized, from bottom to top, by peridotites, an almost continuous level of pillow-lavas or brecciated basalts, rare radiolarites and Cretaceous turbidites. Thrusting of Unit 1 over Unit 2 is marked by a crushed zone with various dismembered material (Fig. 7b). Some exposures show evidence for the existence of fossil oceanic detachment faults. In the outcrop shown in figures 8a-f (interpreted in Fig. 7f), a hm- to km-scale fault zone, outlined by striated peridotite and foliated amphibolite facies gabbro, separates serpentinized peridotite, overlain by a breccia containing clasts of dismembered pillows within a carbonate matrix and pillow-basalts above, from serpentinized peridotite sparsely overlain by ophicalcite.

(2) Unit 2 (Fig. 7c) is characterized by massively serpentinized and in places brecciated peridotite (Figs 8g-h) with dunitic channels. This mantle section is cross-cut by scarce rodingites and plagiogranites and locally intruded by gabbroic pods, which is uncommon in Unit 1. Contrary to Unit 1, pillow lavas are rare and do not constitute a continuous horizon. At the base of Unit 2, the contact onto Unit 3 is outlined by a tectonic mélange (Figs. 7c).

(3) Unit 3 mostly crops out as a tectonic window below Unit 2 (Fig. 7d). Unit 3 is characterized by serpentinized peridotite intruded by large masses of gabbros and dolerites and overlayed by ophicalcite and breccaited materail (Figs. 8i-k). Pillow-lavas are rare and discontinuous, as for Unit 2. Radiolarian cherts and Cretaceous turbidites are present in a few places. The Eocene Nummulitic sandy limestone was deposited unconformably either on the Cretaceous turbidite or directly on the peridotite. This Eocene deposit is affected by large-scale

asymmetric drag folds and overthrust in places by peridotites of Unit 2 or Unit 3 (Fig. 7d). This basal unit exhibits metasedimentary rocks (see below).

Each of these units shows kilometre scale continuity, at odds with the characteristics of a chaotic mélange (Fig. 7e). The stack of units was affected by later tectonics, as shown by the thrusting of peridotite over Neogene conglomeratic deposits south of the Birjand ridge, or by sinistral strike-slip faults cutting through the ridge. The core of the Birjand ridge was intruded by Oligo-Miocene then Plio-Quaternary magmatism.

6.2. Petrology and mineralogy

A brief overview of the petrology and mineralogy of the three main lithologies observed in the ophiolite is given here (Table 1). Peridotites, mildly to completely serpentinized (Figs. 9a-b), dominantly correspond to harzburgite with olivine, orthopyroxene, rare clinopyroxene, titanite, Fe-Ti oxide and occasional amphibole (Delavari et al., 2009; Saccani et al., 2010; Zarrinkoub et al., 2012a). Gabbroic intrusions mostly comprise clinopyroxene and plagioclase, commonly altered to prehnite. A foliation marked by amphiboles is visible in some samples (Figs. 9c-d).

Basalts are exposed as discontinuous layers, hundred meters thick at most. They are made of phenocrysts of clinopyroxene, plagioclase and Fe-Ti oxide in an aphanitic matrix (Figs.9e-f). Some have secondary phases such as epidote and/or pumpellite and occasional calcite veins. Basaltic fragments are also found directly above serpentinized peridotite, as cm- to m-cale clasts in sedimentary breccia/ olistostrome or ophicarbonates.

Microprobe analyses were performed in serpentinized peridotite and gabbro (see supplementary material 1). In gabbros, clinopyroxene compositions are close to augite, while amphibole compositions range from actinolite to tschermakite but are mainly Mg-hornblende; plagioclase is >88 mol% albite. Serpentinized peridotites contain enstatite, amphibole (mostly tremolite or edenite, but wiht some Mg-hornblende) and olivine close to the forsterite

endmember. Semiquantitative amphibole geothermobarometry (Ernst et Liu, 1998) gave results between 625°C and 775°C and between 0.3 GPa and 0.7 GPa for the amphibolitized gabbroic sample 16-01c (equivalent to 15b-18 in Fig. 8e).

7. Sections across the northern branch of the Sistan orogen

Structural observations are summarized on nine sections across the Sistan belt, presented from north to south (Figs. 11; location on Fig. 2c). Representative exposures are shown in Figure 11.

7.1. Gomenj transect

This northern cross-section comprises four main domains (Fig. 11a). In its western part, a thick series of Quaternary and Neogene conglomerates is deformed and overthrust by Upper Cretaceous flysch and unmetamorphosed ophiolitic rocks. The area is pervasively intruded by Eocene to Miocene magmatism.

Further east, a hm-thick crushed zone with amphibolitized blocks in a serpentinite matrix (and abundant listvenite) likely corresponds to the HP-LT zone observed in Gazik (section below) or Sulabest (Angiboust et al., 2013). Sefidabeh basin sediments are thrust over the crushed zone.

These sediments consist of Upper Cretaceous (Senonian) flysch interbedded and/or intruded by arc magmatic rocks unconformably overlain by the Paleocene reef limestone and turbidite (equivalent to the one in Figs. 10a, c), and finally by the Eocene “red bed”. At this latitude the Sefidabeh basin is extremely narrow, allowing to study the basement of the Afghan Block in the eastern part of the section. This basement comprises of Paleozoic granodiorite and amphibolites and a sedimentary cover made of Early Cretaceous series (i.e., oosparitic sandstone overlain by Orbitolina limestone). Basement rocks are thrusted over the Sefidabeh basin in its western part, while large-scale folds are observed in the sedimentary cover in the

eastern part. The thrust contact between the basement and the cover corresponds to a reactivated normal fault. On this transect, the western limit of the Afghan block (Tirrul et al., 1983) does not always coincide with the westernmost outcrop of Orbitolina limestone.

7.2. Gazik transect

This section reveals four main parts (Figs. 11b; for more local sections on this transect: Bonnet et al. 2018; Jentzer et al., 2020), from west to east:

(1) An ultramafic unit made of serpentinite with rare radiolarites or basalts and locally m- to hm-large gabbroic intrusions. It is overlain by folded Cretaceous turbidite (intruded by Oligo-Miocene dykes). This unit is in apparent continuity with the (mostly) unmetamorphosed Neh complex.

(2) Slices of serpentinized peridotite, with a few gabbroic pods, locally overlain by pillow lavas and/or radiolarite. In the eastern part, thick Maastrichtian turbidites are folded into a broad syncline and intruded by massive Oligo-Miocene quartz-diorites. The basal peridotite hosts Senonian adakitic dykes and sills.

(3) The HP-LT zone, more extensive than on the Gomenj section, which comprises three mains units separated by tectonic contacts (Fig. 10d): (a) a serpentinite-matrix mélange made of a fine-grained (to locally massive) matrix surrounding metamorphic blocks of pillow-lavas or metatuffs. This mélange can be sub-divided based on the peak metamorphic assemblage of the blocks: the basal portion reached eclogitic facies while the top portion only reached blueschist facies (Bonnet et al., 2018); (b) a mélange with a tuffaceous matrix, containing blocks of marl, radiolarite, serpentinite, sandstone or basalts, metamorphosed in the greenschist facies at most; (c) Maastrichtian turbiditic sediments, with a monogenic basal conglomerate reworking pieces of serpentinite.

(4) The Sefidabeh basin, with the same characteristics as in Gomenj.

The suture zone separates the HP-LT zone from the Afghan block, here marked by the Orbitolina limestone. It is represented by a steep contact, which must have accommodated the exhumation of the HP-LT units. The boundary between the HP-LT zone and the Sefidabeh basin was reworked into a major reverse and right lateral strike-slip fault (Fig. 11b). Steep faults and local back-thrusting hints to the presence at depth of a flower structure along the contact. Upper Cretaceous volcanocalstics found along this transect could correspond to material reworked from the former Senonian magmatic arc (Jentzer et al., 2020).

7.3. Razeh transect

The Razeh cross-section outlines the southward widening of the Sefidabeh basin (Fig. 11c). In its western part, Quaternary conglomerates unconformably overlie coarse Maastrichtian sediments deposited on top of the HP-LT units and are actively deformed below the overthrusting Sefidabeh basin (close to Fig. 10a). To the east, the Sefidabeh basin consists of Upper Cretaceous (Senonian) flysch interbedded with a ten-meter thick reef preserving large rudists. It is interbedded and/or intruded by a significant amount of arc magmatic rocks. The younger Paleocene reef appears slightly unconformable and shows large thickness variations, from ~0 to >600 m (sames as Figs. 10a, c). Above it, the Paleocene turbidite with Nummulite-rich paleo-channels is preserved in the core of a broad syncline. Eocene red beds, observed in the easternmost part only, lie unconformably on locally very thin Paleocene series. The absence of Paleocene turbidite hints to erosion prior to deposition of Eocene sediments. Eocene to Miocene magmatic rocks intrusions are present.

7.4. Sulabest transect

A major dextral strike-slip fault (the East Neh fault) marks the eastern limit of the Neh complex. Three main units of the Ratuk complex proposed by Angiboust et al. (2013) were recognized by (close to Fig. 10d), from bottom to top: (1) the Eclogitic Unit, at the base, cropping-out into a tectonic window, corresponds to a mélange with a serpentinized matrix

surrounding rare blocks of metaradiolarite and more abundant eclogitic metabasic blocks retrogressed into amphibolite facies; (2) the Upper Unit, which is a mélange with a tuffaceous matrix hosting blocks metamorphosed in the blueschist facies; (3) the Western Unit, made of serpentinized peridotite, pockets of gabbro, pillow basalts and radiolarites, which lacks HP-LT metamorphic relics. The Western Unit is in apparent contintuity with the unmetamorphosed ophiolitic units found to the west of the HP-LT zone in the previous cross-sections. Since this unit also exhibits Senonian arc magmatism (Jentzer et al., 2020), we consider that it represents the westernmost domain of the Afghan Block, either a stretched ocean continent transitional domain or an accreted forearc domain.

To the east, the HP-LT units are covered by folded Maastrichtian polygenic conglomerates grading upwards into a turbiditic sequence. Plio-Quaternary polygenic conglomerates overlie all previous lithologies and are deformed below the thrust contact with the Sefidabeh basin (locally underlined by abundant listvenite). The western part of the Sefidabeh basin is characterized by Upper Cretaceous (Senonian) turbidite and associated arc magmatism rocks covered by the Paleocene reef. Its overall structure is comparable to that presented on the Razeh cross-section (Fig. 11c). All units are intruded by Eocene to Miocene magmatism, located in the vicinity of major tectonic contacts and recently deformed. Neogene (Pliocene to Quaternary) alkali-basalts with basaltic columns are present close to the East Neh fault (Fig. 10e).

7.5. Doroh transect

The Doroh cross-section corresponds to our southernmost transect along the contact between the HP-LT zone and the Afghan Block (Fig. 11e). Its western part exhibits the same lithologies and structural organization as in the previously described HP-LT zone (e.g., Fig. 10d), with an Eclogitic Unit covered by Maastrichtian deposits and Plio-Quaternary folded polygenic conglomerates. The Sefidabeh basin is thrusted over the HP-LT units. It comprises

Senonian turbidites with abundant calc-alkaline magmatic intrusions, lavas and volcano-sedimentary rocks. The lowermost series is a polygenic Upper Cretaceous coarse conglomerate (Fig. 10b). The Paleocene reef outlines west-vergent asymmetric folds (as in Figs. 10a, c).

7.6. Forg transect

Forg cross-section (Fig. 11f) is located to the southwest and almost continuous with the Gazik cross-section but the part in between is not exposed. In the northeast, the Forg cross-section exhibits Cretaceous phyllites unconformably overlain by an intensely deformed distal, thinly bedded Paleocene sequence showing southwest-vergent asymmetric folds and a pervasive sub-vertical schistosity. This transect is cut by the major Purang dextral strike-slip fault and smaller conjugate sinistral and reverse faults outlining the existence of a flower structure. Thrusts locally expose an ophiolitic unit, made of serpentinized peridotite and discontinuous horizons of pillow-lavas, below the Cretaceous sediments (Figs. 10g, h). In the middle of the section, Paleocene deposits are directly found on top ot the ophiolitic basement. They are thrusted over abundant Oligocene to Miocene lavas in the southern part. Some Plio-Quatenary alkali-basalts are also present.

7.7. Birjand transect

Birjand cross-section (Fig. 9g) shows three main units stacked on top of one another and was detailed before, when addressing the overall structure of the Birjand ophiolite (see section 6; Fig. 7). Peridotites of Unit 3 are thrust onto the Eocene sandy-limestone. Unit 2 is thrust over Neogene conglomerates, testifying to the existence of recent deformation. This transect is affected by large-scale sinistral strike-slip faults.

7.8. Ramengan transect

Ramengan cross-section (Fig. 11h) is separated from the Forg cross-section by an extensive synclinorium of Neogene deposits (Fig. 4). In its southern part, the synclinorium is cored by Eocene deposits showing two main lithologies, i.e. a turbiditic sequence and shaly

sediments. The shale deposits exhibit two orthogonal foliation planes. The Eocene lies unconformably above Upper Cretaceous deposits or, locally, Paleocene sediments. Eo-Oligocene magmatism is largely exposed (Fig. 10i). The Cretaceous deposits are pervasively deformed, show southwest-vergent folds and are thrusted over the northern flank of this synclinorium (Figs. 10j, k). Serpentinite associated with basalts and/or radiolarites in the cores of small thrust-related anticlines attests to the presence of an ophiolitic basement (Fig. 10l). Paleocene sediments only crop out in the northern part of this cross-section.

7.9. Barak transect

This transect (Fig. 11i) exposes andalusite-bearing Jurassic metasandstones from the Lut Block (Fig. 10m) and some marbles, both tilted to the north. The southern limit of the Neh complex is marked by a hm-thick basalt succession. The contact between the Lut metasediments and the Neh basalt is not well exposed and consists of basalts thrust onto metasediments. The northern part of the Neh complex forms an antiformal stack with three main units: (1) a basal unit composed by serpentinite intruded by gabbro and topped by pervasively deformed Cretaceous sediments showing the highest Tmax determined by RSCM (between 460°C and 560°C); (2) a second unit showing amphibolite facies metatuffs and metabasalts capped by peridotites (Figs. 10n-p); (3) on top, a third unit, mostly visible on the southern flank of the antiform, is composed by strained amphibolites found immediately below peridotites. Ultramafics are covered by Cretaceous sediments interlayered with basaltic lavas.

The core of this structure is intruded by a granitoid stock (Fig. 3q) affected by a slight schistosity and locally lineated. It is dated from the base of the Eocene by Ar-Ar on biotite (see below). A petrologically different muscovite-tourmaline-bearing granitic intrusion cuts across the contact between the Neh complex and the Lut Block. It could belong the abundant Eo-Oligocene magmatism observed in the area (Figs. 2a, 4).

8. Metamorphic evolutions in the western part of the Sistan orogen

This section focuses on two sets of metamorphic rocks found structurally below the Neh ophiolite (Table 1; Figs. 10; see Figs. 2 for location): (1) those immediately underlying peridotites, as do metamorphic soles (Wakabayashi and Dilek, 2000): amphibolite facies metatuffs and metabasalts; lawsonite-bearing greenschist to blueschist facies metaradiolarites; (2) metamorphic rocks present in the northern part of the Lut Block only: amphibolite to granulite facies gneisses and metasediments (Deh-Salm area); pelitic metasediments showing contact metamorphism. Blueschists and eclogites from the HP-LT zone were extensively studied already and are not detailed here (Fotoohi Rad et al., 2005, 2009; Angiboust et al., 2013; Bröcker et al., 2013; Kurzawa et al., 2017; Bonnet et al., 2018). Ocean-floor metamorphism subsequent to ophiolite genesis (marked by amphibolitized gabbros, serpentinites) was briefly presented in section 6.

8.1. Petrography

8.1.1. Birjand metasediments

Metamorphosed sediments were found within a tectonic slice between Units 2 and 3 in the core of the Birjand ridge (Figs. 4, 7, 11g). Two main lithologies were observed (Table 1):

(1) Hm-scale boudins of metaradiolarites (Figs. 12a) composed of quartz and blue amphibole associated with garnet, phengite, plagioclase, epidote, ilmenite, rare pyroxene and retrograde chlorite. The schistosity is marked by the alignment of amphibole and phengite. The same rock type was found as cm- to m-scale blocks in Eocene conglomerates (Mahmudali, Figs. 4; sample 15b-19).

(2) Clastic material within a carbonate matrix (Figs. 12b-d): (i) ophicalcite with serpentine, magnetite, calcite, birefringent garnet and lawsonite; (ii) a basalt-rich breccia with amphibole, titanite, calcite and lawsonite; (iii) a gabbro-rich breccia with calcite and lawsonite in the matrix and plagioclase, clinopyroxene and lawsonite in the gabbroic clasts. Lawsonite

appears in equilibrium within both the clasts and the carbonate matrix, implying that the brecciation occurred prior to the metamorphic event.

8.1.2. Amphibolite facies soles

Amphibolites and associated metasediments were collected in 10-20 m-thick horizons below serpentinized peridotite in two distinct areas (Figs. 4, 10n-o-p, 11i), south of Barak and to the north-east of Sahlabad, except for sample 14-01 which was found as a block in Eocene conglomerates near Birjand). All of them exhibit a strong schistosity and lineation marked by the orientation of amphibole (Figs. 12e-f).

Amphibolites comprise amphibole, plagioclase, accessory ilmenite (Table 1; samples 14-01, 16-45b; Figs. 12e) and secondary phases such as titanite, epidote and quartz. Some additionally contain clinopyroxene (samples 14-11b2 to 17-18; Figs. 12g-h), either in the foliation or present as boudins (in association with Ca-rich garnet).

Metasediments (samples 14-07, 14-23a, 16-80) are composed of quartz, and phyllosilicates, i.e. white micas or biotite and retrograde chlorite. Two of them, which contain organic matter, provided RSCM maximum temperatures of 515°C on average (Fig. 6).

8.1.3. Metamorphic rocks of the Lut block at the boundary with the Neh complex

These samples correspond to micaschists showing three mineral assemblages: (i) the first one (Figs. 12i) is made by biotite and occasional garnet inclusions in andalusite (sample 16-74); (ii) the second one shows the destabilization of andalusite into sillimanite, associated with white micas and biotite (Figs. 12i-j); (iii) the last one consists of biotite which marks the main foliation, quartz and sometimes plagioclase (Figs. 12i-j). Accessory phases such as tourmaline, Fe-Ti oxide, zircon and organic matter are present (Table 1).

8.1.4. Metamorphic rocks of the Lut Block: Deh-Salm complex

Rocks from the Deh-Salm metamorphic complex were reported during the mapping programme in the 1970s and dated at ~165-160 Ma by Mahmoudi et al. (2010), yet their P-T

conditions and path are still poorly constrained. Three types of metamorphic rocks were distinguished in this area:

(1) Micaschists in the northern part of the Deh-Salm complex, together with marbles and metasandstones. Micaschists consist of quartz, biotite forming the foliation, plagioclase, frequently associated with white mica, sillimanite and sometimes orthoclase. Tourmaline, rutile and titanite are the main accessory phases. Biotite and white mica are altered into chlorite and kaolinite, respectively.

(2) Migmatites exposed in the southern part of the Deh-Salm complex (Fig. 12k-n) showing three successive parageneses: (i) the earliest is made of kyanite, garnet, biotite and white mica (Figs. 12k-l); (ii) the second one comprises quartz, plagioclase and fibrous sillimanite parallel to the main foliation and appears contemporaneous with formation of the leucosome (Figs. 12l-m-n); (iii) the latest one comprises an association of prismatic sillimanite associated with white mica and some biotite crosscutting the main foliation (Figs. 12n), which likely postdates melting. Accessory minerals are tourmaline and Fe-Ti oxide (Table 1).

(3) Amphibolites, found as lenses into metasediments, comprising amphibole, plagioclase and clinopyroxene associated with some epidote and titanite.

8.2. Mineral chemistry

Representative microprobe analysis are available on supplementary material 2.

8.2.1. Birjand metasediments

Results for three metaradiolarite samples (Fig. 13a; supplementary material 1) show that blue amphibole is riebeckite ($Na_B \geq 1.5$, $(Na+K)_B < 0.5$; $XMg < 0.5$; $Fe^{3+}/(Fe^{3+}+Al) > 0.5$; Si between 7.5 and 8). White micas are phengitic with Si between 3.05 and 3.6 and XMg between 0.35 and 0.6. Garnet is manganese-rich (≥38% of spessartine endmember). Clinopyroxene from sample 15b-19 corresponds to omphacite. Felspar in sample 15b-19 is pure albite. Chlorite

isclose to the clinochlore end-member (≥75%) with Si between 2.75 and 3.15 and XMg from 0.4 to 0.85.

The studied metagabbroic clasts show that clinopyroxene lies between the aegyrine-augite and omphacite fields. Plagioclase is again pure albite. Chlorite is clinochlore with Si between 2.85 and 3.175 and XMg from 0.45 to 0.9. Serpentine from the adjacent metaophicalcite (sample 16-21b), determined through Raman spectroscopy corresponds to lizardite. Likewise, the nature of the carbonate matrix of the ophicalcite (16-21b) was determined to be calcite.

8.2.2. Amphibolite facies soles

Microprobe analyses were performed on twelve amphibolites and one metasediment (14-07; Figs. 13b, supplementary material 1). Amphibole is calcic and corresponds to Mg-hornblende, except for some crystals trending towards the tschermakite or tremolite end-members. XMg ranges between 0.4 and 0.85. While the composition is fairly homogeneous in each sample, a wide range of compositions is observed from one sample to the other (Figs. 13b) yet without clear spatial correlations between samples from the north-east (Sahlabad) to the south (Barak). Feldspar is dominantly plagioclase, most commonly around 65% albite, yet spanning the full range of compositions (from 94% anorthite to 98% albite). Four samples contain minor amounts of K-feldspar.

Pyroxene is diopsidic in the four analysed samples (14-11b, 14-20, 14-26a and 17-18), except in sample 14-20 where it is richer in Al and Na and poorer in Ca (i.e., with an augitic composition close to that of sample 16-01c). Garnet (sample 14-11b) is intermediate between grossular and andradite. White mica is slightly phengitic, with Si varying between 3.1 and 3.2 in the metasediment (with XMg ~0.6). In amphibolites, Si varies from 3.2 to 3.4 and XMg from 0.45 to 0.85. Biotite (14-18) has a XMg of 0.65 and Si of 2.8. Epidote is close to the ferric end-member. Chlorite is close to clinochlore composition.

Trace element composition of titanites, in particular the Zr content, was obtained via laser ablation split-stream inductively coupled plasma mass spectrometry (Figs. 13b; see LASS-ICPMS methodology in Appendix). Mean values of the Zr content range between 110 and 185 ppm (14-09: 154 ppm, for a 114-216 range; 14-18: 111 ppm, 42-192 range; 16-42: 158 ppm, 35-460 ppm range; 17-18: 184 ppm, 80-339 ppm range).

8.2.3. Metamorphic rocks of the Lut block at the boundary with the Neh complex

Biotite has a XMg ranging between 0.35 and 0.5 and Si between 2.5 and 2.9 (Figs. 13c, supplementary material 1), with homogeneous composition in each of the three studied samples. Other minerals correspond to en-memeber compositions: albite, muscovite, almandine (sample 16-74). Chlorites are clinochlore. Andalusite is partially replaced by sillimanite. Andalusite is stable with garnet (for 16-74, Fig. 12i) and biotite, whereas sillimanite appears in equilibrium with muscovite and biotite. The two texturally distinct biotite generations have the same composition however.

8.2.4. Metamorphic rocks of the Lut Block: Deh-Salm complex

Measurements were performed for three micaschists (16-54, 55, 57), one migmatite (14-29) and one amphibolite (16-56; Figs. 11d; supplementary material 1). Biotite shows XMg values between 0.35 and 0.45 and Si between 2.55 and 2.9, except for samples 16-57 and partly 16-54 (XMg ~0.55). Chemical mapping (sample 14-29a) confirms the textural difference observed between biotite crystals: biotite associated with garnet has XMg $\geq$ 0.4, whereas biotite replacing garnet has XMg < 0.4. Garnet from sample 14-29a are almandine-rich and homogeneous, except for a small rim exhibiting Mn-enrichment. Feldspar is mainly Na-rich plagioclase, with 50% to 100% albite end-member. Sample 16-57 also contains K-feldspar. Plagioclase in amphibolite (16-56) exhibit a wide range of compositions between 42% and 96% of albite end-member.

White mica is moderately phengitic. Si varies between 3 and 3.2, with rare values up to 3.4 and XMg ranges between 0.35 and 0.65. In sample 14-29a, white mica with the highest Si contents (>3.05) is associated with garnet, kyanite and biotite (XMg>0.4), whereas others are associated with retrograde sillimanite and biotite (XMg<0.4). Amphibole from sample 16-56 is Mg-hornblende with a XMg between 0.5 and 0.7.

8.3.P-T estimates

8.3.1. Birjand metasediments

Only approximate P-T conditions can be determined for these rocks, although their mineralogy hints to HP-LT conditions, as shown by the high Si content in phengite (up to 3.57 apfu) and the presence of omphacite in metaradiolarites, and the presence of lawsonite and omphacite in metamafic rocks. P-T conditions are bracketed by the stability fields of lawsonite, calcite and lizardite to lie between 150 and 300°C and 0.2 to 0.6 GPa (Fig. 14a).

8.3.2. Amphibolite facies soles

Plagioclase-amphibole geothermobarometry on eleven amphibolite samples gives a large range of P-T conditions, with an average value at 730°C ± 40°C and 0.65 GPa ± 0.2 GPa (Figs. 14b). Samples from the south (in blue) or the north (in green) cannot be distinguished. Thermobarometery based on the Zr content in titanite (Hayden et al., 2008; Zr~150-200 ppm for the samples, with estimated silica and titania activities of 1) is consistent with the results of plagioclase-amphibole thermobarometry.

Thermodynamic modelling was performed for sample 15b-15c (bulk composition available on supplementary material 3). Based on Ti and Si isopleths of amphibole and the absence of melting, P-T conditions can be estimated at around 700°C and 0.6 GPa (green rectangle on Figs. 14b), hence undistinguishable from the average P-T conditions estimated by plagioclase-amphibole thermobarometry on 8 amphibole-plagioclase pairs in this sample (714 ± 40°C, 0.54 ± 0.2 GPa; black rectangle on Figs. 14b). The predicted modes of the main phases

agree well with the observed mineralogy: between 40 and 45% of plagioclase, 40 to 45% of amphiboles. Pseudosection modelling also predicts presence of biotite <2% and augite <7% which have not been observed on thin-section (presumably due to their low abundance and/or potential retrogression).

8.3.3. Metamorphic rocks of the Lut block at the boundary with the Neh complex

Thermodynamic modelling for sample 16-72 (Fig. 14c, bulk composition available on supplementary material 3) allows constraining P-T conditions for the two main parageneses observed, i.e. (1) the biotite-andalusite assemblage (red field; Fig. 14c) and (2) the white mica, sillimanite and biotite assemblage (blue field; Fig. 14c). These P-T conditions are consistent with the results of the garnet-biotite thermometry for sample 16-74 (600-650°C ± 25°C). The P-T position of the two paragenesis initiates an anticlockwise P-T path.

8.3.4. Metamorphic rocks of the Lut Block: Deh-Salm complex

Thermometry based on the Ti content of biotite in four samples reveals the existence of two clusters of temperature (Figs. 12d), at 670°C ± 30°C and 740°C ± 20°C. GBAQ geobarometry coupled with garnet-biotite geothermometry shows that the P-T conditions of the kyanite-garnet-biotite-phengite-bearing assemblage of sample 14-29a lie in the range 640-670°C ±25°C and 0.75-0.85 GPa ± 0.2 GPa (Figs. 12d).

Thermodynamic modelling was performed for the migmatitic sample 14-29a (Figs. 14d, bulk composition available on supplementary material 3). Caution is needed since the overall chemistry may have been modified by partial melting. This does not apply, however, to the paragenesis postdating melting (i.e., with prismatic sillimanite, white mica and biotite), which yields conditions between 590 and 670°C and 0.35 to 0.6 GPa (blue field Figs. 14d). Small garnet amounts are predicted (<2%) but probably too low to be observed on thin-section. Conditions for the quartz-plagioclase-sillimanite leucosome lie above 690°C. Results of Ti-in-biotite thermometry (~740°C) provide rough pressure estimate around 0.7 GPa (red circle on

Figs. 14d). The estimate for the early quartz-biotite-sillimanite-garnet-kyanite-plagioclase±rutile paragenesis (~670°C, 0.8 GPa) lies close to the P-T conditions determined using GBAQ/GB geothermobarometry, suggesting only minor modification of the overall chemistry by partial melting. The succession of these mineral assemblages suggests a clockwise P-T path (black dotted line, Figs. 14d).

9. Geochronology

Rocks corresponding to four domains have been dated. Figs. 15 gathers all the results of our dating. All uncertainties are given as ±2σ in the text.

- Ophiolitic rocks of the Neh complex

$^{40}Ar/^{39}Ar$ step-heating of amphiboles from the amphibolitic gabbro 15b-18 provided a plateau age of 106.3 ± 3.1 Ma (Figs. 15a) that includes 100% of released ^{39}Ar.

- Birjand metasediments

$^{40}Ar/^{39}Ar$ step-heating of phengite from two metaradiolarite samples 14b-14 and 15b-19 yielded by plateau ages of 72.2 ± 0.3 and 74.1 ± 0.3 Ma that includes 100% and 98.43% of released ^{39}Ar respectively (Figs. 15b and c).

- Amphibolitic sole and associated rocks of the Neh complex

Datings on amphibolite give three populations of ages:

(1) The oldest was obtained on sample 14-18 (collected close to Sahlabad) by in-situ U-Pb on 46 grains of titanite which yielded a Tera-Wasserburg isochron age of 108.6 ± 4.5 Ma (Figs. 15d);

(2) Intermediate ages were obtained on two samples collected close to Sahlabad which gave two indistinguishable ages: one by $^{40}Ar/^{39}Ar$ step heating method on amphibole provided a plateau age of 72.4 ± 0.6 that includes 100% and ^{39}Ar (Figs. 9e) and another by

in-situ U-Pb on 46 grains of titanite yielded a Tera-Wasserburg isochron age of 72.2 ± 2.1 Ma (Figs. 9f).

(3) The youngest ages were obtained on four samples collected in the area of Barak which gave five indistinguishable ages: three obtained by $^{40}Ar/^{39}Ar$ step heating method on amphibole provided age at 53.4 ± 1.7, 54.9 ± 2.6, 52.9 ± 0.5 Ma that includes 89%, 62.91% and 85.37% of released ^{39}Ar respectively (Figs. 13g, h and i) and two obtained by in-situ U-Pb on 29 (14-09) or 45 (17-18) grains of titanite yielded Tera-Wasserburg isochron ages of 54.1± 11.4 and 51.5 ± 1.4 Ma (Figs. 13g to k).

For the sample 14-09 the age obtained by Ar-Ar and U-Pb are undistinguishable, respectively at 53.4 ± 1.7 and 54.1 ± 11.4 Ma while for sample 14-18 $^{40}Ar/^{39}Ar$ step heating method on amphibole provide a 72.4 ± 0.6 Ma age significantly different from the U-Pb on titanite ages obtained at 108.6 ± 4.5 Ma.

Interestingly, in the area of Mahmudali, amphibolite were collected close to an intrusive and deformed granodiorite which was dated by $^{40}Ar/^{39}Ar$ step heating method on biotite providing an age of 49.6 ± 0.2 Ma that includes 83.46% of released ^{39}Ar (Figs. 13l).

- Metamorphic rocks of the Deh-Salm metamorphic complex

14-29 migmatite sample have been dated by $^{40}Ar/^{39}Ar$ step heating method on biotite at 150.0 ± 0.5 Ma that includes 76.68% of released ^{39}Ar (Figs. 9m).

10. Discussion

10.1. Overall structure of the northern Sistan orogen: major tectonic domains, boundaries and significance

Observations gathered from field investigations, from the different cross-sections and collected samples, together with data recently published by this group (Jentzer et al., 2017, 2020; Bonnet et al., 2018), are combined into a synthetic SW-NE crustal-scale section of the

northern Sistan orogen (Fig. 16; see profile location on Figs. 4). Some first-order characteristics and the relationships between the domains can be outlined:

- The HP-LT zone crops out as a series of discontinuous tectonic windows and marks the location of the suture zone. Early tectonic stacking and later doming characterize this domain (Bonnet et al., 2018). The suture zone contact is reworked by steeply dipping faults at present.

- The Afghan block, onto which the Sefidabeh basin developed, occupies the highest structural position. Cross-sections evidence a widening of the Sefidabeh basin towards the south, consistent with its larger extension in the southern Sistan orogen (Mohammadi et al., 2016; Bagheri and Damani Gol, 2020). The Afghan block also preserves evidence for Early Cretaceous (or earlier) normal faulting, which could reflect thinning of the continental margin (see also Tirrul et al., 1983). The Western Unit, which is sandwiched between the HP-LT zone and the Neh complex and corresponds to an unmetamorphosed ophiolitic sequence cross-cut by Late Cretaceous adakitic lavas (~86-71 Ma; Zarrinkoub et al., 2012b; Jentzer et al.,2020), is interpreted as a forearc of the Sistan subduction zone, possibly a reworked portion of the fomer ocean-continent transition on the Afghan passive margin side.

- The Neh complex preserves a relatively continuous obducted ophiolite, 50 to 80 km large across the profile (>100 km along strike; Figs. 16). Despite post-emplacement deformation of the ophiolite thrust sheet, distinct km-scale units evidence lateral contrasts within the former seafloor reminiscent of modern-day slow- to ultra-slow-spreading environments (e.g. Cannat et al., 2009, Picazo et al., 2012; Escartín et al., 2017): discontinuous and highly variable pillow-lava thicknesses, isolated masses of gabbro intruding serpentinized peridotite, ophicalcite or brecciated basalt and gabbro (i.e., mass wasting deposits) directly atop serpentinized peridotite, together with a lack of sheeted dyke complex. $^{40}Ar/^{39}Ar$ age dating of an amphibolitized gabbro

yielded 106 ± 3 Ma (Figs. 15a), close to the U-Pb zircon dating of oceanic leucogabbros (~110 Ma; Zarrinkoub et al., 2012a).

- The Neh ophiolitic complex is thrust to the SW over the Lut Block and overlain by the Ratuk complex or the Afghan Block (i.e., locally by the Western unit). A series of major NE-dipping contacts, parallel to the main tectonic contact marking the suture zone, are observed throughout this oceanic complex (Fig. 16). Sediments deposited onto the ophiolitic Neh complex indicate a progressive southwestward migration of the depocenter with time. The sedimentary thickness of the Paleocene and Eocene basins of the Neh complex, based on the maximum temperature experienced by the sediments (~275°C on average), could be on the order of -5 km assuming a 50°C.km^{-1} thermal gradient. Such a relatively warm gradient is similar to that of the upper continental crust of Central Tibet (Zhi Min and Wu, 1987) and justified by the likely high heat flow associated with the profuse magmatic activity postdating the Paleo/Eocene (Pang, 2013), or by the present-day value (84-103 mW m^{-2}; Davies, 2013). This thickness broadly agrees with the value proposed by Tirrul et al. (1983; ~4 km).

The overall structural organization and the fact that all the main contacts are dipping towards the NE are consistent with (i) a SW vergence of the orogen, (ii) a general underthrusting of the Neh complex below the Afghan block and (iii) the existence of a former NE dipping subduction. The latter was already proposed by Tirrul et al. (1983) and is strengthened by the location of a Late Cretaceous magmatic arc to the east of the suture zone (Jentzer et al., 2020). The southwestward shift of depocenters suggests an “en sequence” migration of the flexure in the lower plate with respect to the suture zone.

The series of thrusts marking the emplacement of the oceanic Neh complex onto the Lut block are cross-cut by lowermost Eocene acidic intrusions (~55-50 Ma). This indicates that final closure of the Sistan marginal basin was completed by then.

Collisional shortening is probably relatively modest: structures associated with early shortening like ophiolite sheets are well-preserved (Figs..7, 8), and the continental basement of the Lut block is not exposed below the Neh complex, suggesting that thick-skin deformation is insignificant and that the basement may not be significantly involved in the deformation. However, the extension of the Lut block below the Neh complex (Fig. 16; and the thickness of the Neh ophiolite, probably ~12 km at the onset of obduction processes; see below) is unknown. Based on gravimetric data, Mousavi and Ebbing (2018) and Eshagh et al. (2019) estimated that the thickness of the CEIM crust lies between 40 and 45 km with a slight increase up to 52 km below the Sistan orogen, which would be consistent with some minor implication of the basement of the Lut Block basement at depth. Shortening also varies along strike, as shown by the increase of deformation of the Sefidabeh domain towards the N indicating a greater shortening in the northern part of the orogen (see below).

In the absence of clear stratigraphic markers allowing to perform balanced cross-sections, and because of the intensity of ductile deformation in the Cretaceous to Paleocene flyschs and phyllites (as underlined by a well-developed schistosity; Figs. 5m, n), estimating the amount of shortening in the Sistan orogen is fraught with large uncertainties. A crude unfolding of ophiolite sheets and deformed basins suggests a minimum estimate of 80-100 km for the obduction overthrust onto the Lut block, and 30-50 km since final closure of the oceanic realm. We note that part of the first estimate may also have been acquired after closure.

10.2. Geodynamic significance of metamorphic rocks from the Neh complex and Lut block

10.2.1. Neh complex: evidence for intra-oceanic slicing and metamorphic sole formation during the onset of obduction

In addition to mineral transformations associated with oceanic deformation (see section 6) and/or hydrothermal alteration (Tirrul et al., 1983; Saccani et al., 2010; Zarrinkoub et al., 2012a), two new types of mineral recrystallization are reported here in the Neh complex:

(1) Strongly schistosed amphibolite facies metabasic and metasedimentary rocks, mostly metatuffs showing a marked lineation in places (Figs. 10o), are found as a 10-20 m thick horizons below the ophiolite (Figs. 10n, 11i, 16), particularly its southernmost exposures or near Sarbisheh (Figs. 4). Their metamorphic peak, based on thermodynamic modelling, amphibole-plagioclase thermobarometry and Zr content in titanite, lies at 700°C ± 50 and ~0.6-0.7 GPa (e.g., sample 15b-15c; Figs. 14b). Such characteristics suggest that these rocks represent a former metamorphic sole (Wakabayashi and Dilek, 2003; Agard et al., 2016), whose P-T conditions are intermediate between that of granulite facies HT soles (i.e., clinopyroxene-garnet bearing soles; Soret et al., 2017) and greenschist facies LT ones. Their protolith is also intermediate in composition (Agard et al., 2020).

Since metamorphic soles mark the initiation of intra-oceanic subduction (e.g., Wakabayashi and Dilek, 2003; Agard et al., 2016; Plunder et al., 2016; Guilmette et al., 2018; Dubacq et al., 2019), their age is an important constraint for the geodynamic evolution of the Sistan orogen. $^{40}Ar/^{39}Ar$ step heating on amphibole and in-situ U-Pb on titanite yielded three age populations for the metamorphic sole (Figs. 15d-k):

- two ages around 72 Ma, obtained by different methods on distinct samples (72.4 ± 0.6 Ma: $^{40}Ar/^{39}Ar$ step heating on amphibole, sample 14-18; 72.2 ± 1.1 Ma: in situ U-Pb on 59 titanite grains, sample 16-42; Figs. 15e-f).

- five ages between ca. 52 and 55 Ma (Figs. 15g-k), for samples collected in the vicinity of the large granitoid intrusions cutting across the sole (Figs. 10q, 11i, 16). These ages correspond within error to the ca. 50 Ma ages obtained for the granitoids (Fig. 15l) and are thus interpreted as reflecting recrystallization (of amphibole or titanite) during the magmatic event.

- one U-Pb titanite age at 108 ± 2 Ma (Fig. 15d), which is undistinguishable from the one obtained for the amphibolitic gabbro dated at 106 ± 3 Ma (Fig. 15a), and therefore interpreted as inherited from the oceanic activity.

We infer that the two ca. 72 Ma dates, which cannot be linked to any geological event reported so far in the Sistan orogen, correspond to the age of peak metamorphism for the metamorphic soles. If confirmed (see below), this constrains the onset of intra-oceanic subduction within the Sistan ocean and the start of the obduction process. This age lies between (i) the 86 ± 3 Ma peak burial of the suture zone eclogites, which attest to already ongoing E-dipping subduction below the Afghan Block, and (ii) final closure of the Sistan oceanic realm at ~55-50 Ma, as revealed by granitoid intrusions (e.g., sample 14-08) cross-cutting both the Lut Block and the ophiolite, and by the presence of Eocene continental molasse-type sediments (see below).

(2) Lawsonite-bearing rocks were found, in the mountain ridge south of Birjand, at the base of the ophiolitic Unit 2 (Figs. 7, 11g). The presence of lawsonite, in both gabbro clasts and in the carbonate matrix of an oceanic breccia, advocates for peak metamorphic conditions around 250°C and 0.4 GPa, at the transition between greenschist and blueschist facies conditions. Further evidence for metamorphic recrystallization and similar burial is provided by the presence of a phengite, spessartine-rich garnet, ferric blue amphibole and Al-bearing pyroxene assemblage in nearby metaradiolarites (Figs. 13a). $^{40}Ar/^{39}Ar$ step heating of phengite from two distinct metaradiolarite samples, located in the same structural position as the lawsonite-bearing ones, yielded 74.1 ± 0.3 Ma and 72.2 ± 0.3 by $^{40}Ar/^{39}Ar$ step heating (Figs. 15b, c). These ages are similar to those obtained for the metamorphic sole.

These metamorphic rocks collectively provide evidence for a specific deformation event occurring within the Sistan ocean during the Upper Campanian. We propose that this tectono-metamorphic event marks the initiation of intra-oceanic thrusting (and/or subduction), whose

amplitude was larger in the eastern part of the study area (metamorphic soles; Sarbisheh, Malabad) than in the west (lawsonite-bearing samples; Birjand ridge).

Incidentally, the presence of lawsonite-bearing rocks places constraints on the thickness of the ophiolitic material above, around 12-15 km at the time.

10.2.2. Lut Block contact metamorphism associated with Lower Eocene intrusions?

Metapelites located near the contact between the obducted Neh ophiolitic complex and the Lut Block show mineral assemblages indicative of contact metamorphism. Two main rock types are observed:

(1)The most common type contains quartz, biotite, plagioclase and andalusite. P-T conditions are estimated between 600 and 650°C and are lower than 0.3 GPa (red area on Figs. 14c). Whilst sedimentary layering is still visible, these rocks are slightly deformed and located near granitoid intrusions. This assemblage therefore likely reflects contact metamorphism and syn-kinematic growth during granitoid emplacement, at 49.6 ± 0.2 Ma (Fig. 15l).

(2)The second type comprises sillimanite overgrowing andalusite, white mica, plagioclase, biotite and quartz. It is stable in similar but slightly higher P-T conditions, between 625 and 650°C and between 0.3 and 0.4 GPa (blue area on Fig. 14c). This second type may reflect a stronger impact of contact metamorphism and/or additional thrusting following collision. The latter interpretation would be consistent with the existence, in places, of a foliation affecting granitoid intrusions, which advocates for some post-intrusion syn-collisional deformation.

In the absence of age constraints for these metamorphic rocks, we cannot rule out, however, that their metamorphism could be older than the granitoid intrusions, especially because of their similarity with some of the Jurassic metamorphic rocks of Anju or Dehsalm (Lut Block; see below).

10.2.3. Lut Block Deh-Salm metamorphic complex: mid- to late-Jurassic ("Mid"-Late-Cimmerian) regional metamorphism

The Deh-Salm metamorphic complex hosts amphibolites and metasediments exhibiting variable metamorphic degrees, from slightly deformed micaschists to migmatites showing an abundant leucosome and a strongly schistosed melanosome. In the migmatitic zone, the P-T-time path determined for the garnet-kyanite-biotite-plagioclase-phengite-bearing sample 14-29 shows three successive conditions (Figs. 14d): ~675°C and ~0.8 GPa for the peak of pressure, followed by a temperature increase associated with partial melting at around 725°C and 0.75GPa, and then retrograde conditions at 650°C and 0.4 GPa. $^{40}Ar/^{39}Ar$ step heating on biotite gave an age of 149.6 ± 0.5 Ma for this sample (Fig. 15m).

This metamorphic evolution is consistent with the regional metamorphism described by Masoudi et al. (2006; these authors also report contact metamorphism near granitic intrusions and thermal metamorphism marked by andalusite, sillimanite, and sillimanite and orthoclase isograds), with conditions increasing from chlorite-bearing rocks in the NE to staurolite-garnet-biotite-bearing amphibolite facies rocks in the SW. Our pressure estimates are higher than those obtained by Mahmoudi et al. (2010; 680°C and 0.35 GPa), possibly because these authors did not consider the presence of kyanite.

These previous studies (Mahmoudi et al., 2010; Masoudi et al., 2006) proposed that the protolith of the Deh-Salm complex is the Shemshak formation, i.e. the extensive Upper Triassic to Middle Jurassic siliciclastic formation covering most of northern Iran following Paleotethys closure, including the Lut Block. Based on U-Pb zircon and titanite dating of amphibolites and U-Pb monazite dating of metapelites (Mahmoudi et al., 2010), regional metamorphism is constrained between 165 and 160 Ma, and therefore Mid-Cimmerian. This age range overlaps with the 165 to 163 Ma ages obtained by U-Pb zircon or monazite dating (Mahmoudi et al., 2010) and Rb-Sr whole-rock dating of the nearby granitic intrusions (Esmaeily et al., 2005). Nd

and Sr isotopes furthermore support an upper crustal source for these intrusions, suggesting that they derive from the partial melting of metasediments (Esmaeily et al., 2005).

A similar metamorphic setting was described by Bröcker et al. (2014) north of Birjand, in the Anjul area: protoliths were attributed to the Semshak formation and migmatites and granitic intrusions dated by U-Pb (on zircon cores from leucosomes) between 169 and 168 Ma, thus close to the age of Deh-Salm regional metamorphism. In the case of Anjul, two younger ages were also obtained: ~110 Ma, by U-Pb dating of zircon overgrowths, and 102-96 Ma by Rb-Sr on K-feldspar or biotite separates. Bröcker et al. (2014) interpreted these two Cretaceous ages as marking the opening of the Sistan ocean and the cooling of the passive margin, respectively.

In this framework, our 149.6 ± 0.5 Ma Ar/Ar dating of biotite appears younger than the 165-160 Ma age proposed for regional metamorphism (Mahmoudi et al., 2010) yet older than the 110 Ma age thought to reflect the rifting stage (Bröcker et al., 2014). Although further age determinations are needed, this plateau age precludes mixing of different biotite populations and thus seems to reflect a distinct thermal event. We tentatively propose that this ~150 Ma event could represent cooling of regional metamorphic rocks or, since age constraints on gabbros and radiolarites suggest that the Sistan ocean is already open by ~120-110 Ma, a thermal event associated with the onset of rifting.

10.2.4. Summary of the main metamorphic events recorded in the Sistan orogen

Figure 17 summarizes the major metamorphic events associated with the Sistan orogeny. Whether the older, ~150 Ma age reflects a thermal event associated with rifting or cooling of the older Mid-Late-Cimmerian regional metamorphism of Deh-Salm is unclear. The oldest Sistan metamorphism, at ~106 Ma, corresponds to amphibolite facies recrystallization of oceanic gabbros (see section 6). The second one is the HP-LT blueschist to eclogitic facies marking subduction of the Sistan ocean beneath the Afghan Block, dated at 86 ± 3 Ma (Fotoohi Rad et al., 2005,2009; Angiboust et al., 2013; Bröcker et al., 2013; Kurzawa et al., 2017; Bonnet

et al., 2018). The third one is marked by lawsonite-bearing metasediments and metamorphic soles found at the base of the Neh ophiolite, which advocate for intra-oceanic slicing/subduction starting between 74 and 72 Ma. This intra-oceanic thrusting would account for the later obduction of the Neh ophiolite onto the Lut Block. Last, metasediments recording contact metamorphism, which are located in the vicinity of the granitoids intruding both the Lut block and the southermost exposures of the Neh ophiolitic complex, are inferred to be dated at ~50 Ma. Some of these rocks may testify to metamorphic conditions marking incipient collision in the Sistan orogen.

10.3. Tectonic evolution of the northern Sistan orogen and regional implications

Based on the synthetic cross-section of the northern Sistan orogen and the tectono-metamorphic events documented here (Figs. 3, 16, 17), the following section, together with Figure 18, propose a tentative reconstruction of the main geodynamic stages of the Sistan orogeny, from the rifting stage to the present.

10.3.1. Rifting and slow-spreading ocean basin (Cretaceous)

The oldest evidence in support of an oceanic domain between the Lut and Afghan Blocks was provided by K-Ar dating of amphibole from a gabbroic intrusion at 124 Ma (Delaloye and Desmons, 1980), in agreement with the Early Aptian biostratigraphic ages of radiolarian chert interlayered with basalts in the ophiolitic sequence (~120 Ma; Western Unit, Sulabest area: Babazadeh and De Wever, 2004). Other age constraints obtained by biostratigraphy (of radiolarites: Ozsvárt et al., 2020), U-Pb zirgon dating of leucogabbro (Zarrinkoub et al., 2012a) or $^{40}Ar/^{39}Ar$ step heating of amphibole from gabbro (Figs. 13a) give a consistent (minimum) Albian age between 113 and 106 Ma for the ophiolite. This indicates that the rifting stage must predate the Early Aptian. As a result, the Barremian to Aptian Orbitolina limestone (Maurizot et al., 1990) found on both the Lut and Afghan Blocks could be broadly contemporaneous with

the rifting of the Sistan ocean. Sediments found in the footwall of normal faults on the Afghan Block are nevertheless somewhat older, possibly pointing to an even earlier extension/rifting stage.

Geochemical investigations of the Sistan ophiolite show that the crustal section of the ophiolite, whenever present, essentially comprises N-MORB basalts and gabbros. Associated depleted harzburgite is interpreted as residual mantle, following melting. However, depending on the proxy used (i.e., #Cr in spinel, Ti in clinopyroxene or trace element modelling), contrasting degrees of partial melting were proposed to produce these N-MORB and/or the residual depleted harzburgite, from low (Zarrinkoub et al., 2012a) to high (Moazzen et al., 2006) and in one or several melting stages (Saccani et al., 2010). Some E-MORB were interpreted as coming from an interaction between the DMM and an enriched deeper source (Saccani et al., 2010; Zarrinkoub et al., 2012a), whereas rare, supra-subduction zone affinity magmatic rocks were interpreted as produced by a DMM source fluxed by subduction-derived fluids (Saccani et al., 2010; Zarrinkoub et al., 2012a). Our structural observations on the ophiolitic sequence show that the Sistan ophiolite exhibits all the characteristics of a fossil slow-spreading ocean, implying that the last partial melting stage was low (e.g.: Cannat et al., 2009; Lagabrielle et al., 2015; Eddy et al., 2017; Escartín et al., 2017), and that some of the early oceanic detachments are probably partly preserved (Fig. 18a).

10.3.2. Subduction beneath the Afghan margin (~90-55 Ma?)

Initiation of E- to NE-dipping subduction of the Sistan ocean below the Afghan Block is difficult to date and locate precisely, but several markers support its existence from at least 90 Ma (Turonian, Fig. 18a), and possibly before: (1) Peak burial of the blueschist and eclogite facies units of the Ratuk complex was dated at 86 ± 3 Ma by several methods (Bröcker et al., 2013; Kurzawa et al., 2017; Bonnet et al., 2018); (2) The flexural flysch basin, whose depocenter lies on the Afghan block, expands during the Senonian (Coniacian to Maastrichtian:

90-72 Ma; Tirrul et al., 1983; Maurizot et al., 1990a; 1990b); (3) Typical juvenile arc magmatic rocks and/or high silica adakites are intrusive or interbedded into the Sefidabeh flysch basin, the Western Unit and the HP-LT units. U-Pb dating on zirgon gave ages between c.a. 86 and 71 Ma for this magmatism (Zarrinkoub et al., 2012b; Jentzer et al., 2020). (4) The mains thrusts indicate W/SW-vergent deformation. Unlike the HP-LT suture zone located between the Neh complex and the Afghan Block, no suture zone exists between the Neh complex and the Lut Block, making the hypothesis of a west-dipping subduction zone below the Lut Block (e.g., Pang et al. 2012) difficult.

After the formation of cold (7°C km^{-1}) eclogites, the formation of high silica adakites (requiring partial melting of the downgoing slab crust) reflects a change in the thermal regime of the subduction and points to a likely slab breakoff event at ~80 Ma (see discussion in Jentzer et al., 2020 ; Fig. 18b). Incidentally, the presence of high silica adakite dykes and sills intruding the Western Unit implies that this unit belonged to the upper plate of the subduction system. Since the Western Unit comprises non-metamorphosed ophiolitic rocks (i.e., serpentinized peridotite, gabbroic intrusions and basalts), it could either represent a portion of the Sistan ocean or a piece of forearc and/or ocean-continent transitional domain connected to the Afghan margin.

Assuming that the Sistan ocean opened at ~125 Ma and subduction started below the Afghan Block at 90 Ma, the slow-opening Sistan ocean (<~2cm.y^{-1}) was probably not wider than ~700 km.

10.3.3. Intra-oceanic subduction and obduction of the Neh complex (~73 Ma)

Two types of metamorphic rocks provide evidence for a specific deformation event affecting the Sistan ocean during the Upper Campanian: (1) The strongly schistosed, 10-20 m thick horizons of amphibolite facies metabasic and metasedimentary rocks underlying the ophiolite, best exposed in the south of the study area and near Sarbisheh (Figs. 4), with an

inferred metamorphic age around 72 Ma (Figs. 15). Their structural characteristics and metamorphic peak, around 700°C ± 50 and 0.6-0.7 GPa (Figs. 14), suggest that they represent a metamorphic sole and therefore mark the initiation of intra-oceanic subduction (e.g., Wakabayashi and Dilek, 2003; Agard et al., 2016; Plunder et al., 2016; Guilmette et al., 2018; Dubacq et al., 2019); (2) The lawsonite-bearing metasediments located at the base of the ophiolitic Unit 2 (Figs. 7 and 11g), south of Birjand, with a coincident metamorphic age between 74 and 72 Ma, which indicate a synchronous intra-oceanic thrusting, though possibly of a lesser extent (i.e., with pressure of 0.4 GPa advocating for only ~15 km of burial). These tectono-metamorphic events are interpreted here to reflect initiation of intra-oceanic thrusting and/or subduction at 73 ±1 Ma, whose amplitude was larger in the eastern part of the study area (metamorphic soles; Sarbisheh, Malabad) than in the western part (lawsonite-bearing samples; Birjand ridge). This event si coeval with large-scale plate reorganization further east, with Indian starting its northward migration and obduction of ophiolites east of the Afghan block (i.e., Bela and Muslim Bagh ophiolites, Gnos et al., 1997).

In order to account for the emplacement of the obducted Neh complex onto the Lut Block, this intra-oceanic subduction must have been dipping to the NE (in present-day coordinates, i.e. without correcting for the ~30° Cenozoic rotation; Mattei et al., 2015; Figs. 18c,d, 19). Further evidence may come from the existence of supra-subduction ophiolitic material reported in the south of the study area (near Barak; Saccani et al., 2010), but age constraints are lacking for now. Likewise, the ~71 Ma intrusive adakitic magmatism described in the Neh complex (Zarrinkoub et al., 2012b) could support intra-oceanic subduction, during which small volumes of adakitic melts can be produced by partial melting of the downgoing slab crust (<5-10% vol at 850°C; Agard et al., 2016).

At the same in the eastern part of the orogen, the HP-LT metamorphic units are already exposed as shown by the presence of unconformable Maastrichtian deposits (Bonnet et al.,

2018). The HP-LT units were exhumed along the suture, and now exposed into the thinned Afghan margin, at 4 mm yr^{-1} on average. Lower Maastrichtian sedimentation in the innermost part of the orogen is characterized by a drastic regression (from deep Senonian flysch to Maastrichtian conglomerate and reefal limestone; section 5) leading to the individualization of distinct sedimentary basins, i.e. the Sefibadeh basin with shallower deposits than the finely laminated turbidites of the Neh basin (Tirrul et al., 1983).

These important changes could relate to the slowdown of the main NE-dipping subduction, as a result of the suspected ~80 Ma slab breakoff (Jentzer et al., 2020), and/or to some large-scale reorganization of regional geodynamics

10.3.4. End of obduction and onset of collision between the Lut and Afghan Blocks (~55-50 Ma)

After the beginning of intra-oceanic subduction at 74-72 Ma, another change occurs during the Eocene (Fig. 18e), marked by: (1) The change from Upper Paleocene flysch-dominated sediments to Eocene coarse grain continental conglomerates and molasse-type sediments (i.e., 'red beds'). In the SW part of the Neh complex, Eocene deposits are still fine grained with thin argilite layers, indicating a deeper environment than for the conglomerate deposits and suggesting southwestward migration of depocenters with time; (2) A deformation event is revealed by the unconformity of the Eocene deposits onto Paleocene sediments. Tirrul et al. (1983) recognized two stages of deformation of the Eocene deposits, whereas the Oligocene conglomerates are much less deformed; (3) Obduction movements, i.e. the respective movements of the Lut Block and Neh complex, have largely ended by then (Fig. 18e) since a weakly deformed granitoid intrusion dated at 49.6 ± 0.2 Ma cuts through both units (Fig. 15l).

The change in sedimentary regime and the unconformity between the Paleocene and Eocene deposits suggest that the collision began during the Eocene, between ~55 Ma and 50 Ma (according to current biostratigraphic knowledge). Syn-kinematic emplacement of

granitoids cutting through the odbuction nappe thrust could be associated with the first collisional movements.

10.3.5. Events following the onset of collision (after ~45 Ma)

A large calc-alkaline (to alkaline) magmatic production develops from the Mid-Eocene onwards (46-25 Ma; Fig. 18f, g). Two stages were identified (Camp and Griffis, 1982; Pang et al., 2013; Mohammadi et al. 2016): the older one (46-40 Ma; Lutetian) reflects mixed contributions from mantle and upper crustal sources. Partial melting of the upper crust was tentatively associated with the onset of lithospheric delamination; the younger one <30 Ma (Rupelian) has a dominant mantle source and was interpreted as resulting from complete delamination and formation of a wide asthenospheric window.

Shortening of the Sistan orogen prevailed during the first period (i.e. possible inception of delamination), as evidenced by the unconformity between the Oligocene and the Eocene deposits. In contrast, only minor shortening is observed after the beginning of the Oligocene (~30 Ma; Tirrul at al.,1983). Neogene conglomerates unconformably overlying older deposits indicate weak folding and faulting and reworking of earlier contacts (Walker and Khatib, 2006; Jentzer et al., 2017).

Tectono-magmatic events resumed from the Mid-Late Miocene onwards, as shown by alkaline magmatism along major strike-slip faults (marking asthenospheric upwelling along major lithospheric discontinuities;-e.g., Pang et al., 2012). Three groups of active faults were recognized: (1) N-S to NNE–SSW dextral strike-slip faults, which accommodated up to 95 km of motion; (2) ENE-WSW senestral conjugate faults and (3) NW–SE trending thrust faults. Walker et al. (2004) proposed that these faults initiated at 7-5 Ma (during the Messinian).

The dextral strike-slip faults likely accommodated the counterclockwise rotation of at least 35° which affected the Central Iranian microcontinent, including the Lut block, since the Mid-Late Miocene (Mattei et al., 2015). These deformations likely relate to the increase in the

intensity of the Arabia-Eurasia collision since 15-10 Ma (Ballato et al., 2011), as shown by the progressive alignment of the main horizontal stress component across Iran and in the northern Sistan (Jentzer et al., 2017).

10.4. Tectonic significance of the Sistan orogen within the Neotethyan realm

10.4.1. The Sistan ophiolite *vs* the other ophiolites of the 'Inner ophiolite belt'

The Sistan ophiolite is one amongst the many ophiolite belts preserved, across the Iranian territory, between the Neotethys and Paleotethys suture zones (Fig. 1b; Stöcklin, 1968; Moghadam and Stern, 2015). These Mesozoic ophiolitic domains (Table 2 and references therein) have commonly been interpreted as marginal basins opened within the upper plate of the Neotethys subduction system, mostly during the Cretaceous (Agard et al., 2011), although their exact tectonic evolution and mutual relationships remain obscure. These (partly independent?) basins likely developed along inherited boundaries separating the Cimmerian Blocks.

The Sistan ophiolite is the most extensive, along with the Makran ophiolites (i.e., Band e Zeyarat, Fanuj-Makutan). Despite large uncertainties on the timing of their initiation, these ophiolitic basins can be collectively regarded as having lasted between ~140-120 and ~70-55 Ma and were already closed by the Paleocene to Eocene (Table 2). A slightly diachronous opening of these basins is suspected, for example (i) to the north, in the Sabzevar domain (Late Jurassic?; Lindenberg and Groler, 1984; Omrani, 2017; Stöcklin, 1974), possibly coeval with the Waras Panjaw ocean in Afghanistan or the Caspian sea, or (ii) to the south in the Nain-Deshir-Baft-Bad e Zeyarat, Fanuj-Maskutan (145 Ma or older?; Saccani et al., 2018; Hunziker et al., 2015; Ghazi et al., 2004; Ghazi et al., 2012; Moghadam and Stern, 2015, Pirnia et al., 2020), but ages are still somewhat contradictory.

The Sistan differs in several ways: it is the only one exposing subduction-related cold HP-LT metamorphic rocks and arc magmatic rocks, km-scale unmetamorphosed slices of ophiolite

from a former slow spreading ocean and rather extensive metamorphic soles. These specificities can be questioned: was the Sistan ocean initially larger or is it better preserved because of its orientation or because of different obduction processes (i.e., with respect to mechanisms and/or intensity)?

Contrary to the many ophiolites worldwide (Agard et al., 2016, 2020), most commonly formed in a supra-suduction zone environment (Dilek and Furnes, 2019), and to several other Neotethyan ophiolites (Semail, Nain-Baft), the metamorphic soles of Sistan only exhibit intermediate (MP-MT) conditions and in particular no granulite facies HT soles (Soret et al., 2017). The Sistan ophiolite is also different in that it is mainly N- to E-MORB-type, it is older than the metamorphic sole, no HP-LT metamorphism is observed in the underthrust continental margin and no significant extension postdates ophiolite emplacement (contrary to the Semail ophiolite; Fournier et al., 2006; Hansmann et al., 2017; Ninkabou et al., 2021). Similar characteristics are found for the Sevan ophiolite (Hässig et al, 2015; Rolland et al., 2019).

A tentative explanation could be that the ~73 Ma intra-oceanic subduction within the Sistan ocean reached shallower depths than in the main Neotethys ocean, thereby never leading to the formation of a supra-suduction ophiolite like the Semail ophiolite. This could relate to the slow spreading character of the Sistan ophiolite, with a thick and weak serpentinized zone at its base hampering the formation of HT metamorphic soles and promoting strain localization at shallower depths compared to other large-scale ophiolites (hence without proper slabitization: Agard et al., 2020).

10.4.2. Sistan orogeny within the Neothethyan realm

A qualititative paleotectonic reconstruction, with the aim to set back the tectonic evolution of the Sistan orogen with the larger Neotethyan realm and address uncertainties on the initial orientation of the Sistan ocean (see section 2), is proposed in Figure 20. It places emphasis on:

(i) the opening of the Sistan basin around 125 Ma (Fig. 20b) and inception of the main Sistan subduction zone below the Afghan Block around 100-90 Ma, following the regional-scale plate reorganization (Agard et al 2006; Matthews et al., 2012) marked by other obduction events in the Neotethys (e.g., Turkey, Armenia, ~104-88 Ma; Zagros: Neyriz, 95 Ma; Lanphere and Pamic, 1983; Pourteau et al., 2018; Oman, between 104 and 95 Ma; Rioux et al., 2016; Guilmette et al., 2018; Burg, 2018 and references therein; Fig. 20c) and widespread blueschist exhumation (Monié and Agard, 2009; Angiboust et al., 2016). This age also corresponds to the beginning of the transform motion between India and Africa (Rodriguez et al., 2020 and references therein).

(iii) the initiation of intra-oceanic subduction within the Sistan oceanic domain at ~73 Ma, ultimately leading to the emplacement of the ophiolitic Neh complex onto the Lut Block. This period coincides with a second major reorganization of the eastern Neotethys and Indian ocean (Gaina et al., 2015), marked by the onset of fast convergence of the Indian continent towards Eurasia and obduction of the Masirah, Ra's Madehah, Bela, Muslim Bagh or Spontang ophiolites between 70 and 65 Ma (Gnos et al., 1997; Corfield et al., 2001; Figs. 20d).

During the mid-Jurassic, following Paleotethys closure and inception of Neotethys subduction, a magmatic arc starts forming at ~175 Ma along the Sanandaj-Sirjan and Bajgan-Durkan domains (Fig. 20a; e.g. Stampfli and Borel, 2002; Agard et al., 2011; Seton et al., 2012; Burg, 2018). Fragmentation of the upper plate starts in the Mid-Jurassic to the east of the future Sistan domain, with the opening of the back-arc Waras-Panjaw basin separating the Band-e Bayan and Helmand Blocks (Fig. 20a). A similar yet slightly younger (Mid to Late Jurassic) evolution affects the Iranian region, as shown by the opening of the south Caspian basin, possibly extending eastward to Sabzevar and Torbat-e-Heydarieh, and extensional movements in the Kopeh-Dagh (Stöcklin, 1974; Brunet et al., 2003; Robert et al., 2014;Omrani, 2017). To the south of the CEIM, the magmatic evolution advocates for back-arc extension at the rear of

the Neotethyan subduction zone, in the future Makran region (Hunziker et al., 2015; Burg, 2018), in the Kandahar basin (Siehl, 2017) and possibly along the Sanandaj-Sirjan zone (Azizi and Stern, 2019).

During the Early Cretaceous (Fig. 20b), extensional movements lead to rifting and to the formation of the Fannuj ocean between the CEIM et Bajgan-Durkan (e.g. Pirnia, 2020; Sepidbar et al., 2020), extending to the northwest in the future Nain-Baft domain up to the Dorouneh-Grat Kavir fault, suspected to have been active at the time (e.g. Mattei et al., 2015). In contrast, on the Afghan side, the Waras-Panjaw ocean is progressively closing (Montenat, 2009). Opening of the Sistan basin in an oblique transtensional (pull-apart) setting, as shown in Figure 20b, would explain the contrasting evolution between the Lut and Afghan transects, as well as its peculiar N-S orientation. Similar settings were proposed for the oceanic domain where the future Pakistani Bela and Muslim Bagh ophiolites formed along the Chaman fault or for the north-Somalia basin (Gaina et al., 2015), or in the Caiman sea (Leroy et al., 2000). This geometry would be consistent with the existence of a STEP fault (Govers and Wortel, 2005) separating the sinking Neotethyan slab across the present-day Neh fault.

Between 115 and 85 Ma, the Arabia-Eurasia convergence rate steadily increases and changes orientation (Fig. 20c; e.g. Agard et al., 2006; DeMets et al., 2010), leading to a major reorganization in the Neotethys, with initiation of intraoceanic subduction zones at 105-95 Ma, leading to the formation and emplacement of several ophiolites and intraoceanic arcs (e.g. Guilmette et al., 2018; Pourteau et al., 2018; Bonnet et al., 2020). We relate these kinematic changes to the onset of closure of the Iranian marginal basins: to the north, the metamorphic evolution in the Sabzevar domain (through the presence of granulites similar to metamorphic soles; Rossetti et al., 2010) likely advocates for the onset of subduction, and the Waras-Panjaw ocean is closed (Montenat, 2009; Siehl, 2017). In the Nain-Baft domain, metamorphic soles marking closure were dated at 100-90 Ma (Shafai Moghadam et al., 2009). In the south, in the

Makran region, arc magmatism is still active and blueschists are exhumed at 100-95 Ma (Burg, 2018), as along the southern Sanandaj-Sirjan zone (Agard et al., 2006; Angiboust et al., 2016). In the Sistan region, peak burial of blueschists and eclogites at ~86 Ma (Bröcker et al., 2013; Bonnet et al., 2018) indicates that subduction has been active since a few millions years at least.

During the Campanian (~75 Ma; Figs. 20d), most of the Iranian marginal basins are actively closing. The Sistan ocean records the onset of intraoceanic shortening at ~73 Ma, contemporaneous with the northward migration of India, changes in subduction dynamics and obduction movements marked by the emplacement of the Masirah, Muslim Bagh, Bela and Spontang ophiolites (Gnos et al., 1997; Corfield et al., 2001; Gaina et al., 2015). The Sistan ocean, probably due to its central location in the Neotethyan realm, appears to have strikingly recorded the major plate reorganizations at 100-90 Ma and 75-70 Ma which triggered the main obduction events of the Neotethys (Gnos et al., 1997; Agard et al., 2007; Gaina et al., 2015). To the east of the Sistan domain, magmatic arcs form in the southern Afghan Block (Chagai Hills; Ras Koh, where small ophiolitic remnants are also found). Whether these represent accreted forearcs or formed within a lateral equivalent of the microcontinental Kabul Block is unknown (Siehl, 2017; Burg, 2018). Maastrichtian sediments unconformably overlying the Ras Koh, Makran, Baft and Deshir ophiolites indicate that these were obducted by then (later Paleocene sediments in the Nain ophiolite may indicate diachronous closure, younging towards the NW).

During the Lower Eocene, obduction of the Sistan and Sabzevar ophiolites is over, all Iranian marginal basins bassins are closed except the south Caspian basin. From the Eocene onwards, calc-alkaline magmatism affects most of Iran, along the Urumieh–Dokhtar arc, from the Alborz to Kopeh Dagh, and in the Lut Block west of Sistan (Fig. 20e). This episode reflects large-scale distributed extension triggered by lithospheric delamination and/or Neotethyan slab retreat (Omrani et al., 2008; Agard et al., 2011; Verdel et al., 2011; Rossetti et al., 2014).

11. Conclusions

(1) This study provides new insights on the units and structural organization of the Sistan orogenic belt. The Afghan Block and Western Unit occupy the highest structural position, through which the HP-LT suture zone is exposed as a tectonic window, while the Neh complex is represented by a continuous, weakly deformed ophiolite thrust to the SW over the Lut Block. Sediments of the Neh complex evidence a progressive southwestward migration of depocenters and burial (up to ~275°C on average) in a warm thermal gradient (50°C.km^{-1}). Major thrusts within the Neh complex dip to the NE and post-emplacement shortening is relatively modest (30-50 km). The ophiolitic part of the Neh complex, which attests to a former slow- to ultra-slow spreading ocean with extensive hydrothermal alteration, exposes in its basal part a 74-72 Ma metamorphic sole. Ophiolite emplacement was largely achieved by 55-50 Ma when granitoids intruded both the ophiolite and the Lut Block. Two types of metamorphism are observed in the Lut Block: contact metamorphism (andalusite/sillimanite- and biotite-bearing micashists) releated to the ~55-50 Ma granitoid intrusions, possibly lightly imprinted by later collision; regional metamorphism, marked by the presence of micashists and migmatites, dated at ca. 150 Ma and probably associated with the Mid- to Late Cimmerien events which affected Central Iran.

(2) Based on the tectono-metamorphic data and events documented here and literature data, a tentative reconstruction of the geodynamic evolution of the Sistan orogen is proposed: (i) between 124 and 90 Ma, and possibly earlier, the slow- to ultra-slow spreading Sistan ocean was active, suggesting a maximum width of ~700 km; (ii) since 90 Ma at least, NE-dipping subduction of the Sistan ocean below the Afghan margin was active: this was responsible for the flexural subsidence a deposition of the Senonian flyschs, the formation and exhumation of blueschists and eclogites and the emplacement of calc-alkaline and adakitic arc magmatism; (iii) between 74 and 72 Ma, an intra-oceanic NE-dipping thrusting or subduction was initiated,

as attested by metamorphic sole rocks, which ultimately led to the obduction of the Neh complex ophiolitic domain onto the Lut Block, largely completed by 55-50 Ma; (v) Eocene collision, marked by a drastic change in sedimentation, was only moderate, with around 30-40 km of shortening, and rather short-lived, being mostly achieved during the Oligocene. Later, post-collisional shortening was limited (probably ~10-20 km).

(3) In a Neo-Tethyan perspective, the comparison between the tectonic evolution of Sistan and those of the other Inner ophiolite belts of Central Iran suggests that: (i) the Sistan ocean formed as an independent pull-apart basin along an inherited transfer fault located between Iran and Afghanistan, as a result of transtensional movements and contrasting slab dynamics along the Neo-Tethyan subduction zone; (ii) the triggering of the ~90 Ma main subduction zone coincides with a major kinematic change (in both velocity and direction) within the Neo-Tethyan realm, coeval with the exhumation of Zagros and Makran blueschists and the obduction of the Western Tethyan ophiolites (e.g. Oman, Turkey); (iii) initiation of the 74-72 Ma intra-oceanic thrusting/subduction coincides with the obduction of the Eastern Tethyan ophiolites (e.g. Bela, Muslim Bagh, Spontang) and the closure of most of the Inner Iranian ophiolitic basins. The Sistan orogen, with its central position in the Tethyan realm, therefore appears to have recorded all the main tectonic stages accompanying Neo-Tethyan closure.

Acknowledgements

We feel indebted to the Geological Survey of Iran, and especially to Dr. Shahidi, to the geologists and all the staff (drivers, cooks and chief of camp) for their kindness, constant support and for enabling us to visit the region since 2014. This work was financially supported by the CNRS-INSU programs, by ISTeP lab of Sorbonne University and by the over-head of the project “Zooming in Between Plates” (Marie Curie International Training Network of the European Union’s Seventh Framework Program FP7/2007/2013/ under REA grant agreement

no. 604713). We would like to warmly thank M. Eric Delairis who produced the thin sections studied; M. Omar Boudouma for its help during SEM sessions; M. Michael Fialin and M. Nicolas Rividi for their techical support during microprobe analyses. Main thanks to M. Eric Barrier for taking the time to discuss tectonic reconstructions.

Appendix: Methods used

1. Analytical methods used

1.1. Mineral chemistry

The electron microprobes used for this study were Cameca SX-5 and SX-100 at Camparis (Sorbonne Université, 4 place Jussieu, 75005 Paris, France). Point measurements were made in classical analytical conditions (15 kV acceleration voltage and 10 nA beamcurrent allowing ~2 µm beam size in wavelength-dispersive spectroscopy mode) using diopside (Ca,Mg, Si), $MnTiO_3$ (Mn, Ti), orthoclase (K, Al), Fe_2O_3 (Fe), albite (Na) and Cr_2O_3 (Cr) as standards for calibration of elements indicated in parentheses. Elemental mapping has been carried out with identical voltage and an increased current (100 nA) with a counting time of 100 ms per point. Analyses were calibrated with the manufacturer's software using standards as point analyses (Pouchou and Pichoir, 1991). All analysis were sorted based on their structural formulae calculated with Fe^{3+} estimates using the method of Droop (1987) for garnet and clinopyroxene, and the method exposed in Leake et al. (1997) for amphibole. We considered all iron as ferric in epidote and lawsonite, and as ferrous in mica.

1.2. RAMAN spectroscopy and mineral determination

RAMAN spectroscopy on polished thin sections was used to identify the serpentine and the carbonate minerals. Following Schwartz et al, (2013), the spectral regions investigated to characterize serpentine species are from 150 to 1150 cm^{-1} and from 3600 to 3720 cm^{-1} because they include the lattice vibrational modes and the OH stretching mode region. The nature of

carbonate material was determined using the spectral region between 600 to 800 cm^{-1} as indicated in Kontoyannis and Vagenas (2000).

2. Thermometric methods used

2.1. Raman spectroscopy on carbonaceous material: Tmax estimation

The Raman spectrum of carbonaceous materials (RSCM) between 1100 and 1800 cm^{-1} can exhibit a characteristic graphitic band at ~1580 cm^{-1} and four defect bands at ~1200 (D4), ~1350 (D1), ~1500 (D3) and ~1620 (D2) cm^{-1}. The increase of temperature during diagenesis and metamorphism induces a progressive and irreversible loss of the defect bands, thus for a temperature >655°C, all the organic matter is changed into pure graphite. Nowadays, several calibrated methods using Raman spectra allow to quantify the maximum temperature (Tm) reached by the carbonaceous materials (CM) between 150°C and 655°C with an intrinsic error of ±50 °C (Beyssac et al., 2002; Lahfid et al., 2010; Kouketsu et al., 2014). In this study, we used for Tm ≥ 330°C the calibration from Beyssac et al. (2002) and the calibration from Lahfid et al. (2010) for Tm < 330°C.

Raman spectra were collected with a Raman microspectrometer (Renishaw inVia located at the ENS and at the IMPMC, both in Paris, France) on conventional petrographic thin sections. Textural position of the CM was carefully checked and the focus was made beneath the surface of a transparent adjacent grain to limit some potential parasitic effects. Analysis was performed in the center of the carbonaceous particles, using argon laser beam (514 nm, Spectra Physics) equipped with a LEICA 50 x magnification objective (0.5 numerical aperture) and using a circular polarization of the laser. The Raman scattered light was dispersed by wavelength using a holographic grating with 1800 lines/mm and detected by a CCD camera. The spectra were recorded in the 700 to 2000 cm^{-1} range (first order spectrum). For each sample between 11 and 20 coherent Raman spectra were obtained.

2.2. Ti in biotite: empirical thermometry

For metapelitic rocks saturated in Al, in Ti, and in Si (aluminosilicate, rutile or ilmenite and quartz bearing rock) and for biotite with XMg ≥ 0.275 and 0.04 < Ti < 0.6 apfu, the incorporation of Ti in octahedral sites of biotite depends on temperature. Henry (2005) proposed an empirical function linking Ti in biotite and temperature as defined in equation (A) with an uncertainty of ± 24°C. This relationship can be used between 0.3 and 0.6 GPa and 480 to 800°C. Presence of CM in the rock is recommended to use this geothermometer because CM buffers the oxygen and limits the formation of Fe^{3+}.

$$(A) \quad T = \left(\frac{\ln(Ti) - a - c(XMg)^3}{b}\right)^{0.333}$$

Where T is temperature in °C, Ti is the Ti content of the analysed biotite in apfu, XMg of the analysed biotite and a, b and c three adjustment coefficients respectively defined as:

a = -2.3594, b = $4.6482\ 10^{-9}$ and c = -1.7283.

3. Thermobarometric methods used

3.1. Plagioclase-amphibole

Holland and Blundy (1994) proposed an edenite-richterite thermometer (edenite + albite = richterite + anorthite), based on the exchange (Na Si)-(Ca Al) between amphibole and plagioclase as described in the equation B. This method can be used over a broad range of bulk rocks composition (with or without quartz), in a range of 400 to 1000°C and 0.1 to 1.5 GPa with an uncertainty around ± 40°C.

$$(B) \quad T = \frac{78.44 + Y_{ab\text{-}an} - 33.6\, X^{M4}_{Na} - (66.8\text{-}2.92P)X^{M2}_{Al} + 78.5X^{T1}_{Al} + 9.4X^{A}_{Na}}{0.071 - R \ln\left(\frac{27\, X^{M4}_{Na}\, X^{T1}_{Si}\, X^{pl}_{an}}{64\, X^{M4}_{Ca}\, X^{T1}_{Al}\, X^{pl}_{ab}}\right)}$$

Where the Yab-an term is given by: for Xab>0.5 then Yab-an = 3 kJ otherwise Yab-an = 12.0 (2Xab – 1) + 3 kJ, T is the temperature in Kelvins, P is the pressure in kbar and the $X^{\Phi i}$ terms denote the molar fraction of species (or component) i in phase (or crystallographic site) Φ.

Molina et al. (2015) proposed a barometer using the Al-Si partitioning between plagioclase and Ca-amphibole as described in equation (C). This method can be used over a broad range of bulk rocks composition (with or without quartz) but only with amphibole containing more than 0.02 apfu of Ti and more than 0.05 apfu of Al_{VI} , in a range of 650 to 1050°C and 0.15 to 0.23 GPa with an uncertainty ≤±0.2 GPa.

$$(C)\quad P = \frac{8.3144\ T \ln D^{pl/amph}_{Al/Si} - 8.7\ T + 23\ 337\ X^{T1}_{Al} + 7\ 579\ X_{ab} - 11\ 302}{-274}$$

Where $Dpl/amph_{Al/Si} = (Xpl_{Al}/Xpl_{Si})/(Xamph_{Al}/Xamph_{Si})$: molar plagioclase/amphibole Al-Si partition coefficient, T is the temperature in Kelvins, P is the pressure in kbar and the $X^{\Phi i}$ terms denote the molar fraction of species (or component) i in phase (or crystallographic site) Φ.

Using both B and C equations for Ca-amphibole and plagioclase bearing metamorphic rocks, P-T conditions can be estimated between 650 and 1000°C and 0.1 to 1.5 GPa with an uncertainty of ± 40°C and ± 0.2 GPa.

3.2. Ti-Al amphiboles

In meta-basaltic rocks saturated in Ti, Al and Ti content of Ca-amphibole can be used to estimate semi-quantitatively P-T conditions (Ernst and Liu, 1998). This method has been tested for natural and experimental samples on a range of temperature between 400 and 1100°C and a range of pressure between 0 and 2.2 GPa but the best fit between this method and independent P-T estimations have been obtained for low grade metamorphism. Amphibole isopleths do not seem to be affected by small variations in bulk rocks composition. During cooling, the exsolution in amphibole of rutile, titanite or ilmenite which are Ti bearing phases can lead to an underestimation of the Ti content of the amphibole and must be considered.

3.3. GB and GBAQ: empirical thermobarometry

Wu (2017) proposed a garnet–biotite–aluminosilicate–quartz (GBAQ) geobarometer which can be used for a broad garnet and biotite composition and under P–T conditions from

450 to 950°C and from 0.1 to 1.7 GPa with a random error inferred to be around ±0.18 GPa. This geobarometer need to be used the type of aluminosilicate bearing in the rock and an estimated temperature which is obtained by the geothermometer garnet-biotite (GB) from Holdaway (2000). In this method the temperature is calculated with an estimated uncertainty of ±25°C, using the Fe-Mg partition coefficient between garnet and biotite and an estimation of pressure. GBAQ geobarometer and GB geothermometer can be simultaneously applied to iteratively estimate metamorphic P–T conditions. These methods are applied only for low value of ferric iron in biotite (around 11 ± 3 mol %) which can be buffered by ilmenite and/or graphite in the rocks. For samples without aluminosilcate, only GB geothermometer was used.

4. Thermodynamic modelling

Pseudosections were calculated using Perple_X (6.8.6 version, Connolly, 2005, 1990). with the internally consistent thermodynamic dataset and equation of state of H_2O used come from Holland and Powell (2011), the useful solution models and the bulk rocks composition here obtained after crushing, dissolution and ICP-OES iCap 6 500 analysis performed in Nancy CRPG (results on Table 8. 4). For metabasite sample (15b-15c), the system used was Na_2O–CaO–K_2O–FeO–MgO–Al_2O_3–SiO_2–H_2O–TiO_2 and the solution models considered were: amphibole, augite and melt with thermodynamic properties from Green et al. (2016), garnet, orthopyroxene, white mica, biotite, chlorite and ilmenite with thermodynamic properties from White et al. (2014), Holland and Powell (2011) for epidote, White et al. (2002) for titanite and Holland and Powell (2003) for feldspar. The amount of water was chosen at 1 wt%. All the iron was considered as ferrous. For metapelitic samples (14-29a and 16-72) the system used was Na_2O–CaO–K_2O–FeO–MgO–MnO–Al_2O_3–SiO_2–H_2O–TiO_2 and the solution models considered were: garnet, chloritoid, staurolite, white mica, biotite, chlorite, ilmenite and melt with thermodynamic properties from White et al. (2014), Holland and Powell (2011) for epidote and Holland and Powell (2003) for feldspar. The amount of water was chosen at 2.5 wt% for

sample 14-29a and 2 wt% for sample 16-72. All the iron was considered as ferrous. By minimizing Gibbs free energy, the software calculates for each desired P-T conditions the sTable 8. mineralogical assemblage and the composition of each solid solution. These models were compared to the natural mineral compositions obtained by microprobe analysis to estimate the P-T conditions of the mineral assemblages of our samples.

Table 3 : Bulk rock composition used for pseudosection

5. Geochronology methods used

5.1. Ar-Ar

Samples were carefully chosen for dating so that: they bear minerals with enough K to be dated with the Ar–Ar method (white mica, biotite or amphibole) and these minerals constitute a well-understood paragenesis in the rock. Selected samples were crushed and sieved; single grains were handpicked under binocular microscope and cleaned in ultrasonic bath with acetone and distilled water. They were packaged in Al foils and irradiated for 40 hours in the core of the Triga Mark II nuclear reactor of Pavia (Italia) with several aliquots of the Fish Canyon sanidine standard (28.03 ± 0.08 Ma;Jourdan and Renne, 2007) as flux monitor. Argon isotopic interferences on K and Ca were determined by irradiation of KF and CaF_2 pure salt. Argon analyses were performed at Géosciences Montpellier (France) with two analytical devices that each consist of: (a) an IR-CO_2 laser of 100 kHz used at 5–15% during 60 s, (b) a lenses system for beam focusing, (c) a steel chamber, kept at 10^{-8}–10^{-9} bar, with a drilled copper plate, (d) an inlet line for purification of gases including two Zr–Al getters, (e) a multi-collector mass spectrometer (Argus VI fromThermo-Fisher). A custom-made software controls the laser intensity, the timing of extraction/purification and the data acquisition. To measure the Ar background within the system, one blank analysis was performed every three sample analyses. ArArCalc© v2.5.2 was used for data reduction and plotting. The one-sigma errors reported on

plateau, isochron and total gas ages include the error on the irradiation factor J. Atmospheric ^{40}Ar was estimated using a value of the initial $^{40}Ar/^{36}Ar$ of 295.5.

5.2. U-Pb in titanite

In situ U-Pb analyses of titanites were performed by laser ablation split-stream inductively coupled plasma mass spectrometry (LASS ICP-MS, Kylander-Clark et al., 2013) at the University of California, Santa Barbara. Samples were ablated using a Photon Machines 193 nm ArF ultraviolet laser with a laser fluence of ~1 $J.cm^{-2}$, and U-Pb isotopes and trace elements were analysed simultaneously on the same 35 µm spots, using a Nu Instrument Plasma 3D multi-collector inductively coupled plasma mass spectrometer (MC-ICP-MS) and an Agilent 7700X quadrupole inductively coupled plasma mass spectrometer (Q-ICP-MS), respectively. The laser was fired twice at 50% power to remove surface contamination and this material was allowed to wash out for 15 s. Samples were then ablated at 4 Hz for 15 seconds with a laser energy of 1 $J.cm^{-2}$. Analyses of unknowns were bracketed by analyses of matrix-matched titanite standard MKED (1518.87 ± 0.31 Ma isotope dilution thermal ionization mass spectrometry date; Spandler et al., 2016), which was used as a primary standard for U-Pb analyses. Secondary titanite standards BLR (1047.1 ±0.4 Ma concordia date; Aleinikoff et al., 2007), FC (28.395 ± 0.049 Ma Concordia date; Schmitz and Bowring, 2001) and Y17 (388.6 ± 0.5 Ma isotope dilution thermal ionization mass spectrometry data; Spencer et al., 2013) were included to monitor accuracy and internal error. We obtained ^{207}Pb-corrected $^{206}Pb/^{238}Pb$ ages (using Stacey-Kramers common Pb correction in IsoplotR; Vermeesch, 2018) of 1033.41 ± 3.43 Ma for BLR (n=17), 27.99 ± 0.14 for FC (n=10), and 391.94 ± 1.71 Ma for Y17 (n=11). These ages are accurate to within 1.3%, 1.4% and 0.8% of standard values, respectively.

All unknowns were additionally bracketed by analyses of international glass standard NIST612, that was used as a primary standard for trace elements (Pearce et al., 1997), using ^{44}Ca as the internal standard element (assuming 19.2 wt.% Ca). The spectra were reduced using

Iolite v2.5 (Paton et al., 2011), error correlations were recalculated after Schmitz and Schoene (2007), and discordia ages were calculated using IsoplotR (Vermeesch, 2018).

Captions

Figure 1. Geological setting of the Sistan in the Tetyan realm. **a)** Elevation map with GPS horizontal velocities, in Eurasia-fixed reference frame, for the eastern Alpine–Himalayan belt (modified after Vernant et al., 2004), the main Tethyan ophiolites (modified after Khan et al., 2006), the Paleo- and Neo-Tethyan sutures and the main continental blocks implied in the Tethyan orogeny. **b)** Shaded relief map from ETOPO1 (http://www.ngdc.noaa.gov/mgg/global/relief/ETOPO1) with the main Paleo- and Neo-Tethyan sutures, the main faults (in *italic*), the orogenic belt (in **bold**) neighboring the Sistan and the supposed marginal basins associated with the closure of the Neo-Tehtys (in orange).

Figure 2. The Sistan orogen **a)** Elevation map with the location of the main Iranian ophiolites, the Cenozoic magmatic provinces (modified after Paul et al., 2010) and the Moho depth (modified after Mousavi and Ebbing, 2018). **b)** Schematic structure of the North Sistan belt. **c)** Location of the main targets of this study.

Figure 3. Review of the main information available for the Sistan Orogen: synthetic logs modified from Tirrul et al. (1983), metamorphic landmarks from Bonnet et al. (2018; Amph: Amphibolitic facies; BS: blueschist facies; GS: greenschist facies), magmatic landmarks from Jentzer et al. (2020), tectonic landmarks from Jentzer et al. (2017), paleomagnetic from Mattei et al. (2005; CCW: counterclockwise rotation) and the geodynamic evolution inferred from these previous studies. Data provide in this study and their integration in the geodynamic evolution of the Sistan orogeny are also mentioned.

Figure 4. Structural map of the North Sistan belt. **a)** locations of the anchor points (in black) and metamorphic rocks sampled. **b)** representative structural measurement and position of cross-sections.

Figure 5. Representative sedimentary rocks **a-k)** of the Sefidabeh basin; l-r) of the Neh complex (GPS coordinates in supplementary material 1-logs).

Figure 6. RSCM results with Tmax obtained localized on the structural map (see details in supplementary material 2)

Figure 7. Overall structure of Birjand ophiolitic ridge. **a)** Location of Birjand ridge ophiolite and our anchor points; **b-d)** Representative tectonic contact; **e)** Structural map of Birjand ophiolite ridge; **f-j)** Lithologies of representative outcrops (located on a). GPS coordinates of each photography available in supplementary material 1-ophiolite.

Figure 8. Representative lithologies of each Birjand ophiolite unit. **a-f**) Unit 1; **g-h**) Unit 2; **i-k**) Unit 3. GPS coordinates of each photography available in supplementary material 1-ophiolite.

Figure 9. Representative thin section photomicrographs of the ophiolite lithologies. Abbreviations are from Whitney and Evans (2010).

Figure 10. Representative outcrops and landscapes of the Sistan. GPS coordinates of each photography available in supplementary material 1-cross-sections.

Figure 11. Same scale cross-sections across the Sistan. And: Andalusite; BS: Blueschist facies; E: Eclogitic facies; GS: Greenschist facies; J: Jurassic; C: Cretaceous; LC: Lower Cretaceous; UC: Upper Cretaceous; SB: Sefidabeh basin; WU: Western Unit

Figure 12. Representative thin section and SEM photomicrographs **a-d)** Birjand metasediments; **e-h)** Amphibolitic sole; **i-j)** Metamorphic rocks of the Lut block at the boundary with the Neh complex; **k-n)** Dehsalm metamorphic complex

Figure 13. Compositional plots of minerals. **a)** for the Birjand metasediments; **b)** Amphibolitic sole; **c)** Metamorphic rocks of the Lut block at the boundary with the Neh complex; **d)** Dehsalm metamorphic complex. Representative examples are given in supplementary material 2.

Figure 14. Estimation of the P-T conditions. **a)** On Birjand metasediments using mineral assemblage compared to initiation or mature subduction gradient (Agard et al., 2018, 2020; Bonnet et al., 2019) **b)** On aphibolitic sole using (on top) amphibole-plagioclase thermobarometry and Zr in titanite (grey areas corresponds to P-T conditions observed in metamorphic sole worldwise Agard et al., 2016) or using isopleths on pseudosection for sample 15b-15c (mineral assemblage for the fields 1 to 8 are available on supplementary material 3). **c)** On metasimentary rocks of the Lut Block using garnet-biotite thermometry and mineral assemblage on pseudsection for sample 16-72 (3: WM, Bt, Fsp, Ilm, Sil, Qz, H_2O; 4: Bt, Fsp_1, Fsp_2, Ilm, Sil, Qz, H_2O; all mineral assemblage for the fields 1 to 10 are available on supplementary material 3). **d)** On Deh-Salm complex metasedimentry rocks using Ti-in biotite for thermometry, garnet-biotite-aluminosilicate-quartz for thermobarometry and both mineral assemblage and composition on pseudosection for sample 14-29 (7: Grt, Melt, WM, Bt, Fsp, Ky, Qz, Rt, H_2O; 8: Grt, WM, Bt, Fsp, Ky, Qz, Rt, H_2O; 9: Grt, WM, St, Bt, Fsp, Ky, Qz, Rt, H_2O; 33: Grt, Melt, WM, Bt, Fsp, Sil, Qz, Rt, H_2O; 34: Grt, Melt, WM, Bt, Fsp, Sil, Qz, Rt; 35: Grt, Melt, Bt, Fsp, Sil, Qz, Rt; 36: Grt, Melt, Bt, Fsp, Ilm, Sil, Qz, Rt, H_2O; 37: Grt, Melt, WM, Bt, Fsp, Ilm, Sil, Qz, Rt, H_2O; 38: Grt, Melt, WM, Bt, Fsp, Ilm, Sil, Qz, H_2O; 39: Grt, WM, St, Bt, Fsp, Ilm, Sil, Qz, H_2O; 40: WM, Bt, Fsp, Ilm, Sil, Qz, H_2O; all mineral assemblage for the fields 1 to 44 are available on supplementary material 3). The shade of grey on the speudosection indicate the field variance.

Figure 15. Synthesis of the geochronological work, including Tera-Wasserburg diagrams showing U-Pb analytical data of titanite with error ellipses of the 95% confidence interval or ^{40}Ar-^{39}Ar age degassing spectra for amphibole, biotite or white mica. **a)** for ophiolitic gabbro;

b-c) for Birjand metachert; **d-k)** for Neh amphibolitic sole; **l)** for granitoid intrusion; **m)** for Dehsalm metamorphic complex migmatite.

Figure 16. Synthetic cross-section of the Sistan orogen. And: Andalusite; BS: Blueschist facies; Cong.: Conglomerate; E: Eclogitic facies; Eo: Eocene; GS: greenschist facies; J: Jurassic; C or Cret.: Cretaceous; LC: Lower Cretaceous; UC: Upper Cretaceous; Ng: Neogen; Pe: Paleocen; SB: Sefidabeh basin; WU: Western Unit.

Figure 17. Major metamorphic events associated with the Sistan orogeny. **a)** Results provided by this study ; **b)** Comparison between the HP-BT Ratuk complex metamorphism (Fotoohi Rad et al., 2009, 2005; Angiboust et al., 2013; Bonnet et al., 2018;) and the green-schist to amphibolite metamorphism of the Neh complexe.

Figure 18. Tectonic reconstruction along NNE-SSW profile (located on Figs. 4) of the Sistan from Turonian to present day.

Figure 19. 3D block diagram emphasizing the initiation of intra-oceanic subduction between 74 and 72 Ma.

Figure 20. Tectonic evolution of the Sistan in the Tethyan real from Late Jurassic to Eocene. BD: Bajgan-Durkan; K: Kandahar; TeH: Torbat-e-Heydarieh; SaSi: Sanandaj-Sirjan.

Table 1. Petrology and mineralogy of the main metamorphic lithologies studied

Table 2. Comparison between the main inner ophiolite of Iran

Supplementary material 1: GPS coordinates of the studied outcrops

Supplementary material 2: Raman results and representative microprobe analyses for minerals of each metamorphic rocks type.

Supplementary material 3: Bulk composition and mineral assemblage for each pseudosections.

References

Agard, P., Monié, P., Gerber, W., Omrani, J., Molinaro, M., Meyer, B., Labrousse, L., Vrielynck, B., Jolivet, L., Yamato, P., 2006. Transient, synobduction exhumation of Zagros blueschists inferred from P-T, deformation, time, and kinematic constraints: Implications for Neotethyan wedge dynamics: TRANSIENT EXHUMATION PROCESSES IN ZAGROS. Journal of Geophysical Research: Solid Earth 111, n/a-n/a. https://doi.org/10.1029/2005JB004103

Agard, P., Omrani, J., Jolivet, L., Whitechurch, H., Vrielynck, B., Spakman, W., Monié, P., Meyer, B., Wortel, R., 2011. Zagros orogeny: a subduction-dominated process. Geological Magazine 148, 692–725. https://doi.org/10.1017/S001675681100046X

Agard, P., Yamato, P., Soret, M., Prigent, C., Guillot, S., Plunder, A., Dubacq, B., Chauvet, A., Monié, P., 2016. Plate interface rheological switches during subduction infancy: Control on slab penetration and metamorphic sole formation. Earth and Planetary Science Letters 451, 208–220. https://doi.org/10.1016/j.epsl.2016.06.054

Ajirlu, M.S., Moazzen, M., Hajialioghli, R., 2016. Tectonic evolution of the Zagros Orogen in the realm of the Neotethys between the Central Iran and Arabian Plates: An ophiolite perspective. Central European Geology 59, 1–27. https://doi.org/10.1556/24.59.2016.001

Aleinikoff, J.N., Wintsch, R.P., Tollo, R.P., Unruh, D.M., Fanning, C.M., Schmitz, M.D., 2007. Ages and origins of rocks of the Killingworth dome, south-central Connecticut: Implications for the tectonic evolution of southern New England. American Journal of Science 307, 63–118. https://doi.org/10.2475/01.2007.04

Angiboust, S., Agard, P., De Hoog, J.C.M., Omrani, J., Plunder, A., 2013a. Insights on deep, accretionary subduction processes from the Sistan ophiolitic “mélange” (Eastern Iran). Lithos 156–159, 139–158. https://doi.org/10.1016/j.lithos.2012.11.007

Angiboust, S., Agard, P., De Hoog, J.C.M., Omrani, J., Plunder, A., 2013b. Insights on deep, accretionary subduction processes from the Sistan ophiolitic "mélange" (Eastern Iran). Lithos 156–159, 139–158. https://doi.org/10.1016/j.lithos.2012.11.007

Azizi, H., Stern, R.J., 2019. Jurassic igneous rocks of the central Sanandaj–Sirjan zone (Iran) mark a propagating continental rift, not a magmatic arc. Terra Nova 31, 415–423. https://doi.org/10.1111/ter.12404

Babazadeh, S.A., De Wever, P., 2004. Early Cretaceous radiolarian assemblages from radiolarites in the Sistan Suture (eastern Iran). Geodiversitas 26, 185–206.

Bagheri, S., Damani Gol, S., 2020. The eastern iranian orocline. Earth-Science Reviews 210, 103322. https://doi.org/10.1016/j.earscirev.2020.103322

Barrier, E., Vrielynck, B., Brouillet, J.-F., Brunet, M.-F., 2018. Paleotetconic reconstruction of the Central Tethyan realm. Atlas of 20 maps.

Berberian, F., Berberian, M., 1981. Tectono-plutonic episodes in Iran. Zagros Hindu Kush Himalaya Geodynamic Evolution 5–32.

Berberian, M., Jackson, J.A., Qorashi, M., Talebian, M., Khatib, M., Priestley, K., 2000. The 1994 Sefidabeh earthquakes in eastern Iran: blind thrusting and bedding-plane slip on a growing anticline, and active tectonics of the Sistan suture zone. Geophysical Journal International 142, 283–299.

Berberian, M., King, G.C.P., 1981. Towards a paleogeography and tectonic evolution of Iran. Canadian Journal of Earth Sciences 18, 210–265. https://doi.org/10.1139/e81-019

Besse, J., Torcq, F., Gallet, Y., Ricou, L.E., Krystyn, L., Saidi, A., 1998. Late Permian to Late Triassic palaeomagnetic data from Iran: constraints on the migration of the Iranian block through the Tethyan Ocean and initial destruction of Pangaea. Geophysical Journal International 135, 77–92. https://doi.org/10.1046/j.1365-246X.1998.00603.x

Beyssac, O., Goffé, B., Chopin, C., Rouzaud, J.N., 2002. Raman spectra of carbonaceous material in metasediments: a new geothermometer: RAMAN SPECTROSCOPY OF CARBONACEOUS MATERIAL. Journal of Metamorphic Geology 20, 859–871. https://doi.org/10.1046/j.1525-1314.2002.00408.x

Bonnet, G., Agard, P., Angiboust, S., Monié, P., Jentzer, M., Omrani, J., Whitechurch, H., Fournier, M., 2018. Tectonic slicing and mixing processes along the subduction interface: The Sistan example (Eastern Iran). Lithos 310–311, 269–287. https://doi.org/10.1016/j.lithos.2018.04.016

Bonnet, G., Agard, P., Whitechurch, H., Fournier, M., Angiboust, S., Caron, B., Omrani, J., 2020. Fossil seamount in southeast Zagros records intraoceanic arc to back-arc transition: New constraints for the evolution of the Neotethys. Gondwana Research 81, 423–444. https://doi.org/10.1016/j.gr.2019.10.019

Boulin, J., 1991. Structures in Southwest Asia and evolution of the eastern Tethys. Tectonophysics 196, 211–268.

Bröcker, M., Fotoohi Rad, G., Abbaslu, F., Rodionov, N., 2014. Geochronology of high-grade metamorphic rocks from the Anjul area, Lut block, eastern Iran. Journal of Asian Earth Sciences 82, 151–162. https://doi.org/10.1016/j.jseaes.2013.12.021

Bröcker, M., Fotoohi Rad, G., Burgess, R., Theunissen, S., Paderin, I., Rodionov, N., Salimi, Z., 2013. New age constraints for the geodynamic evolution of the Sistan Suture Zone, eastern Iran. Lithos 170–171, 17–34. https://doi.org/10.1016/j.lithos.2013.02.012

Brunet, M.-F., Korotaev, M.V., Ershov, A.V., Nikishin, A.M., 2003. The South Caspian Basin: a review of its evolution from subsidence modelling. Sedimentary Geology 156, 119–148. https://doi.org/10.1016/S0037-0738(02)00285-3

Burg, J.-P., 2018. Geology of the onshore Makran accretionary wedge: Synthesis and tectonic interpretation. Earth-Science Reviews 185, 1210–1231. https://doi.org/10.1016/j.earscirev.2018.09.011

Camp, V.E., Griffis, R.J., 1982a. Character, genesis and tectonic setting of igneous rocks in the Sistan suture zone, eastern Iran. Lithos 15, 221–239.

Camp, V.E., Griffis, R.J., 1982b. Character, genesis and tectonic setting of igneous rocks in the Sistan suture zone, eastern Iran. Lithos 15, 221–239.

Cannat, M., Sauter, D., Escartin, J., Lavier, L., Picazo, S., 2009. Oceanic corrugated surfaces and the strength of the axial lithosphere at slow spreading ridges. Earth and Planetary Science Letters 288, 174–183. https://doi.org/10.1016/j.epsl.2009.09.020

Connolly, J.A.D., 2005. Computation of phase equilibria by linear programming: A tool for geodynamic modeling and its application to subduction zone decarbonation. Earth and Planetary Science Letters 236, 524–541. https://doi.org/10.1016/j.epsl.2005.04.033

Connolly, J.A.D., 1990. Multivariable phase diagrams: an algorithm based on generalized thermodynamics. American Journal of Science 290, 666–718.

Corfield, R.I., Searle, M.P., Pedersen, R.B., 2001. Tectonic Setting, Origin, and Obduction History of the Spontang Ophiolite, Ladakh Himalaya, NW India. The Journal of Geology 109, 715–736. https://doi.org/10.1086/323191

Davies, J.H., 2013. Global map of solid Earth surface heat flow: Global Surface Heat Flow Map. Geochemistry, Geophysics, Geosystems 14, 4608–4622. https://doi.org/10.1002/ggge.20271

Davoudzadeh, M., Soffel, H., Schmidt, K., 1981. On the rotation of the Central-East-Iran microplate. Neues Jahrbuch für Geologie und Paläontologie - Abhandlungen 180–192.

Delaloye, M., Desmons, J., 1980. Ophiolites and mélange terranes in Iran: a geochronological study and its paleotectonic implications. Tectonophysics 68, 83–111.

Delavari, M., Amini, S., Saccani, E., Beccaluva, L., 2009. Geochemistry and Petrologenesis of Mantle Peridotites from the Nehbandan Ophiolitic Complex, Eastern Iran. Journal of Applied Sciences 9, 2671–2687.

DeMets, C., Gordon, R.G., Argus, D.F., 2010. Geologically current plate motions. Geophysical Journal International 181, 1–80. https://doi.org/10.1111/j.1365-246X.2009.04491.x

Dercourt, J. et al, Zonenshain, L.P., Ricou, L.-E., Kazmin, V.G., Le Pichon, X., Knipper, A.L., Grandjacquet, C., Sbortshikov, I.M., Geyssant, J., Lepvrier, C., others, 1986. Geological evolution of the Tethys belt from the Atlantic to the Pamirs since the Lias. Tectonophysics 123, 241–315.

Dubacq, B., Soret, M., Jewison, E., Agard, P., 2019. Early subduction dynamics recorded by the metamorphic sole of the Mt. Albert ophiolitic complex (Gaspé, Quebec). Lithos 334–335, 161–179. https://doi.org/10.1016/j.lithos.2019.03.019

Eddy, M.P., Jagoutz, O., Ibañez-Mejia, M., 2017. Timing of initial seafloor spreading in the Newfoundland-Iberia rift. Geology 45, 527–530. https://doi.org/10.1130/G38766.1

Eftekhar Nezhad, J., Ohanian, T., Tatevosian, S., Afaghi, A., Hosseini, Z., Ghomashi, A., Afharian Zadeh, A., Etemadi, N., 1987. Birjand Geological map.

Ernst, W.G., Liu, J., 1998. Experimental phase-equilibrium study of Al- and Ti-contents of calcic amphibole in MORB; a semiquantitative thermobarometer. American Mineralogist 83, 952–969. https://doi.org/10.2138/am-1998-9-1004

Escartín, J., Mével, C., Petersen, S., Bonnemains, D., Cannat, M., Andreani, M., Augustin, N., Bezos, A., Chavagnac, V., Choi, Y., Godard, M., Haaga, K., Hamelin, C., Ildefonse, B., Jamieson, J., John, B., Leleu, T., MacLeod, C.J., Massot-Campos, M., Nomikou, P., Olive, J.A., Paquet, M., Rommevaux, C., Rothenbeck, M., Steinfuhrer, A., Tominaga, M., Triebe, L., Campos, R., Gracias, N., Garcia, R., 2017. Tectonic structure, evolution, and the nature of oceanic core complexes and their detachment fault zones (13°20′N and 13°30′N, Mid Atlantic

Ridge): 13°N MAR CORRUGATED OCEANIC DETACHMENTS. Geochemistry, Geophysics, Geosystems 18, 1451–1482. https://doi.org/10.1002/2016GC006775

Eshagh, Mehdi, Tenzer, R., Eshagh, Mehrdad, 2019. Elastic thickness of the Iranian lithosphere from gravity and seismic data. Tectonophysics 228186. https://doi.org/10.1016/j.tecto.2019.228186

Esmaeily, D., Nédélec, A., Valizadeh, M.V., Moore, F., Cotten, J., 2005. Petrology of the Jurassic Shah-Kuh granite (eastern Iran), with reference to tin mineralization. Journal of Asian Earth Sciences 25, 961–980. https://doi.org/10.1016/j.jseaes.2004.09.003

Festa, A., Pini, G.A., Ogata, K., Dilek, Y., 2019. Diagnostic features and field-criteria in recognition of tectonic, sedimentary and diapiric mélanges in orogenic belts and exhumed subduction-accretion complexes. Gondwana Research. https://doi.org/10.1016/j.gr.2019.01.003

Fotoohi Rad, G.R., Droop, G.T.R., Amini, S., Moazzen, M., 2005. Eclogites and blueschists of the Sistan Suture Zone, eastern Iran: A comparison of P–T histories from a subduction mélange. Lithos 84, 1–24. https://doi.org/10.1016/j.lithos.2005.01.007

Fotoohi Rad, G.R., Droop, G.T.R., Burgess, R., 2009. Early Cretaceous exhumation of high-pressure metamorphic rocks of the Sistan Suture Zone, eastern Iran. Geological Journal 44, 104–116. https://doi.org/10.1002/gj.1135

Gaina, C., van Hinsbergen, D.J.J., Spakman, W., 2015. Tectonic interactions between India and Arabia since the Jurassic reconstructed from marine geophysics, ophiolite geology, and seismic tomography: INDIA-ARABIA TECTONIC INTERACTIONS. Tectonics 34, 875–906. https://doi.org/10.1002/2014TC003780

Gnos, E., Immenhauser, A., Peters, Tj., 1997. Late Cretaceous/early Tertiary convergence between the Indian and Arabian plates recorded in ophiolites and related sediments. Tectonophysics 271, 1–19. https://doi.org/10.1016/S0040-1951(96)00249-1

Green, E.C.R., White, R.W., Diener, J.F.A., Powell, R., Holland, T.J.B., Palin, R.M., 2016. Activity-composition relations for the calculation of partial melting equilibria in metabasic rocks. Journal of Metamorphic Geology 34, 845–869. https://doi.org/10.1111/jmg.12211

Guilmette, C., Smit, M.A., van Hinsbergen, D.J.J., Gürer, D., Corfu, F., Charette, B., Maffione, M., Rabeau, O., Savard, D., 2018. Forced subduction initiation recorded in the sole and crust of the Semail Ophiolite of Oman. Nature Geoscience 11, 688–695. https://doi.org/10.1038/s41561-018-0209-2

Hayden, L.A., Watson, E.B., Wark, D.A., 2008. A thermobarometer for sphene (titanite). Contributions to Mineralogy and Petrology 155, 529–540. https://doi.org/10.1007/s00410-007-0256-y

Henry, D.J., 2005. The Ti-saturation surface for low-to-medium pressure metapelitic biotites: Implications for geothermometry and Ti-substitution mechanisms. American Mineralogist 90, 316–328. https://doi.org/10.2138/am.2005.1498

Holdaway, M.J., 2000. Application of new experimental and garnet Margules data to the garnet-biotite geothermometer. American Mineralogist 85, 881–892. https://doi.org/10.2138/am-2000-0701

Holland, T., Blundy, J., 1994. Non-ideal interactions in calcic amphiboles and their bearing on amphibole-plagioclase thermometry. Contributions to mineralogy and petrology 116, 433–447.

Holland, T., Powell, R., 2003. Activity composition relations for phases in petrological calculations: an asymmetric multicomponent formulation. Contributions to Mineralogy and Petrology 145, 492–501. https://doi.org/10.1007/s00410-003-0464-z

Holland, T.J.B., Powell, R., 2011. An improved and extended internally consistent thermodynamic dataset for phases of petrological interest, involving a new equation of state for solids: THERMODYNAMIC DATASET FOR PHASES OF PETROLOGICAL INTEREST.

Journal of Metamorphic Geology 29, 333–383. https://doi.org/10.1111/j.1525-1314.2010.00923.x

Hunziker, D., Burg, J.-P., Bouilhol, P., von Quadt, A., 2015. Jurassic rifting at the Eurasian Tethys margin: Geochemical and geochronological constraints from granitoids of North Makran, southeastern Iran. Tectonics 34, 571–593. https://doi.org/10.1002/2014TC003768

Jentzer, M., Fournier, M., Agard, P., Omrani, J., Khatib, M.M., Whitechurch, H., 2017. Neogene to Present paleostress field in Eastern Iran (Sistan belt) and implications for regional geodynamics: Paleostress Field in Eastern Iran. Tectonics 36, 321–339. https://doi.org/10.1002/2016TC004275

Jentzer, M., Whitechurch, H., Agard, P., Ulrich, M., Caron, B., Zarrinkoub, M.H., Kohansal, R., Miguet, L., Omrani, J., Fournier, M., 2020. Late Cretaceous calc-alkaline and adakitic magmatism in the Sistan suture zone (Eastern Iran): Implications for subduction polarity and regional tectonics. Journal of Asian Earth Sciences 104588. https://doi.org/10.1016/j.jseaes.2020.104588

Jourdan, F., Renne, P.R., 2007. Age calibration of the Fish Canyon sanidine 40Ar/39Ar dating standard using primary K–Ar standards. Geochimica et Cosmochimica Acta 71, 387–402. https://doi.org/10.1016/j.gca.2006.09.002

Kontoyannis, C.G., Vagenas, N.V., 2000. Calcium carbonate phase analysis using XRD and FT-Raman spectroscopy. The Analyst 125, 251–255. https://doi.org/10.1039/a908609i

Kouketsu, Y., Mizukami, T., Mori, H., Endo, S., Aoya, M., Hara, H., Nakamura, D., Wallis, S., 2014. A new approach to develop the Raman carbonaceous material geothermometer for low-grade metamorphism using peak width: Raman CM geothermometer using FWHM. Island Arc 23, 33–50. https://doi.org/10.1111/iar.12057

Kurzawa, T., Bröcker, M., Fotoohi Rad, G., Berndt, J., Lisker, F., 2017. Cretaceous high-pressure metamorphism and low pressure overprint in the Sistan Suture Zone, eastern Iran:

Additional temperature estimates for eclogites, geological significance of U-Pb zircon ages and Rb-Sr constraints on the timing of exhumation. Journal of Asian Earth Sciences 147, 332–344. https://doi.org/10.1016/j.jseaes.2017.07.051

Kylander-Clark, A.R.C., Hacker, B.R., Cottle, J.M., 2013. Laser-ablation split-stream ICP petrochronology. Chemical Geology 345, 99–112. https://doi.org/10.1016/j.chemgeo.2013.02.019

Lagabrielle, Y., Vitale Brovarone, A., Ildefonse, B., 2015. Fossil oceanic core complexes recognized in the blueschist metaophiolites of Western Alps and Corsica. Earth-Science Reviews 141, 1–26. https://doi.org/10.1016/j.earscirev.2014.11.004

Lahfid, A., Beyssac, O., Deville, E., Negro, F., Chopin, C., Goffé, B., 2010. Evolution of the Raman spectrum of carbonaceous material in low-grade metasediments of the Glarus Alps (Switzerland): RSCM in low-grade metasediments. Terra Nova 22, 354–360. https://doi.org/10.1111/j.1365-3121.2010.00956.x

Lanphere, M.A., Pamic, J., 1983. 40Ar/39Ar ages and tectonic setting of ophiolite from the Neyriz area, southeast Zagros range, Iran. Tectonophysics 245–256.

Leroy, S., Mauffret, A., Patriat, P., Mercier de Lepinay, B., 2000. An alternative interpretation of the Cayman trough evolution from a reidentification of magnetic anomalies. Geophysical Journal International 141, 539–557. https://doi.org/10.1046/j.1365-246x.2000.00059.x

Lucazeau, F., 2019. Analysis and mapping of an updated terrestrial heat flow dataset. Geochemistry, Geophysics, Geosystems. https://doi.org/10.1029/2019GC008389

Mahmoudi, S., Masoudi, F., Corfu, F., Mehrabi, B., 2010. Magmatic and metamorphic history of the Deh-Salm metamorphic Complex, Eastern Lut block, (Eastern Iran), from U–Pb geochronology. International Journal of Earth Sciences 99, 1153–1165. https://doi.org/10.1007/s00531-009-0465-x

Masoudi, F., Mehrabi, B., Mahmoudi, S., 2006. Garnet (Almandine-Spessartine) Growth Zoning and Its Application to Constrain Metamorphic History in Dehsalm Complex, Iran 17, 11.

Mattei, M., Cifelli, F., Muttoni, G., Zanchi, A., Berra, F., Mossavvari, F., Eshraghi, S.A., 2012. Neogene block rotation in central Iran: Evidence from paleomagnetic data. Geological Society of America Bulletin 14.

Mattei, M., Cifelli, F., Muttoni, G., Rashid, H., 2015. Post-Cimmerian (Jurassic-Cenozoic) paleogeography and vertical axis tectonic rotations of Central Iran and the Alborz Mountains. Journal of Asian Earth Sciences 102, 92–101. https://doi.org/10.1016/j.jseaes.2014.09.038

Maurizot, P., Fauvelet, E., Eftekhar-Nezhad, J., 1990. Explanatory text of the Gazik quadrangle map 1:250,000.

Metcalfe, I., 2013. Gondwana dispersion and Asian accretion: Tectonic and palaeogeographic evolution of eastern Tethys. Journal of Asian Earth Sciences 66, 1–33. https://doi.org/10.1016/j.jseaes.2012.12.020

Moazzen, M., Modjarrad, M., Zarrinkoub, M., 2006. Mineral chemistry, petrogenesis and P-T conditions of formation of harzburgitic peridotites from south of Birjand, Eastern Iran. Journal of Asian Earth Sciences. https://doi.org/10.1016/j.jseaes.2005.07.009

Mohammadi, A., Burg, J.-P., Bouilhol, P., Ruh, J., 2016a. U-Pb geochronology and geochemistry of Zahedan and Shah Kuh plutons, southeast Iran: Implication for closure of the South Sistan suture zone. Lithos 248–251, 293–308. https://doi.org/10.1016/j.lithos.2016.02.003

Mohammadi, A., Burg, J.-P., Winkler, W., Ruh, J., von Quadt, A., 2016b. Detrital zircon and provenance analysis of Late Cretaceous–Miocene onshore Iranian Makran strata: Implications for the tectonic setting. Geological Society of America Bulletin 128, 1481–1499. https://doi.org/10.1130/B31361.1

Montenat, C., 2009. The Mesozoic of Afghanistan. GeoArabia 14, 64.

Mousavi, N., Ebbing, J., 2018. Basement characterization and crustal structure beneath the Arabia–Eurasia collision (Iran): A combined gravity and magnetic study. Tectonophysics 731–732, 155–171. https://doi.org/10.1016/j.tecto.2018.03.018

Omidianfar, S., Monsef, I., Rahgoshay, M., Zheng, J., Cousens, B., 2020. The middle Eocene high-K magmatism in Eastern Iran Magmatic Belt: constraints from U-Pb zircon geochronology and Sr-Nd isotopic ratios. International Geology Review 1–18. https://doi.org/10.1080/00206814.2020.1716272

Omrani, H., 2017. Geodynamic evolution of the Sabzevar zone, northern central Iranian micro-continent. Miner Petrol 19. https://doi.org/10.1007/s00710-017-0505-3

Omrani, J., Agard, P., Whitechurch, H., Benoit, M., Prouteau, G., Jolivet, L., 2008. Arc-magmatism and subduction history beneath the Zagros Mountains, Iran: A new report of adakites and geodynamic consequences. Lithos 106, 380–398. https://doi.org/10.1016/j.lithos.2008.09.008

Ozsvárt, P., Bahramnejad, E., Bagheri, S., Sharifi, M., 2020. New Albian (Cretaceous) radiolarian age constraints for the Dumak ophiolitic mélange from the Shuru area, Eastern Iran. Cretaceous Research 104451. https://doi.org/10.1016/j.cretres.2020.104451

Pang, K.-N., Chung, S.-L., Zarrinkoub, M.H., Khatib, M.M., Mohammadi, S.S., Chiu, H.-Y., Chu, C.-H., Lee, H.-Y., Lo, C.-H., 2013. Eocene–Oligocene post-collisional magmatism in the Lut–Sistan region, eastern Iran: Magma genesis and tectonic implications. Lithos 180–181, 234–251. https://doi.org/10.1016/j.lithos.2013.05.009

Pang, K.-N., Chung, S.-L., Zarrinkoub, M.H., Mohammadi, S.S., Yang, H.-M., Chu, C.-H., Lee, H.-Y., Lo, C.-H., 2012. Age, geochemical characteristics and petrogenesis of Late Cenozoic intraplate alkali basalts in the Lut–Sistan region, eastern Iran. Chemical Geology 306–307, 40–53. https://doi.org/10.1016/j.chemgeo.2012.02.020

Paton, C., Hellstrom, J., Paul, B., Woodhead, J., Hergt, J., 2011. Iolite: Freeware for the visualisation and processing of mass spectrometric data. Journal of Analytical Atomic Spectrometry 26, 2508. https://doi.org/10.1039/c1ja10172b

Pearce, N.J.G., Perkins, W.T., Westgate, J.A., Gorton, M.P., Jackson, S.E., Neal, C.R., Chenery, S.P., 1997. A Compilation of New and Published Major and Trace Element Data for NIST SRM 610 and NIST SRM 612 Glass Reference Materials. Geostandards and Geoanalytical Research 21, 115–144. https://doi.org/10.1111/j.1751-908X.1997.tb00538.x

Picazo, S., Cannat, M., Delacour, A., Escartin, J., Rouméjon, S., Silantyev, S., 2012. Deformation associated with the denudation of mantle-derived rocks at the Mid-Atlantic Ridge 13°-15°N: The role of magmatic injections and hydrothermal alteration: DENUDATION OF ULTRAMAFIC ROCKS. Geochemistry, Geophysics, Geosystems 13. https://doi.org/10.1029/2012GC004121

Pirnia, T., 2020. Cretaceous tectonic evolution of the Neo-Tethys in Central Iran: Evidence from petrology and age of the Nain-Ashin ophiolitic basalts. Geoscience Frontiers 25.

Plunder, A., Agard, P., Chopin, C., Soret, M., Okay, A.I., Whitechurch, H., 2016. Metamorphic sole formation, emplacement and blueschist facies overprint: early subduction dynamics witnessed by western Turkey ophiolites. Terra Nova 28, 329–339. https://doi.org/10.1111/ter.12225

Pouchou, J.-L., Pichoir, F., 1991. Quantitative Analysis of Homogeneous or Stratified Microvolumes Applying the Model “PAP,” in: Electron Probe Quantitation 31–75.

Richards, J.P., Şengör, A.M.C., 2017. Did Paleo-Tethyan anoxia kill arc magma fertility for porphyry copper formation? Geology 45, 591–594. https://doi.org/10.1130/G38954.1

Richards, J.P., Sholeh, A., 2016. Chapter 7 The Tethyan Tectonic History and Cu-Au Metallogeny of Iran 20.

Robert, A.M.M., Letouzey, J., Kavoosi, M.A., Sherkati, S., Müller, C., Vergés, J., Aghababaei, A., 2014. Structural evolution of the Kopeh Dagh fold-and-thrust belt (NE Iran) and interactions with the South Caspian Sea Basin and Amu Darya Basin. Marine and Petroleum Geology 57, 68–87. https://doi.org/10.1016/j.marpetgeo.2014.05.002

Rodriguez, M., Huchon, P., Chamot-Rooke, N., Fournier, M., Delescluse, M., Smit, J., Plunder, A., Calvès, G., Ninkabou, D., Pubellier, M., François, T., Agard, P., Gorini, C., 2020. Successive shifts of the India-Africa transform plate boundary during the Late Cretaceous-Paleogene interval: Implications for ophiolite emplacement along transforms. Journal of Asian Earth Sciences 191, 104225. https://doi.org/10.1016/j.jseaes.2019.104225

Rossetti, F., Nasrabady, M., Theye, T., Gerdes, A., Monié, P., Lucci, F., Vignaroli, G., 2014. Adakite differentiation and emplacement in a subduction channel: The late Paleocene Sabzevar magmatism (NE Iran). Geological Society of America Bulletin 27.

Rossetti, F., Nasrabady, M., Vignaroli, G., Theye, T., Gerdes, A., Razavi, M.H., Vaziri, H.M., 2010. Early Cretaceous migmatitic mafic granulites from the Sabzevar range (NE Iran): implications for the closure of the Mesozoic peri-Tethyan oceans in central Iran. Terra Nova 22, 26–34. https://doi.org/10.1111/j.1365-3121.2009.00912.x

Saccani, E., Delavari, M., Beccaluva, L., Amini, S., 2010. Petrological and geochemical constraints on the origin of the Nehbandan ophiolitic complex (eastern Iran): Implication for the evolution of the Sistan Ocean. Lithos 117, 209–228. https://doi.org/10.1016/j.lithos.2010.02.016

Schmitz, M.D., Bowring, S.A., 2001. U-Pb zircon and titanite systematics of the Fish Canyon Tuff: an assessment of high-precision U-Pb geochronology and its application to young volcanic rocks. Geochimica et Cosmochimica Acta 65, 2571–2587. https://doi.org/10.1016/S0016-7037(01)00616-0

Schmitz, M.D., Schoene, B., 2007. Derivation of isotope ratios, errors, and error correlations for U-Pb geochronology using 205 Pb- 235 U-(233 U)-spiked isotope dilution thermal ionization mass spectrometric data: U-PB ISOTOPE RATIO DERIVATION. Geochemistry, Geophysics, Geosystems 8, n/a-n/a. https://doi.org/10.1029/2006GC001492

Schwartz, S., Guillot, S., Reynard, B., Lafay, R., Debret, B., Nicollet, C., Lanari, P., Auzende, A.L., 2013. Pressure–temperature estimates of the lizardite/antigorite transition in high pressure serpentinites. Lithos 178, 197–210. https://doi.org/10.1016/j.lithos.2012.11.023

Sengor, A.M.C., Altiner, D., Cin, A., Ustaömer, T., Hsü, K.J., 1988. Origin and assembly of the Tethyside orogenic collage at the expense of Gondwana Land. Geological Society, London, Special Publications 37, 119–181. https://doi.org/10.1144/GSL.SP.1988.037.01.09

Sepidbar, F., Frederico, L., Habib, B., Mohamed Zaki, K., Peng, J., 2020. Geochemistry and tectonic significance of the Fannuj-Maskutan SSZ-type ophiolite (Inner Makran, SE Iran). International Geology Review 29. https://doi.org/10.1080/00206814.2020.1753118

Seton, M., Müller, R.D., Zahirovic, S., Gaina, C., Torsvik, T., Shephard, G., Talsma, A., Gurnis, M., Turner, M., Maus, S., Chandler, M., 2012. Global continental and ocean basin reconstructions since 200Ma. Earth-Science Reviews 113, 212–270. https://doi.org/10.1016/j.earscirev.2012.03.002

Siehl, A., 2017. Structural setting and evolution of the Afghan orogenic segment – a review. Geological Society, London, Special Publications 427, 57–88. https://doi.org/10.1144/SP427.8

Soffel, H.C., Davoudzadeh, M., Rolf, C., Schmidt, S., 1996. New palaeomagnetic data from Central Iran and a Triassic palaeoreconstruction. Geologische Rundschau 85, 293–302. https://doi.org/10.1007/s005310050075

Soffel, H.C., Förster, H.G., 1984. Polar Wander Path of the Central-East-Iran Microplate Including New Results. Neues Jahrbuch für Geologie und Paläontologie - Abhandlungen 168, 165–172. https://doi.org/10.1127/njgpa/168/1984/165

Soret, M., Agard, P., Dubacq, B., Plunder, A., Yamato, P., 2017. Petrological evidence for stepwise accretion of metamorphic soles during subduction infancy (Semail ophiolite, Oman and UAE). Journal of Metamorphic Geology. https://doi.org/10.1111/jmg.12267

Spandler, C., Hammerli, J., Sha, P., Hilbert-Wolf, H., Hu, Y., Roberts, E., Schmitz, M., 2016. MKED1: A new titanite standard for in situ analysis of Sm–Nd isotopes and U–Pb geochronology. Chemical Geology 425, 110–126. https://doi.org/10.1016/j.chemgeo.2016.01.002

Spencer, K.J., Hacker, B.R., Kylander-Clark, A.R.C., Andersen, T.B., Cottle, J.M., Stearns, M.A., Poletti, J.E., Seward, G.G.E., 2013. Campaign-style titanite U–Pb dating by laser-ablation ICP: Implications for crustal flow, phase transformations and titanite closure. Chemical Geology 341, 84–101. https://doi.org/10.1016/j.chemgeo.2012.11.012

Stampfli, G.M., Borel, G.D., 2002. A plate tectonic model for the Paleozoic and Mesozoic constrained by dynamic plate boundaries and restored synthetic oceanic isochrons. Earth and Planetary Science Letters 196, 17–33. https://doi.org/10.1016/S0012-821X(01)00588-X

Stöcklin, J., 1974. Possible ancient continental margins in Iran. The Geology of continental Margins 873–887.

Tirrul, R., Bell, I.R., Griffis, R.J., Camp, V.E., 1983. The Sistan suture zone of eastern Iran. Geological Society of America Bulletin 94, 134–150.

Verdel, C., Wernicke, B.P., Hassanzadeh, J., Guest, B., 2011. A Paleogene extensional arc flare-up in Iran: iranian volcanism. Tectonics 30, n/a-n/a. https://doi.org/10.1029/2010TC002809

Vermeesch, P., 2018. IsoplotR: A free and open toolbox for geochronology. Geoscience Frontiers 9, 1479–1493. https://doi.org/10.1016/j.gsf.2018.04.001

Wakabayashi, J., Dilek, Y., 2003. What constitutes ‘emplacement’ of an ophiolite?: Mechanisms and relationship to subduction initiation and formation of metamorphic soles.

Geological Society, London, Special Publications 218, 427–447. https://doi.org/10.1144/GSL.SP.2003.218.01.22

Walker, R.T., Gans, P., Allen, M.B., Jackson, J., Khatib, M., Marsh, N., Zarrinkoub, M., 2009. Late Cenozoic volcanism and rates of active faulting in eastern Iran. Geophysical Journal International 177, 783–805. https://doi.org/10.1111/j.1365-246X.2008.04024.x

Walker, R.T., Khatib, M.M., 2006. Active faulting in the Birjand region of NE Iran: active faulting at Birjand in NE Iran. Tectonics 25, n/a-n/a. https://doi.org/10.1029/2005TC001871

White, R.W., Powell, R., Clarke, G.L., 2002. The interpretation of reaction textures in Fe-rich metapelitic granulites of the Musgrave Block, central Australia: constraints from mineral equilibria calculations in the system K2O-FeO-MgO-Al2O3-SiO2-H2O-TiO2-Fe2O3: REACTION TEXTURES, MUSGRAVE BLOCK GRANULITES. Journal of Metamorphic Geology 20, 41–55. https://doi.org/10.1046/j.0263-4929.2001.00349.x

White, R.W., Powell, R., Holland, T.J.B., Johnson, T.E., Green, E.C.R., 2014. New mineral activity-composition relations for thermodynamic calculations in metapelitic systems. Journal of Metamorphic Geology 32, 261–286. https://doi.org/10.1111/jmg.12071

Zarrinkoub, M. H., Pang, K.-N., Chung, S.-L., Khatib, M.M., Mohammadi, S.S., Chiu, H.-Y., Lee, H.-Y., 2012a. Zircon U-Pb age and geochemical constraints on the origin of the Birjand ophiolite, Sistan suture zone, eastern Iran. Lithos 154, 392–405. https://doi.org/10.1016/j.lithos.2012.08.007

Zarrinkoub, M. H., Mohammadi, S.S., Khatib, M.H., 2012b. Evaluation of adakites in the northern part of Sistan suture zone, eastern Iran, for porphyry mineralization. Recent Researches in Environmental and Geological Sciences 4.

March 10, 2021

Professor M. Santosh
Editor-In-chief
Gondwana Research

Dear Editor,

Please find enclosed a manuscript entitled:
"The Sistan orogen (Eastern Iran): Tectonic evolution and significance within the Tethyan realm"
by Michael Jentzer, Philippe Agard, Guillaume Bonnet, Patrick Monié, Marc Fournier, Hubert Whitechurch, Jafar Omrani, Mohammad Hossein Zarrinkoub, Mohammad Mahdi Khatib, Reza Kohansal, Damien Do Couto, Camille Godbillot and Dia Ninkabou that we wish to submit for publication to Gondwana Research.

We were invited some time ago by Timothy Horscroft to submit this work to your journal (potentially tagged as a GR Focus Review).

Gondwana Research seems indeed particularly well suited for our ms: this work provides a fully original, comprehensive petrological and tectonic study of the Sistan orogen, i.e. the belt formed as a result of the convergence between two Gondwana-derived Cimmerian Blocks, namely the Lut block and the Afghan block.

Results allow to reappraise the geodynamic evolution of the entire region and of the Neo-Tethyan realm. We therefore feel that this ms might be of interest to the broad readership of Gondwana Research, as well as to our Iranian colleagues.

Hoping you will find the enclosed manuscript fit for review, and looking forward to hearing from you,

Best regards,

Michael Jentzer

(corresponding author, email: michael.jentzer@upmc.fr)

Graphical Abstract

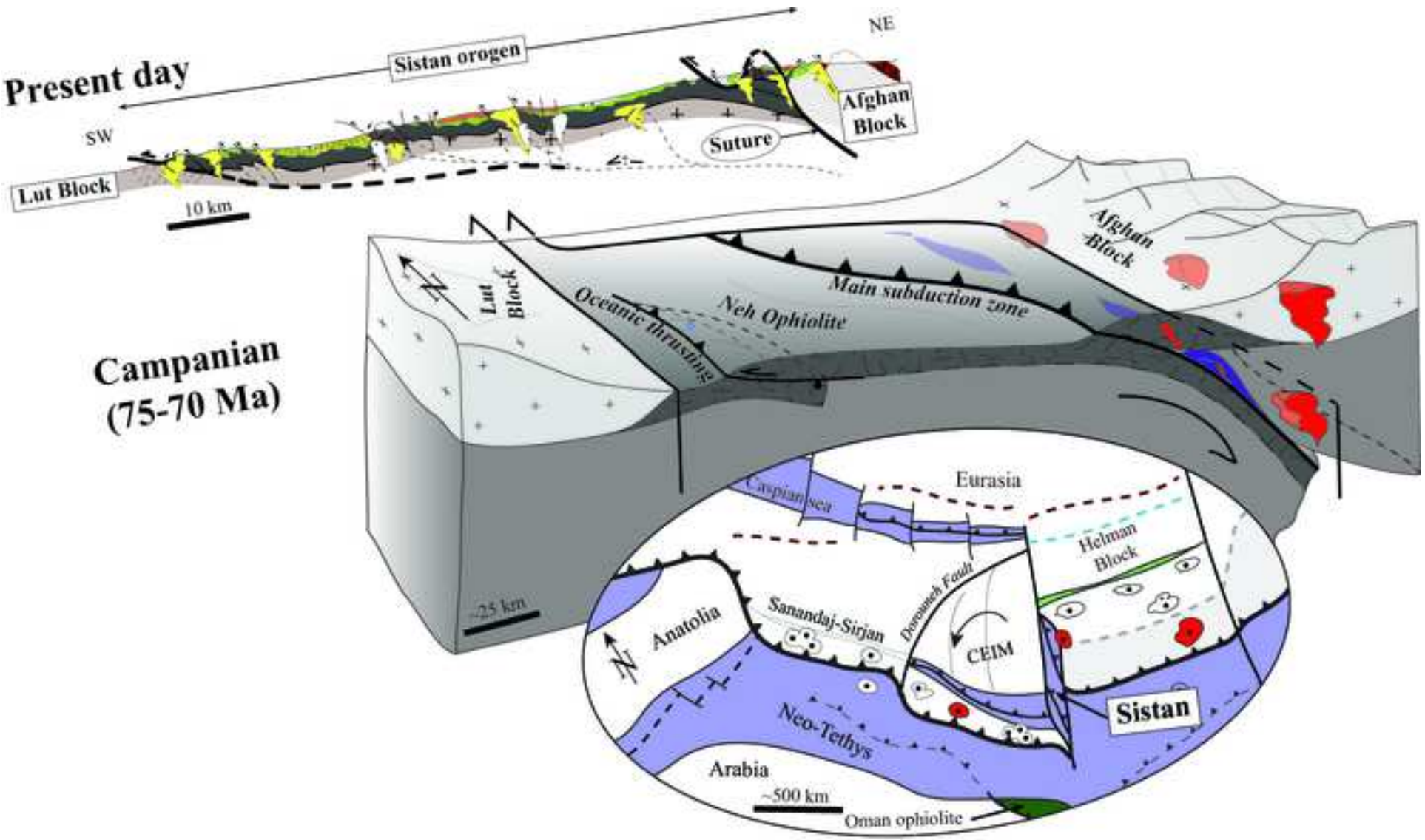

Highlights:

- Sistan ocean opened as a pull apart basin at ~125 Ma with a slow spreading rate.
- Closure of the Sistan started since 90 Ma with a NE-dipping subduction.
- 73 Ma metamorphic sole argues for an oceanic thrusting inducing the obduction process.
- Sistan recorded both ~90 and ~75 Ma geodynamic events affecting the Tethys closure.

Fig 1

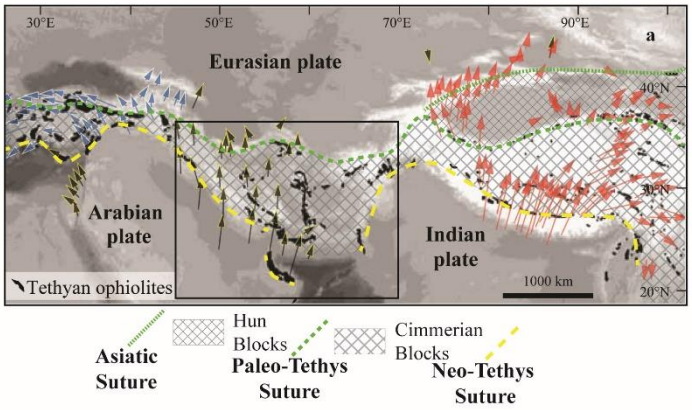

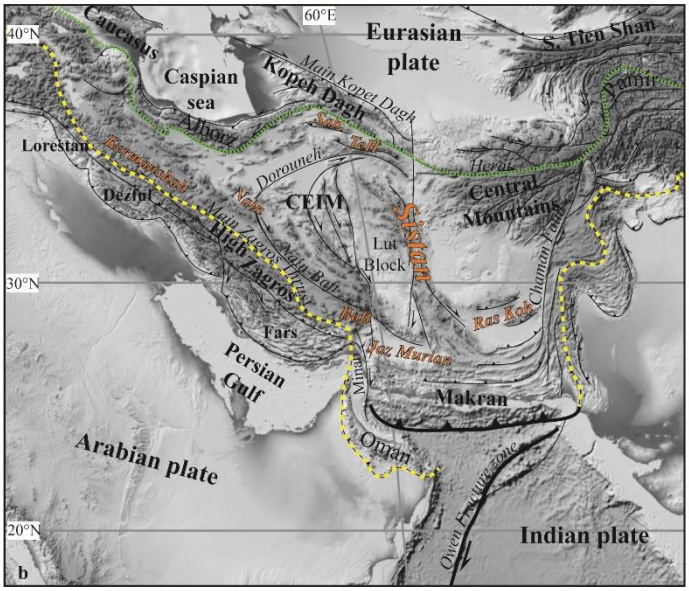

Fig 2

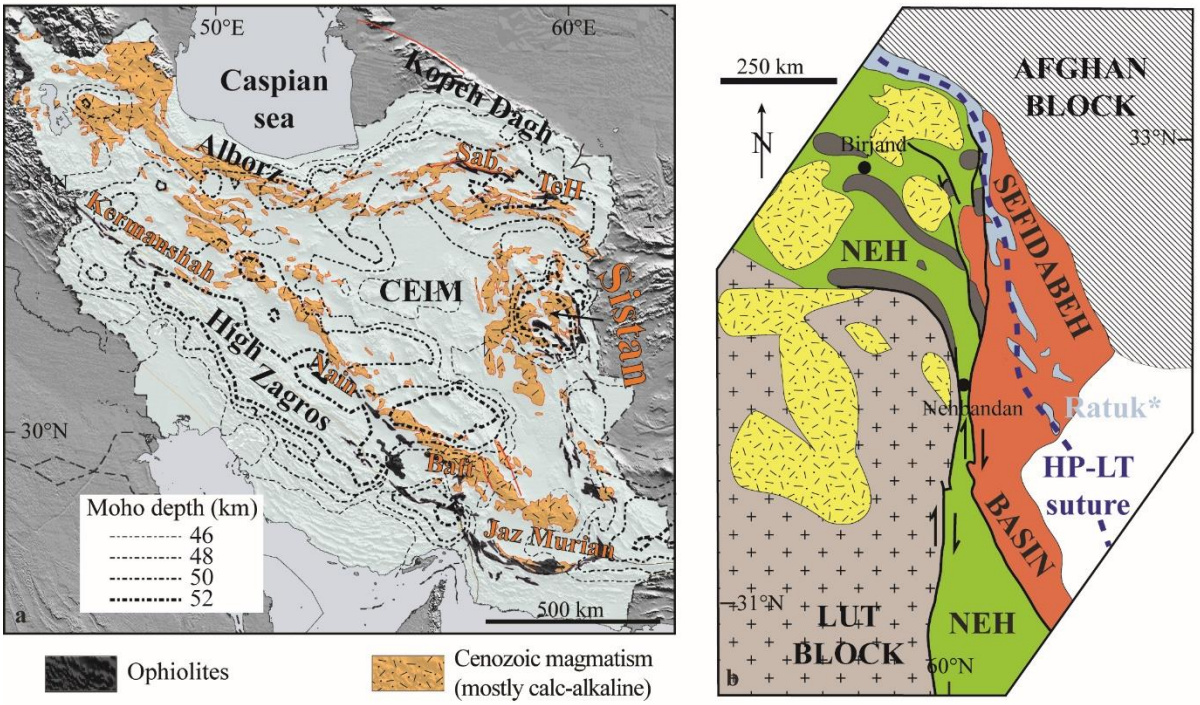
50°E
60°E
Caspian sea
Kopeh Dagh
Alborz
Sab.
Ieh
Kermanshah
CEIM
Sistan
High Zagros
Main
Bajgan
Jaz Murian
30°N
Moho depth (km)
46
48
50
52
500 km
a
Ophiolites
Cenozoic magmatism (mostly calc-alkaline)
250 km
N
AFGHAN BLOCK
33°N
Birjand
SEFIDABEH
NEH
Nehbandan
Ratuk*
HP-LT suture
BASIN
31°N
LUT BLOCK
NEH
60°N
b

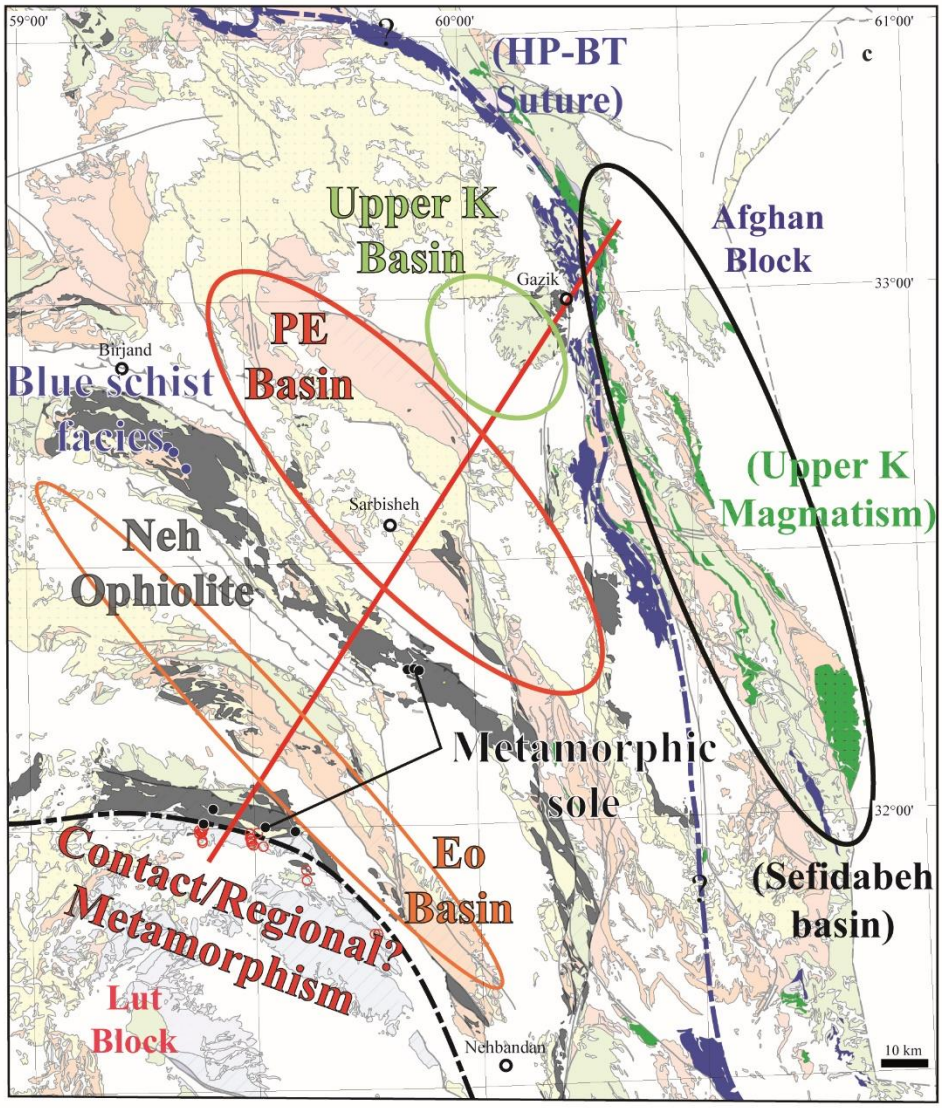
59°00'
60°00'
61°00'
c
(HP-BT Suture)
Upper K Basin
Afghan Block
Gazik
33°00'
PE Basin
Birjand
Blue schist facies
(Upper K Magmatism)
Sarbisheh
Neh Ophiolite
Metamorphic sole
32°00'
Eo Basin
(Sefidabeh basin)
Contact/Regional? Metamorphism
Lut Block
Nehbandan
10 km

Fig. 3

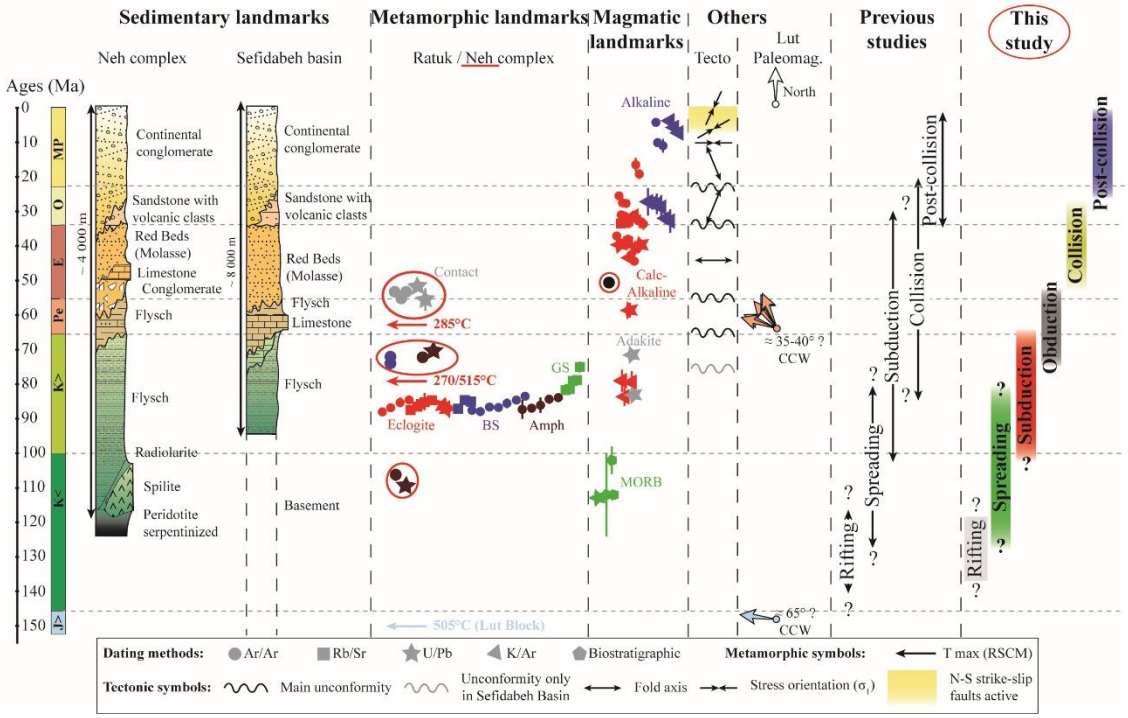
Sedimentary landmarks
Metamorphic landmarks
Magmatic landmarks
Others
Previous studies
This study
Neh complex
Sefidabeh basin
Ratuk / Neh complex
Tecto
Lut Paleomag.
North
Ages (Ma)
MP
O
E
Pe
K>
K<
Δ
~ 4 000 m
~ 8 000 m
Continental conglomerate
Sandstone with volcanic clasts
Red Beds (Molasse)
Limestone Conglomerate
Flysch
Radiolarite
Spilite
Peridotite serpentinized
Limestone
Basement
Contact
285°C
270/515°C
Eclogite
BS
Amph
GS
505°C (Lut Block)
Alkaline
Calc-Alkaline
Adakite
MORB
≈ 35-40° ? CCW
65° ? CCW
Rifting
Spreading
Subduction
Collision
Post-collision
Obduction
Dating methods:
Ar/Ar
Rb/Sr
U/Pb
K/Ar
Biostratigraphic
Metamorphic symbols:
T max (RSCM)
Tectonic symbols:
Main unconformity
Unconformity only in Sefidabeh Basin
Fold axis
Stress orientation (σ1)
N-S strike-slip faults active

Fig. 4

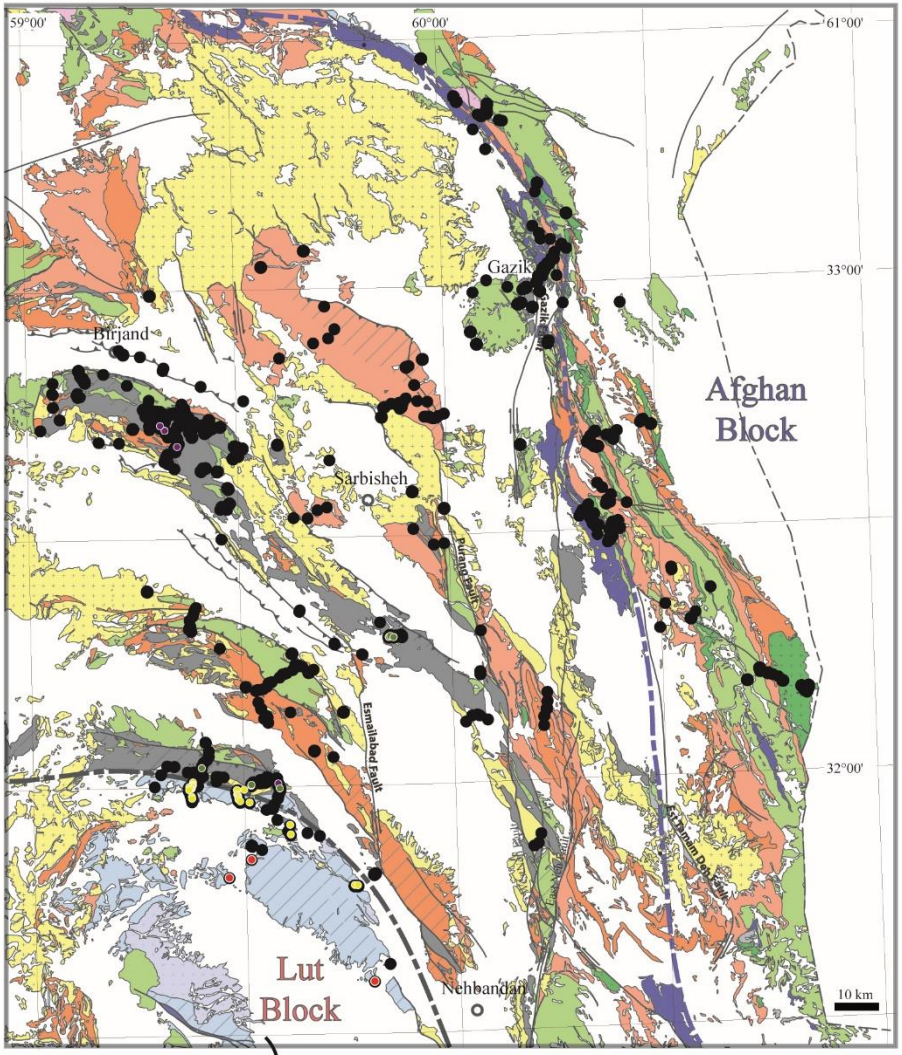

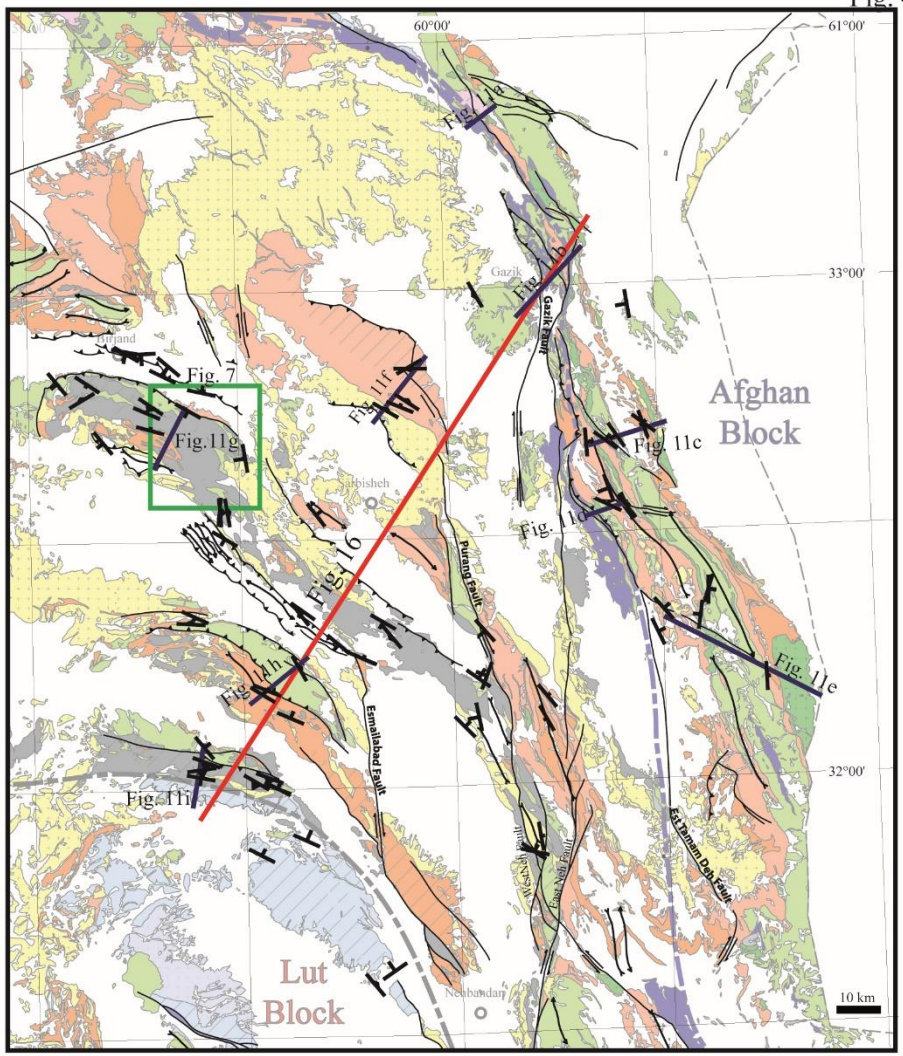

Dehsalm metamorphic complex

Sedimentary rocks Plio-quaternary | Oligo-miocene | Eocene | Paleocene | Cretaceous | Jurassic | Precambrian

Magmatic rocks: Cenozoic (mostly oligocene) | Cretaceous | Jurassic | Precambrian

Metamorphic rocks: Undetermined facies | Eclogite and BS facies **Others:** Ophiolitic complex

Outcrops: Anchor points | Neh: Birjand Metasediments | Neh: Amphibolitic sole | Lut: contact metamorphism | Lut: regional metamorphism

Boundary line | HP-LT Suture zone | Western limit of the Lut block

Tectonic information: Anticline axis | Syncline axis

Main faults | Main stricke-slipe faults | Main reverse faults

Representative strike an dip of the bedding: 0< ⊢ <30 60≤ ⊢ <90; 30≤ ⊢ <60 ⊢ = 90

Representative strike an dip of the schistosity: 30< ⊢ ≤90; 30< ⊢ ≤60; 0< ⊢ ≤30

Representative strike of the lineation: |

Fig. 5


a
Calci-Turbidite
Aptian(?) -Senonian
b
Conglomerate
basal Maastrichtian
c
Turbidite
Maastrichtian
d
Hippuritic limestone
Maastrichtian
e
f
g
h
Reefal limestone
Paleocene
i
Turbidite
Paleocene
j
Red Beds conglomerate
Eocene
k
Conglomerate
Plio-quaternary

Fig. 5-continued

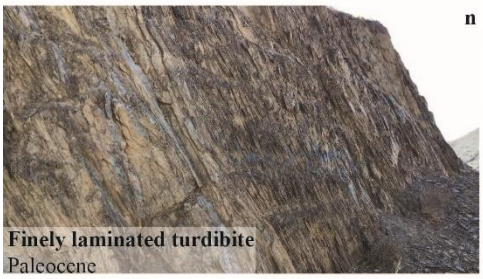

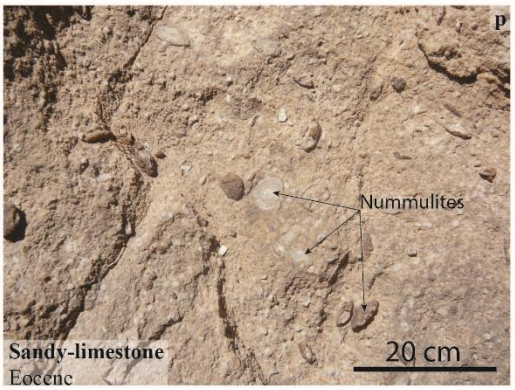

Fig. 6

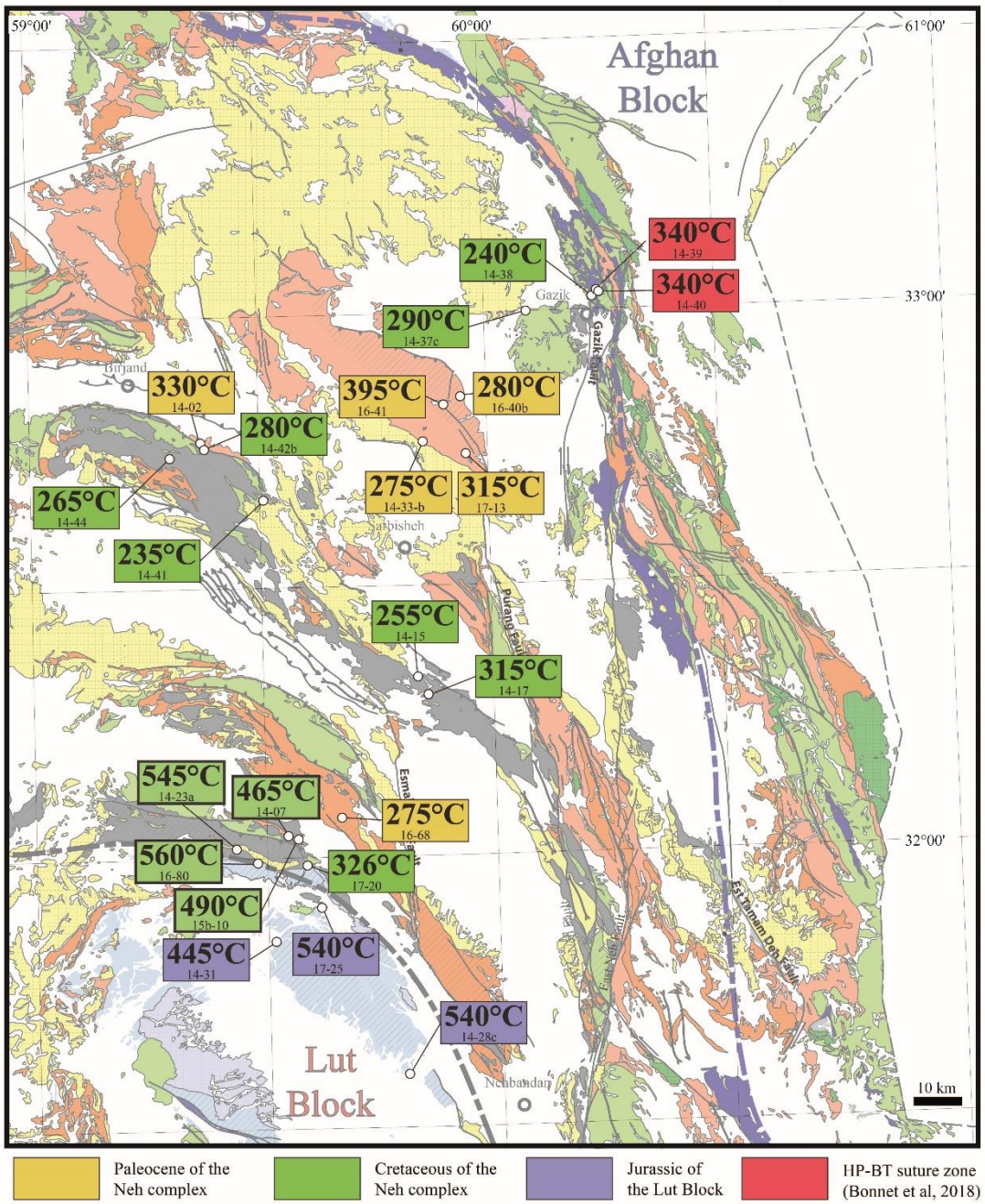
59°00'
60°00'
61°00'
33°00'
32°00'
Afghan Block
Lut Block
340°C 14-39
340°C 14-40
240°C 14-38
290°C 14-37c
330°C 14-02
280°C 14-42b
395°C 16-41
280°C 16-40b
275°C 14-33-b
315°C 17-13
265°C 14-44
235°C 14-41
255°C 14-15
315°C 14-17
545°C 14-23a
465°C 14-07
275°C 16-68
560°C 16-80
326°C 17-20
490°C 15b-10
445°C 14-31
540°C 17-25
540°C 14-28c
Gazik
Birjand
Jabisheh
Nehbandan
Gazik Fault
Esmail Fault
Dasht-e-Lut Fault
Est Tabnam Deh Fault
10 km
Paleocene of the Neh complex
Cretaceous of the Neh complex
Jurassic of the Lut Block
HP-BT suture zone (Bonnet et al, 2018)

Fig 7

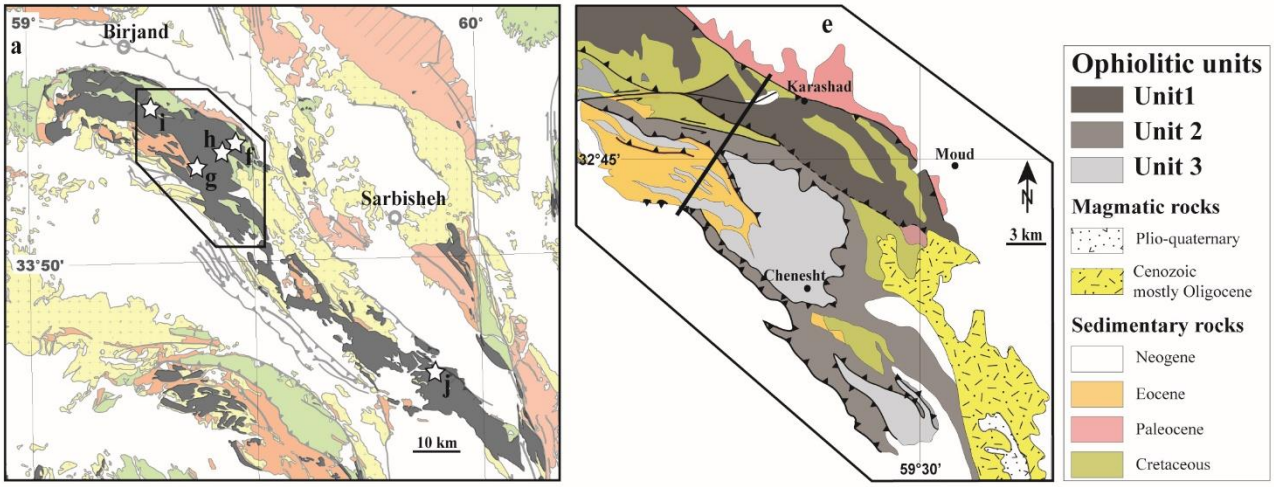
a
59°
60°
Birjand
33°50'
Sarbisheh
10 km
e
Karashad
32°45'
Moud
3 km
Cheneshk
59°30'
Ophiolitic units
Unit1
Unit 2
Unit 3
Magmatic rocks
Plio-quaternary
Cenozoic mostly Oligocene
Sedimentary rocks
Neogene
Eocene
Paleocene
Cretaceous

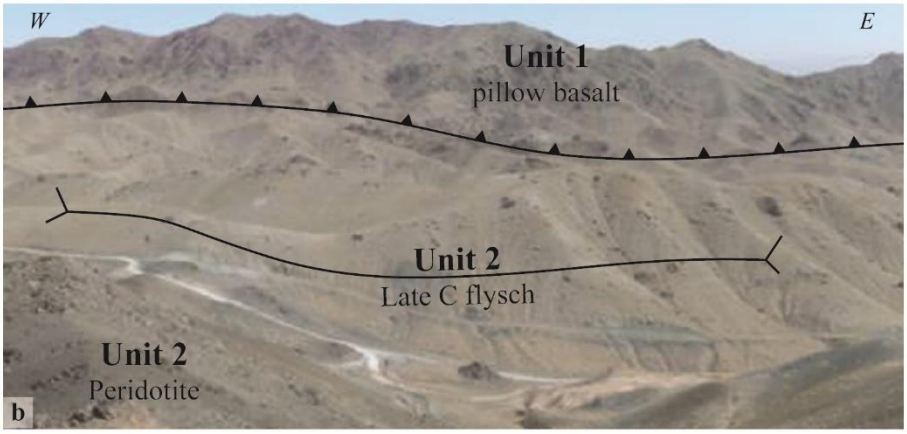
W
E
Unit 1
pillow basalt
Unit 2
Late C flysch
Unit 2
Peridotite
b

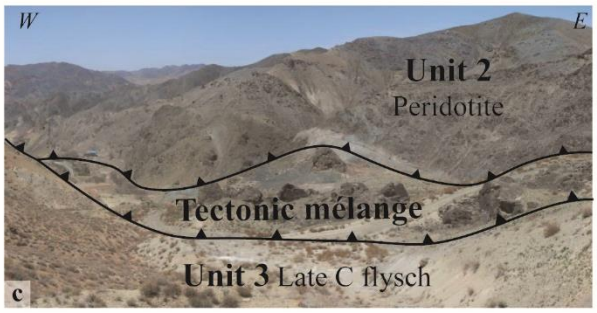
W
E
Unit 2
Peridotite
Tectonic mélange
Unit 3 Late C flysch
c

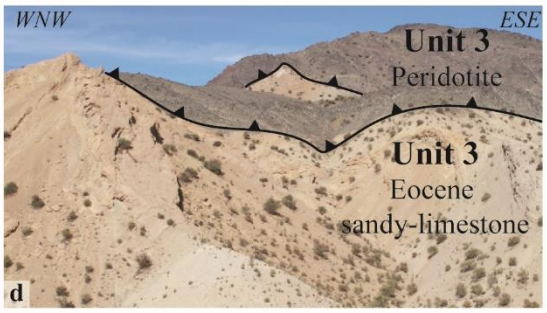
WNW
ESE
Unit 3
Peridotite
Unit 3
Eocene
sandy-limestone
d

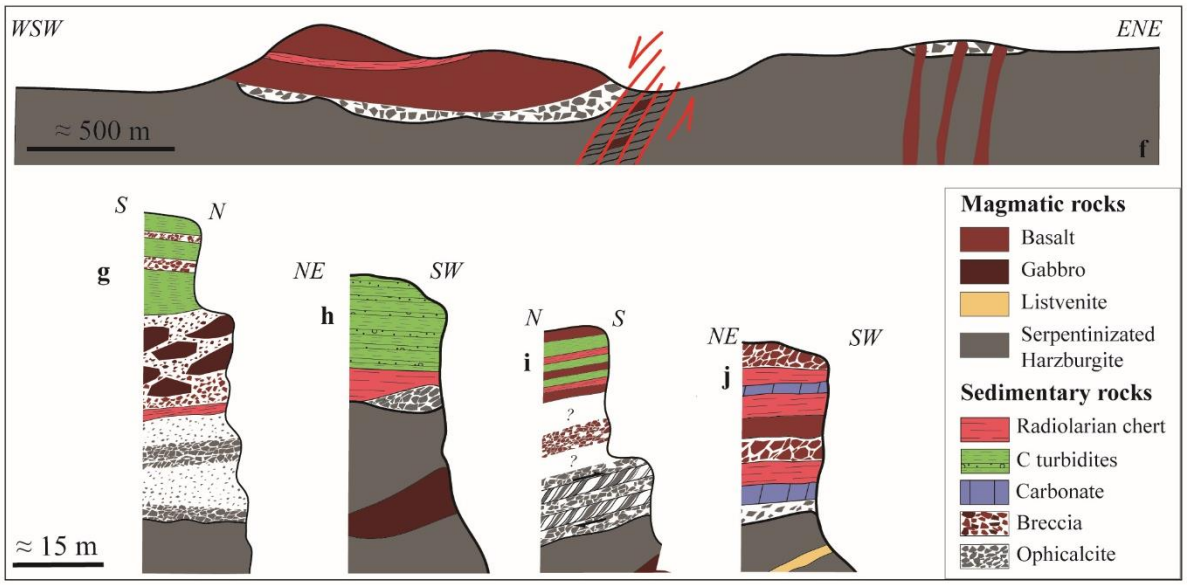
WSW
ENE
≈ 500 m
f
S
N
g
NE
SW
h
N
S
i
NE
SW
j
≈ 15 m
Magmatic rocks
Basalt
Gabbro
Listvenite
Serpentinizated Harzburgite
Sedimentary rocks
Radiolarian chert
C turbidites
Carbonate
Breccia
Ophicalcite

Fig 8

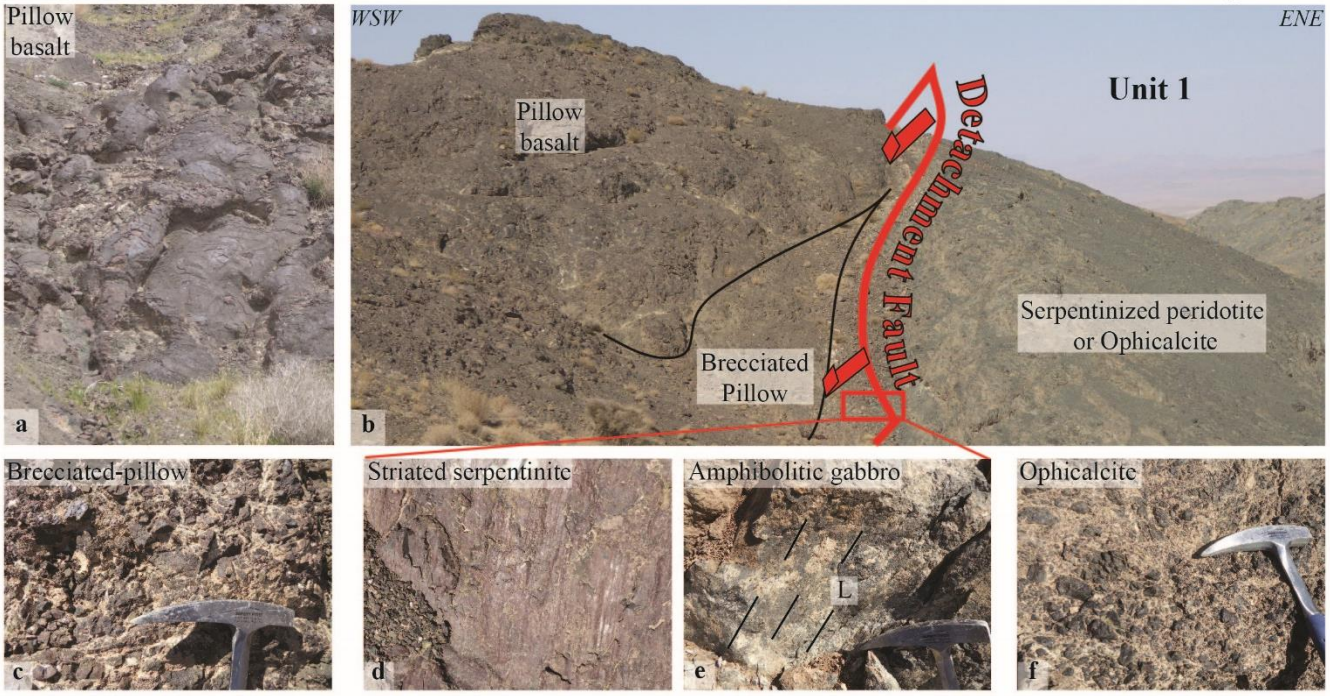
Pillow basalt
a
WSW
ENE
Unit 1
Pillow basalt
Detachment Fault
Serpentinized peridotite or Ophicalcite
Brecciated Pillow
b
Brecciated-pillow
c
Striated serpentinite
d
Amphibolitic gabbro
L
e
Ophicalcite
f

Fig 8 continued

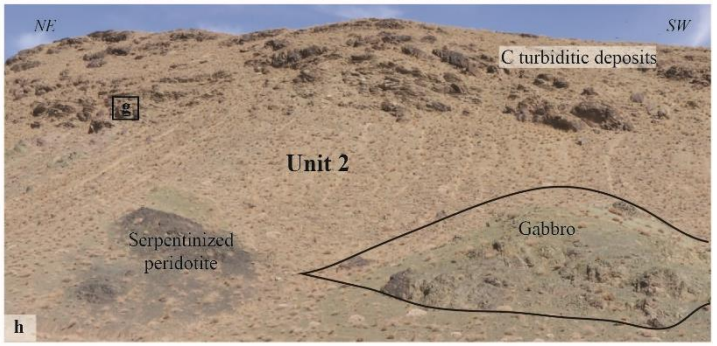

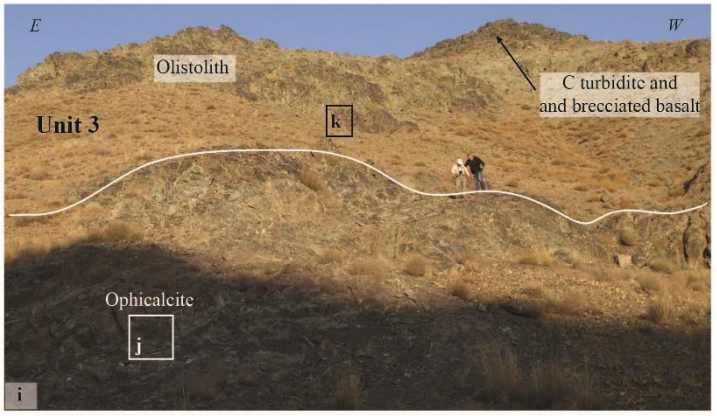

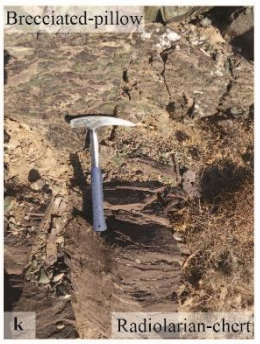

Fig 9

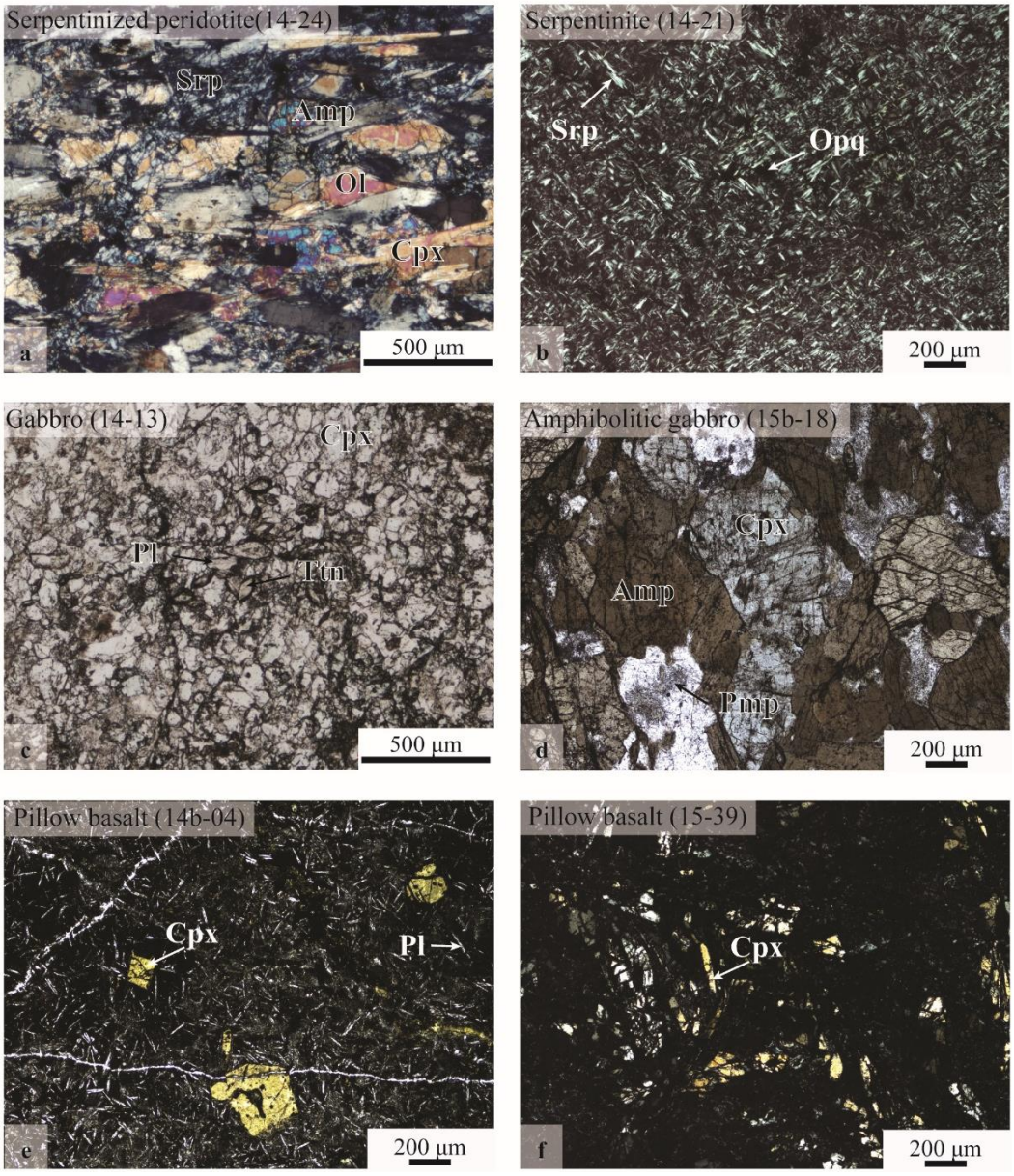
Serpentinized peridotite(14-24)
Srp
Amp
Ol
Cpx
500 μm
a
Serpentinite (14-21)
Srp
Opq
200 μm
b
Gabbro (14-13)
Cpx
Pl
Ttn
500 μm
c
Amphibolitic gabbro (15b-18)
Cpx
Amp
Pmp
200 μm
d
Pillow basalt (14b-04)
Cpx
Pl
200 μm
e
Pillow basalt (15-39)
Cpx
200 μm
f

Fig 10

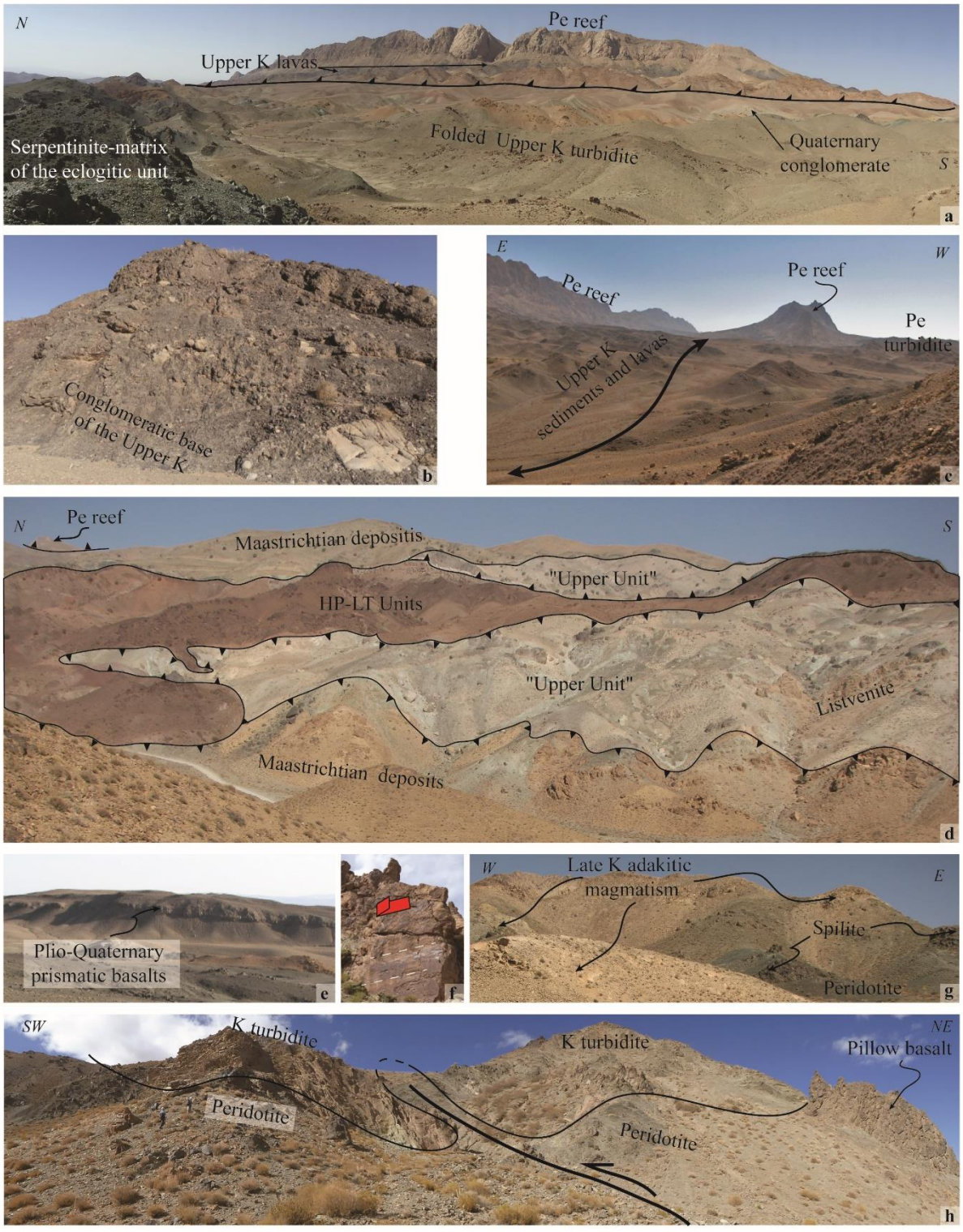
N
Pe reef
Upper K lavas
Serpentinite-matrix
of the eclogitic unit
Folded Upper K turbidite
Quaternary
conglomerate
S
a
Conglomeratic base
of the Upper K
b
E
W
Pe reef
Pe reef
Pe
turbidite
Upper K
sediments and lavas
c
N
Pe reef
S
Maastrichtian depositis
"Upper Unit"
HP-LT Units
"Upper Unit"
Listvenite
Maastrichtian deposits
d
Plio-Quaternary
prismatic basalts
e
f
W
Late K adakitic
magmatism
E
Spilite
Peridotite
g
SW
K turbidite
K turbidite
NE
Pillow basalt
Peridotite
Peridotite
h

Fig 10 continued

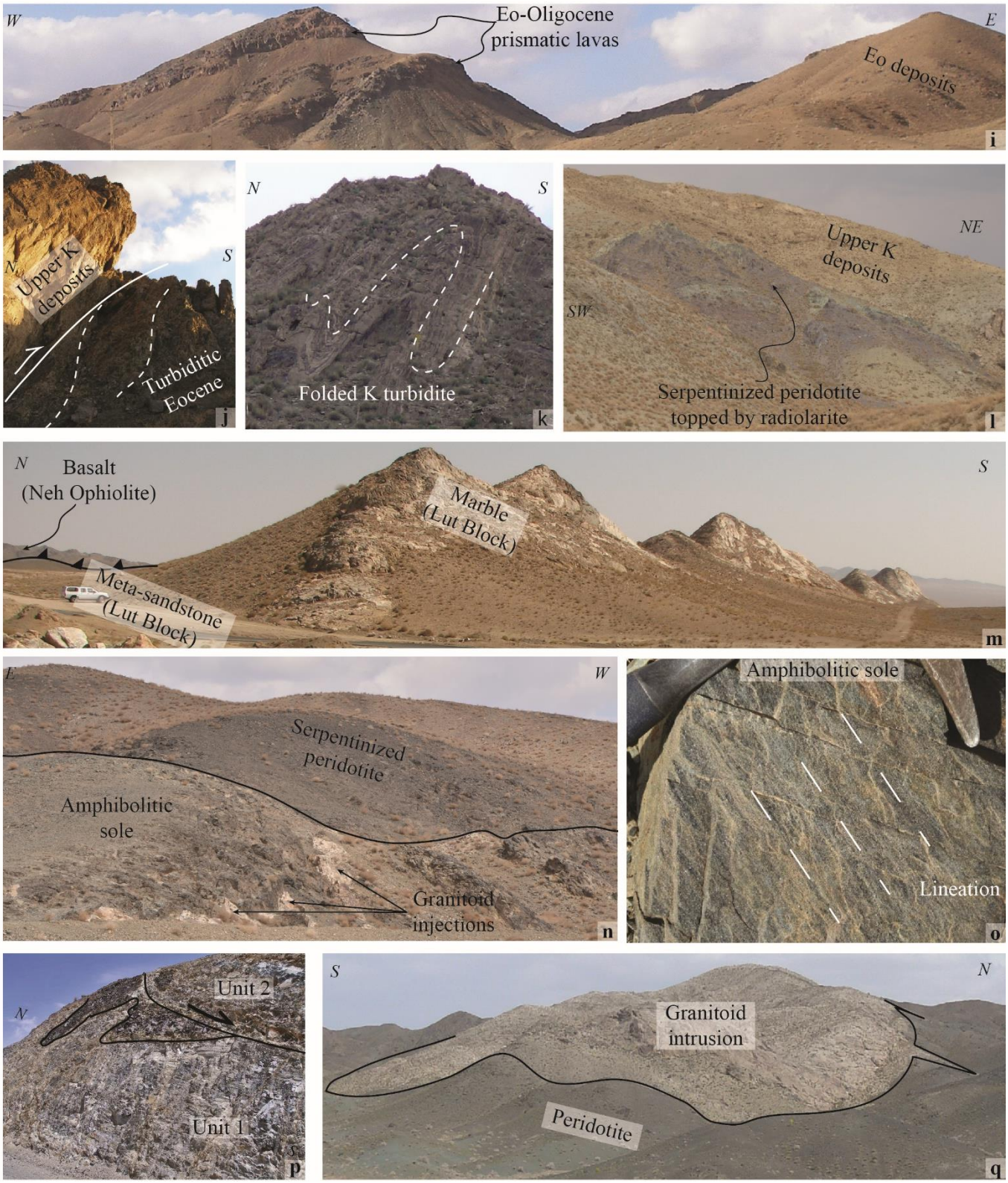

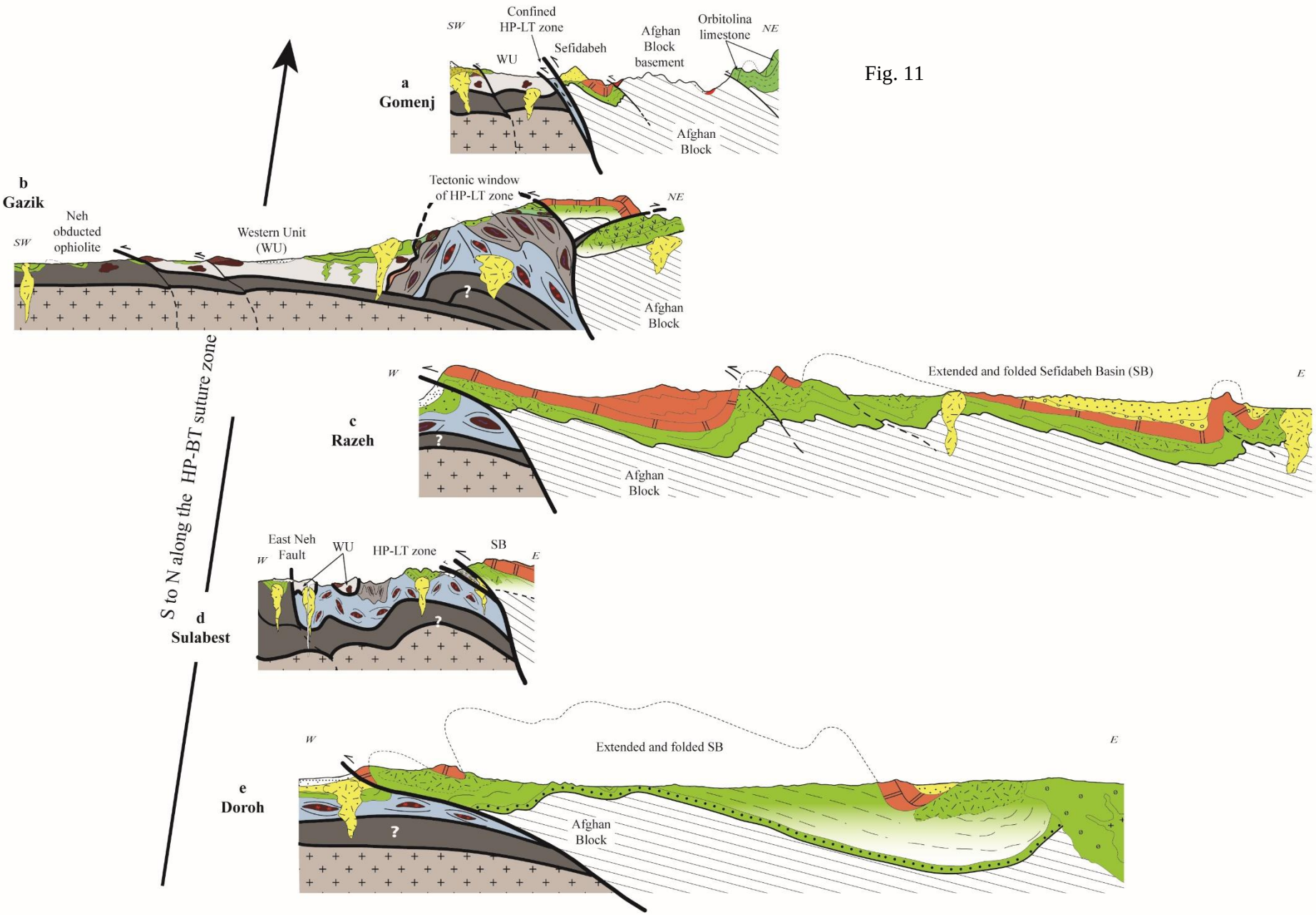
a
Gomenj
SW
Confined
HP-LT zone
Sefidabeh
WU
Afghan
Block
basement
Orbitolina
limestone
NE
Afghan
Block
b
Gazik
SW
Neh
obducted
ophiolite
Western Unit
(WU)
Tectonic window
of HP-LT zone
NE
?
Afghan
Block
S to N along the HP-BT suture zone
c
Razeh
W
Extended and folded Sefidabeh Basin (SB)
E
?
Afghan
Block
d
Sulabest
W
East Neh
Fault
WU
HP-LT zone
SB
E
?
e
Doroh
W
Extended and folded SB
E
?
Afghan
Block

Fig. 11

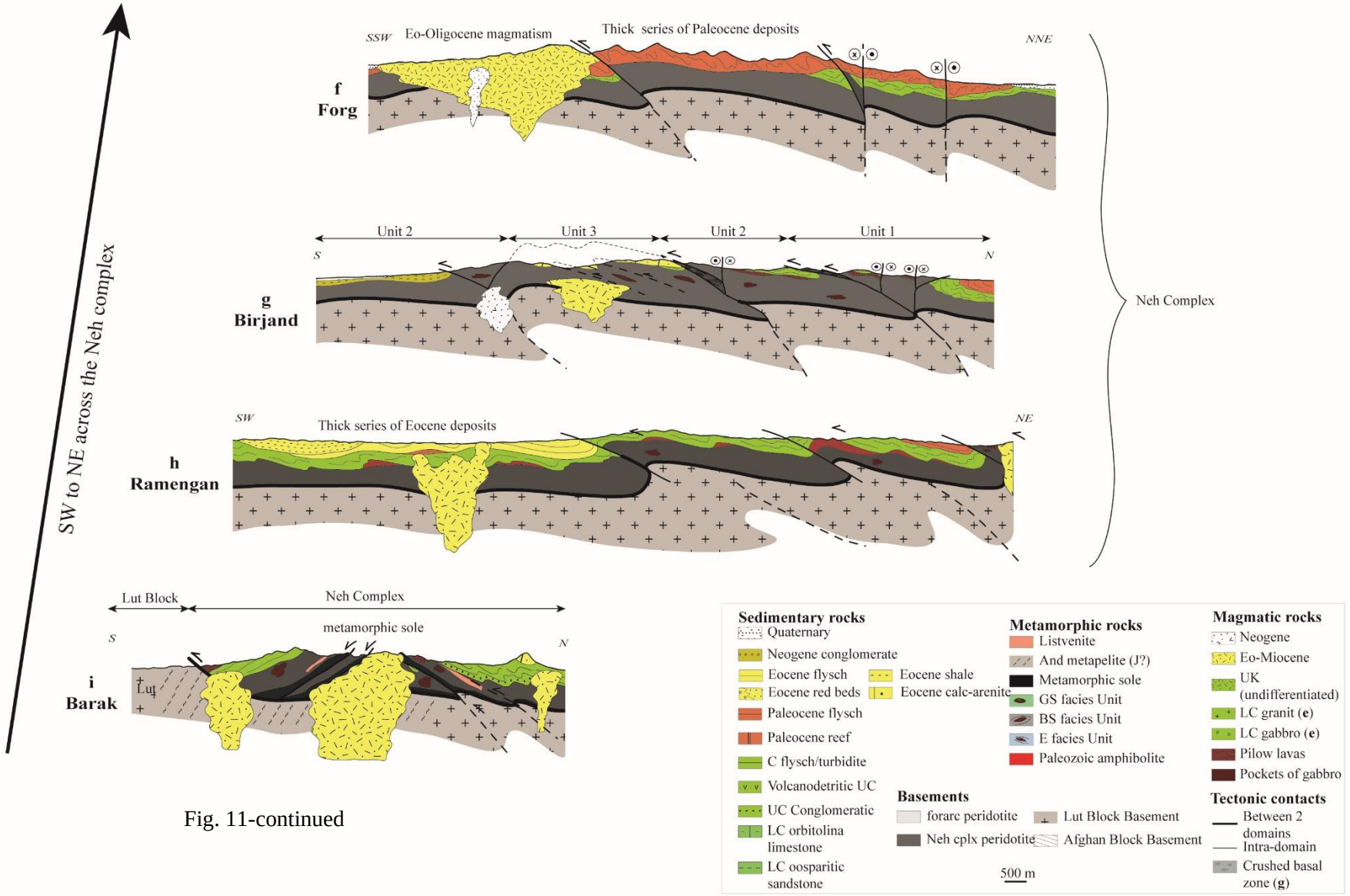

Fig. 11-continued

Fig 12

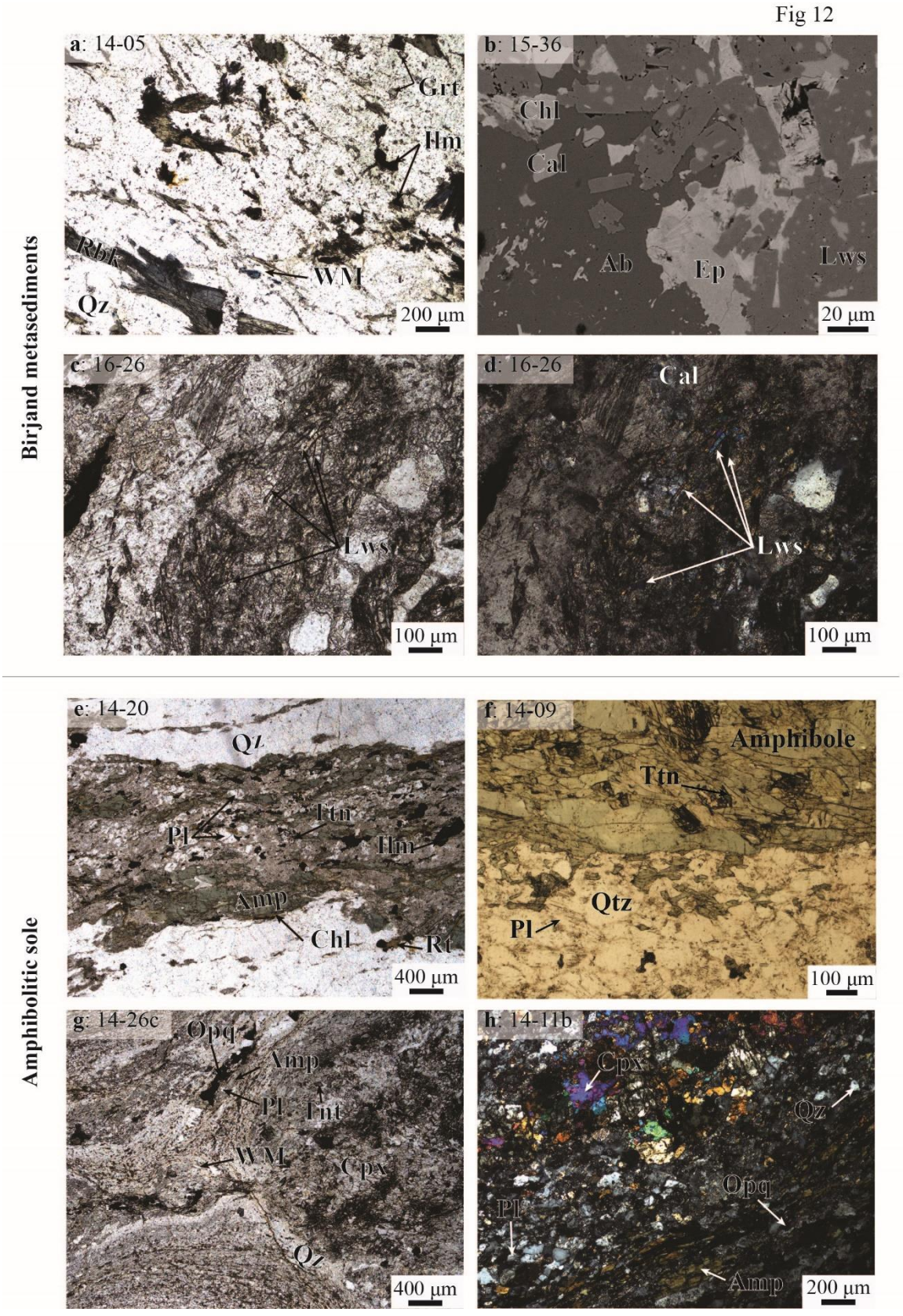
Birjand metasediments
a: 14-05
Grt
Hm
Rbk
WM
Qz
200 µm
b: 15-36
Chl
Cal
Ab
Ep
Lws
20 µm
c: 16-26
Lws
100 µm
d: 16-26
Cal
Lws
100 µm
Amphibolitic sole
e: 14-20
Qz
Pl
Ttn
Ilm
Amp
Chl
Rt
400 µm
f: 14-09
Amphibole
Ttn
Qtz
Pl
100 µm
g: 14-26c
Opq
Amp
Pl
Ent
WM
Cpx
Qz
400 µm
h: 14-11b
Cpx
Qz
Opq
Pl
Amp
200 µm

Fig 12-continued

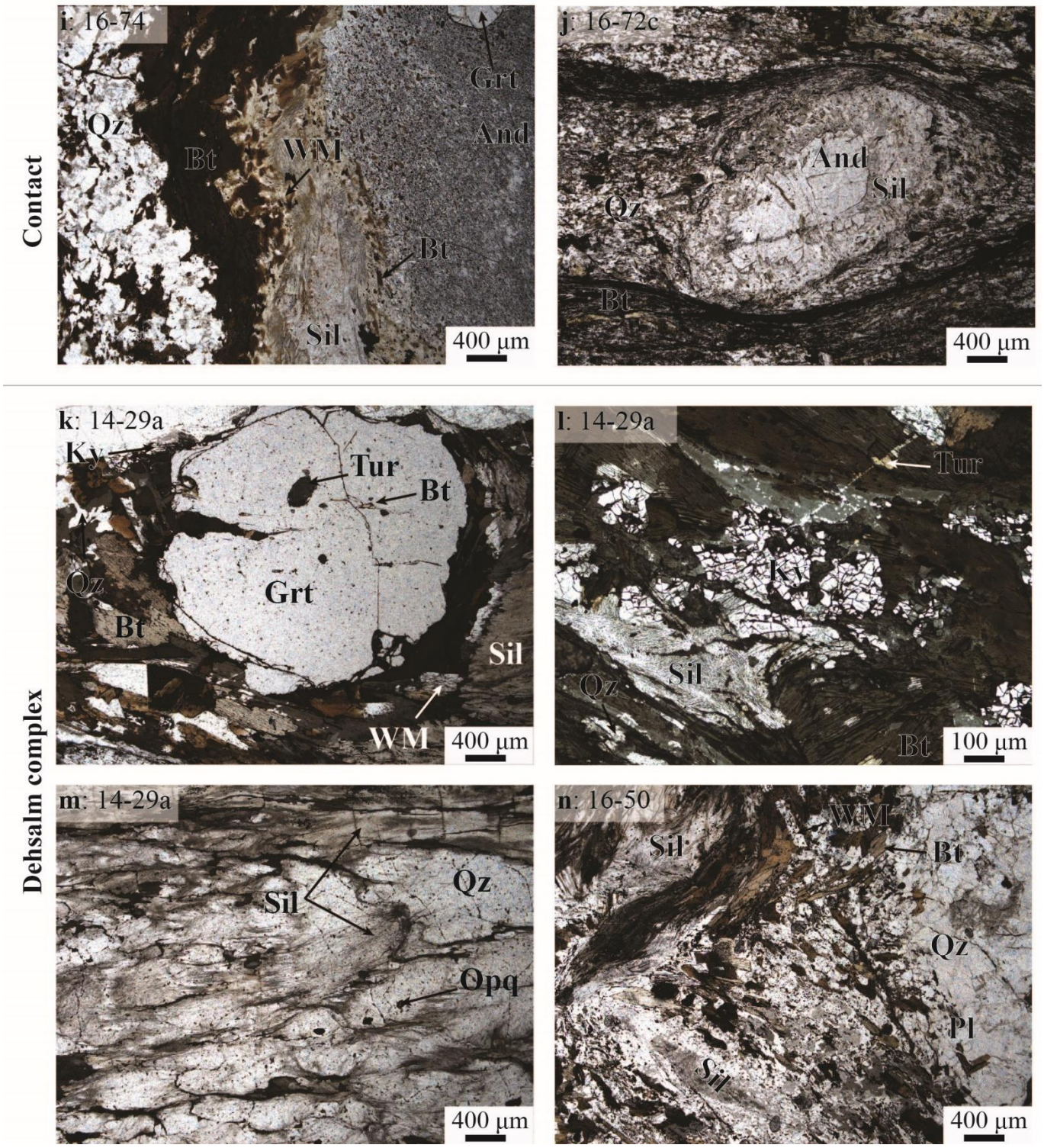

Fig 13

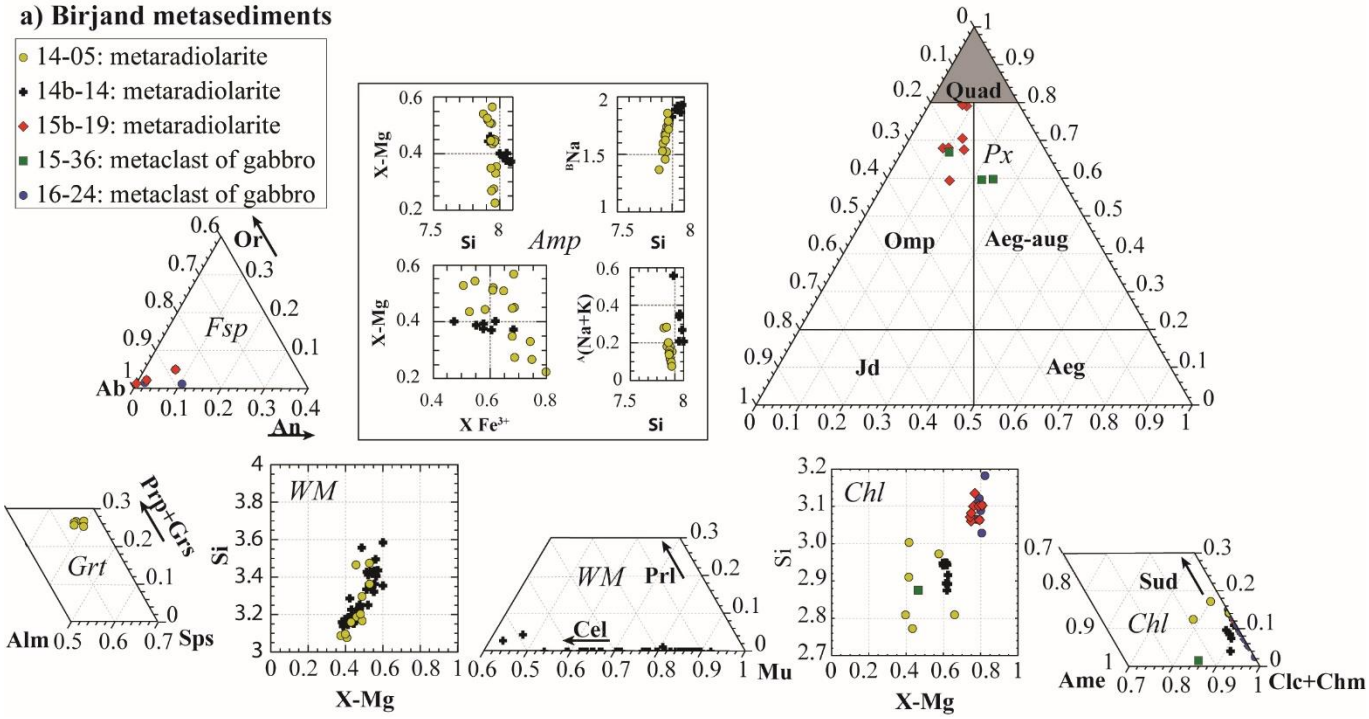
a) Birjand metasediments
14-05: metaradiolarite
14b-14: metaradiolarite
15b-19: metaradiolarite
15-36: metaclast of gabbro
16-24: metaclast of gabbro
Or
Fsp
Ab
An
Amp
X-Mg
Si
X Fe3+
Quad
Px
Omp
Aeg-aug
Jd
Aeg
Grt
Prp+Grs
Alm
Sps
WM
Prl
Cel
Mu
Chl
Sud
Ame
Clc+Chm

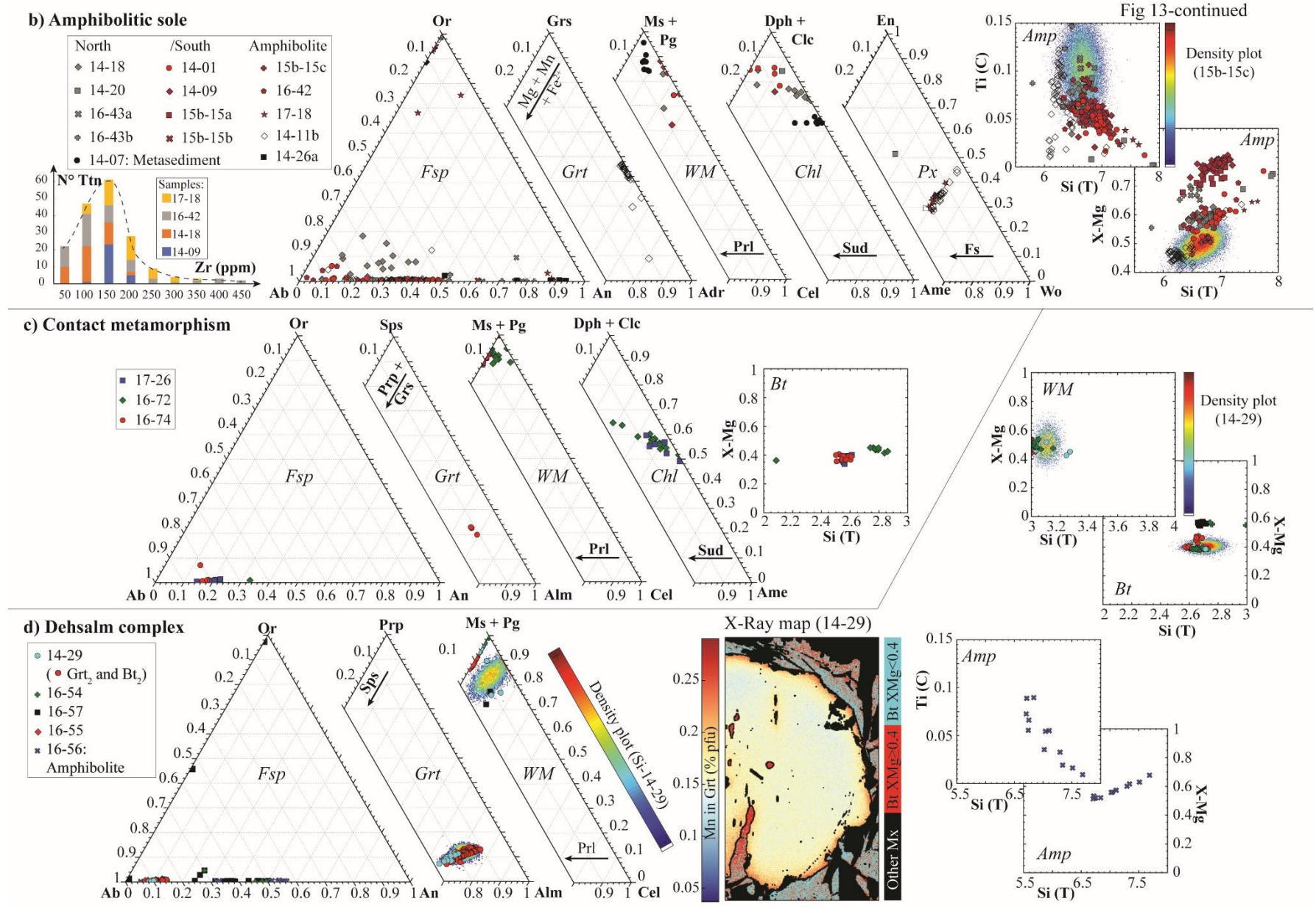
Fig 13-continued
b) Amphibolitic sole
North /South Amphibolite
14-18 14-01 15b-15c
14-20 14-09 16-42
16-43a 15b-15a 17-18
16-43b 15b-15b 14-11b
14-07: Metasediment 14-26a
N° Ttn
Samples: 17-18 16-42 14-18 14-09
Zr (ppm)
Or Grs Ms + Pg Dph + Clc En
Fsp Grt WM Chl Px
Mg + Mn + Fe2+
Prl Sud Fs
Ab An Adr Cel Ame Wo
Amp
Ti (C)
Si (T)
X-Mg
Density plot (15b-15c)
c) Contact metamorphism
17-26 16-72 16-74
Or Sps Ms + Pg Dph + Clc
Prp + Grs
Fsp Grt WM Chl
Prl Sud
Ab An Alm Cel Ame
Bt
WM
Density plot (14-29)
d) Dehsalm complex
14-29 (Grt2 and Bt2)
16-54 16-57 16-55 16-56: Amphibolite
Or Prp Ms + Pg
Sps
Density plot (Si-14-29)
X-Ray map (14-29)
Mn in Grt (% pfu)
Bt XMg≥0.4
Bt XMg<0.4
Other Mx

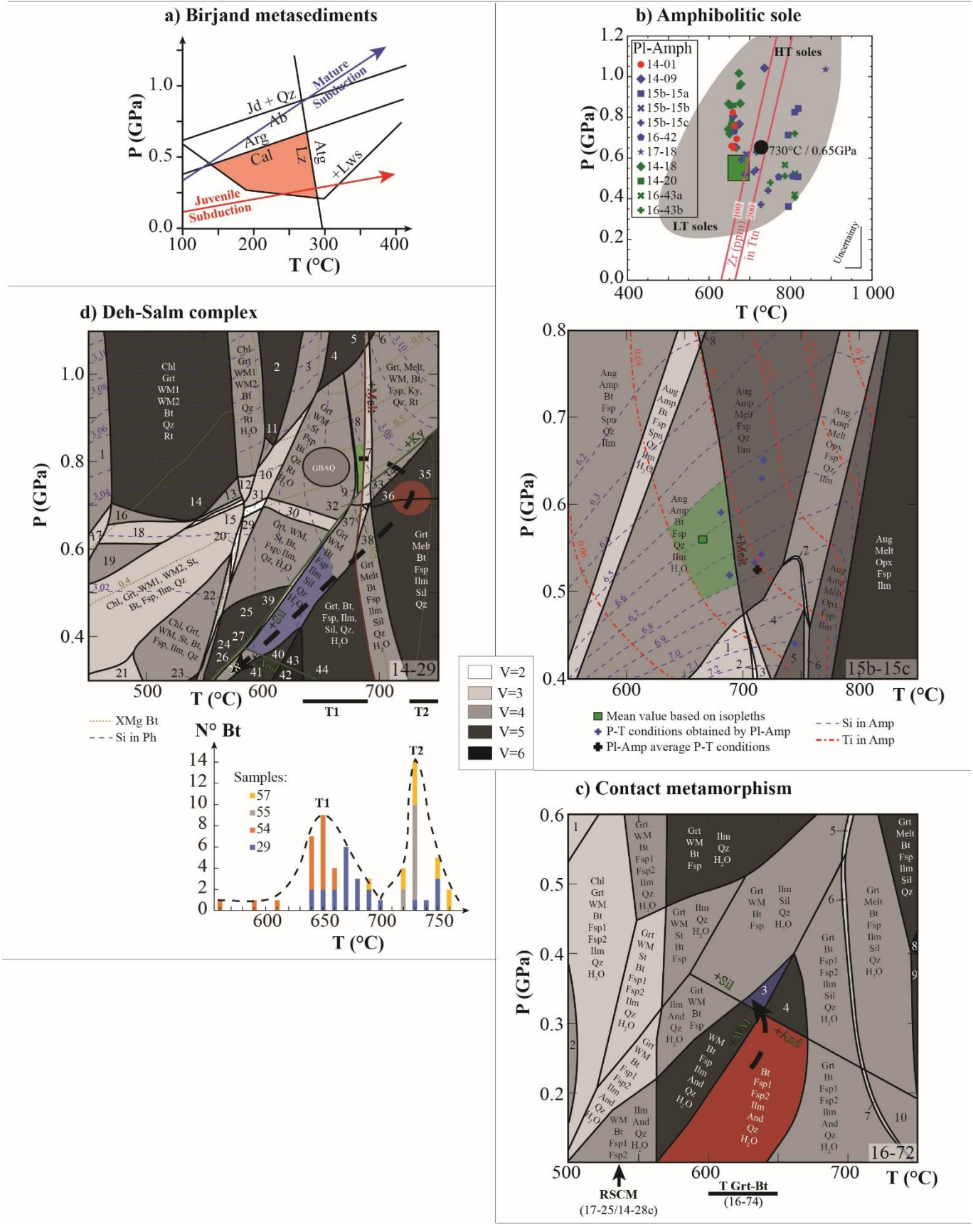
a) Birjand metasediments
P (GPa)
T (°C)
Jd + Qz
Ab
Arg
Cal
Lz
Atg
+Lws
Mature Subduction
Juvenile Subduction
b) Amphibolitic sole
Pl-Amph
14-01
14-09
15b-15a
15b-15b
15b-15c
16-42
17-18
14-18
14-20
16-43a
16-43b
HT soles
LT soles
730°C / 0.65GPa
Zr (ppm) in Ttn
100
200
Uncertainty
d) Deh-Salm complex
14-29
GBAQ
T1
T2
XMg Bt
Si in Ph
N° Bt
Samples:
57
55
54
29
V=2
V=3
V=4
V=5
V=6
15b-15c
Mean value based on isopleths
P-T conditions obtained by Pl-Amp
Pl-Amp average P-T conditions
Si in Amp
Ti in Amp
c) Contact metamorphism
16-72
RSCM
(17-25/14-28c)
T Grt-Bt
(16-74)

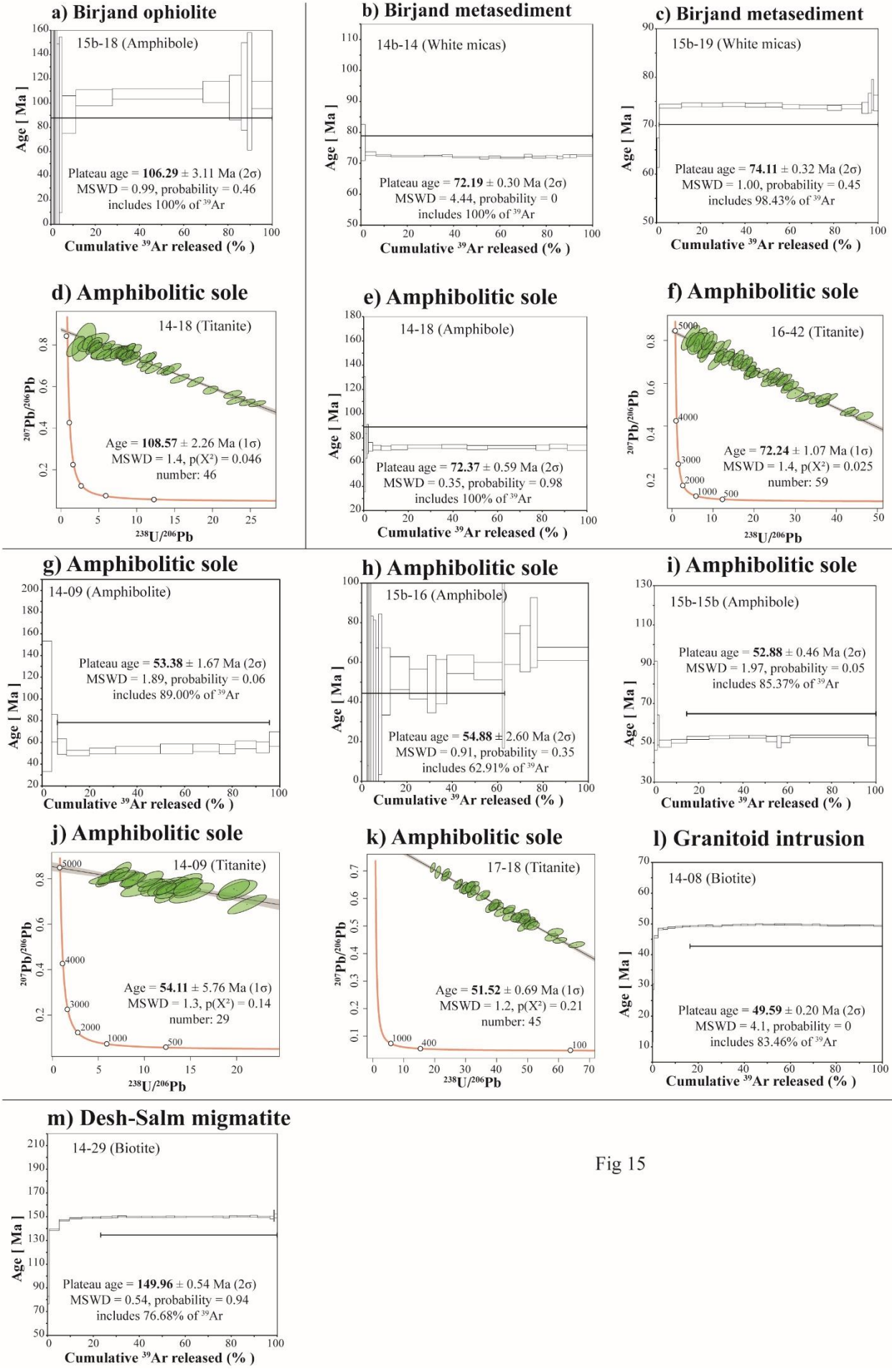
a) Birjand ophiolite
15b-18 (Amphibole)
Plateau age = 106.29 ± 3.11 Ma (2σ)
MSWD = 0.99, probability = 0.46
includes 100% of 39Ar
Age [Ma]
Cumulative 39Ar released (%)
b) Birjand metasediment
14b-14 (White micas)
Plateau age = 72.19 ± 0.30 Ma (2σ)
MSWD = 4.44, probability = 0
includes 100% of 39Ar
Age [Ma]
Cumulative 39Ar released (%)
c) Birjand metasediment
15b-19 (White micas)
Plateau age = 74.11 ± 0.32 Ma (2σ)
MSWD = 1.00, probability = 0.45
includes 98.43% of 39Ar
Age [Ma]
Cumulative 39Ar released (%)
d) Amphibolitic sole
14-18 (Titanite)
Age = 108.57 ± 2.26 Ma (1σ)
MSWD = 1.4, p(X²) = 0.046
number: 46
207Pb/206Pb
238U/206Pb
e) Amphibolitic sole
14-18 (Amphibole)
Plateau age = 72.37 ± 0.59 Ma (2σ)
MSWD = 0.35, probability = 0.98
includes 100% of 39Ar
Age [Ma]
Cumulative 39Ar released (%)
f) Amphibolitic sole
16-42 (Titanite)
Age = 72.24 ± 1.07 Ma (1σ)
MSWD = 1.4, p(X²) = 0.025
number: 59
207Pb/206Pb
238U/206Pb
g) Amphibolitic sole
14-09 (Amphibolite)
Plateau age = 53.38 ± 1.67 Ma (2σ)
MSWD = 1.89, probability = 0.06
includes 89.00% of 39Ar
Age [Ma]
Cumulative 39Ar released (%)
h) Amphibolitic sole
15b-16 (Amphibole)
Plateau age = 54.88 ± 2.60 Ma (2σ)
MSWD = 0.91, probability = 0.35
includes 62.91% of 39Ar
Age [Ma]
Cumulative 39Ar released (%)
i) Amphibolitic sole
15b-15b (Amphibole)
Plateau age = 52.88 ± 0.46 Ma (2σ)
MSWD = 1.97, probability = 0.05
includes 85.37% of 39Ar
Age [Ma]
Cumulative 39Ar released (%)
j) Amphibolitic sole
14-09 (Titanite)
Age = 54.11 ± 5.76 Ma (1σ)
MSWD = 1.3, p(X²) = 0.14
number: 29
207Pb/206Pb
238U/206Pb
k) Amphibolitic sole
17-18 (Titanite)
Age = 51.52 ± 0.69 Ma (1σ)
MSWD = 1.2, p(X²) = 0.21
number: 45
207Pb/206Pb
238U/206Pb
l) Granitoid intrusion
14-08 (Biotite)
Plateau age = 49.59 ± 0.20 Ma (2σ)
MSWD = 4.1, probability = 0
includes 83.46% of 39Ar
Age [Ma]
Cumulative 39Ar released (%)
m) Desh-Salm migmatite
14-29 (Biotite)
Plateau age = 149.96 ± 0.54 Ma (2σ)
MSWD = 0.54, probability = 0.94
includes 76.68% of 39Ar
Age [Ma]
Cumulative 39Ar released (%)

Fig 15

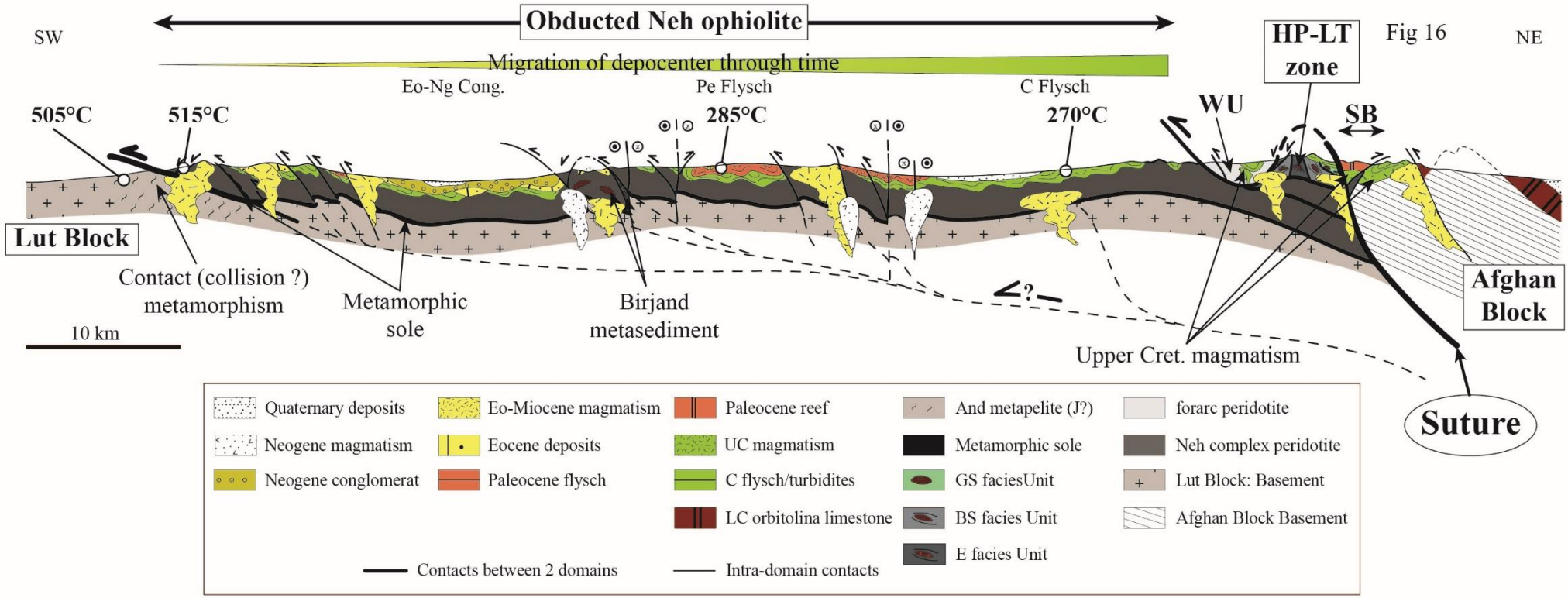
SW
Obducted Neh ophiolite
NE
Fig 16
HP-LT zone
Migration of depocenter through time
Eo-Ng Cong.
Pe Flysch
C Flysch
505°C
515°C
285°C
270°C
WU
SB
Lut Block
Contact (collision ?) metamorphism
Metamorphic sole
Birjand metasediment
10 km
Upper Cret. magmatism
Afghan Block
Suture
Quaternary deposits
Neogene magmatism
Neogene conglomerat
Eo-Miocene magmatism
Eocene deposits
Paleocene flysch
Paleocene reef
UC magmatism
C flysch/turbidites
LC orbitolina limestone
And metapelite (J?)
Metamorphic sole
GS faciesUnit
BS facies Unit
E facies Unit
forarc peridotite
Neh complex peridotite
Lut Block: Basement
Afghan Block Basement
Contacts between 2 domains
Intra-domain contacts

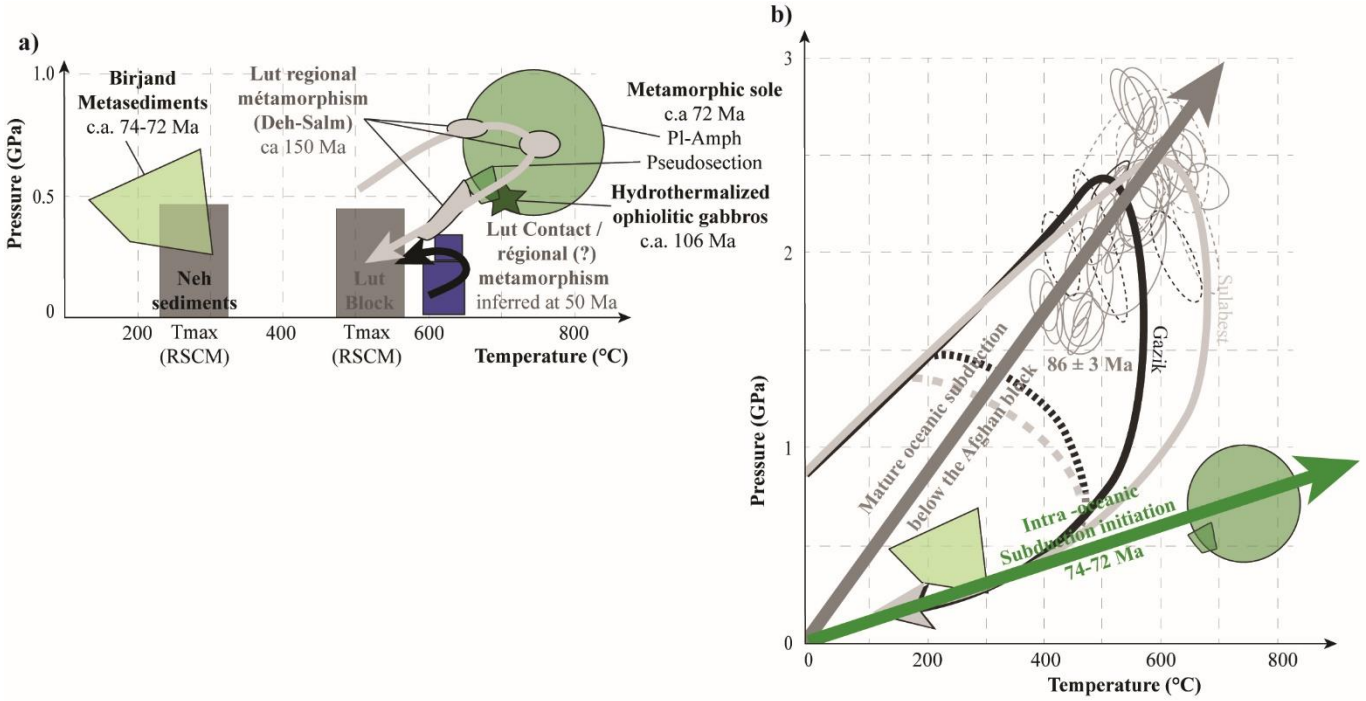
a)
Pressure (GPa)
1.0
0.5
0
Birjand
Metasediments
c.a. 74-72 Ma
Neh
sediments
Lut regional
métamorphism
(Deh-Salm)
ca 150 Ma
Lut
Block
Metamorphic sole
c.a 72 Ma
Pl-Amph
Pseudosection
Hydrothermalized
ophiolitic gabbros
c.a. 106 Ma
Lut Contact /
régional (?)
metamorphism
inferred at 50 Ma
200
Tmax
(RSCM)
400
Tmax
(RSCM)
600
800
Temperature (°C)
b)
Pressure (GPa)
3
2
1
0
Mature oceanic subduction
below the Afghan block
86 ± 3 Ma
Gazik
Sulabest
Intra -Oceanic
Subduction initiation
74-72 Ma
0
200
400
600
800
Temperature (°C)

Fig. 17

Fig. 18

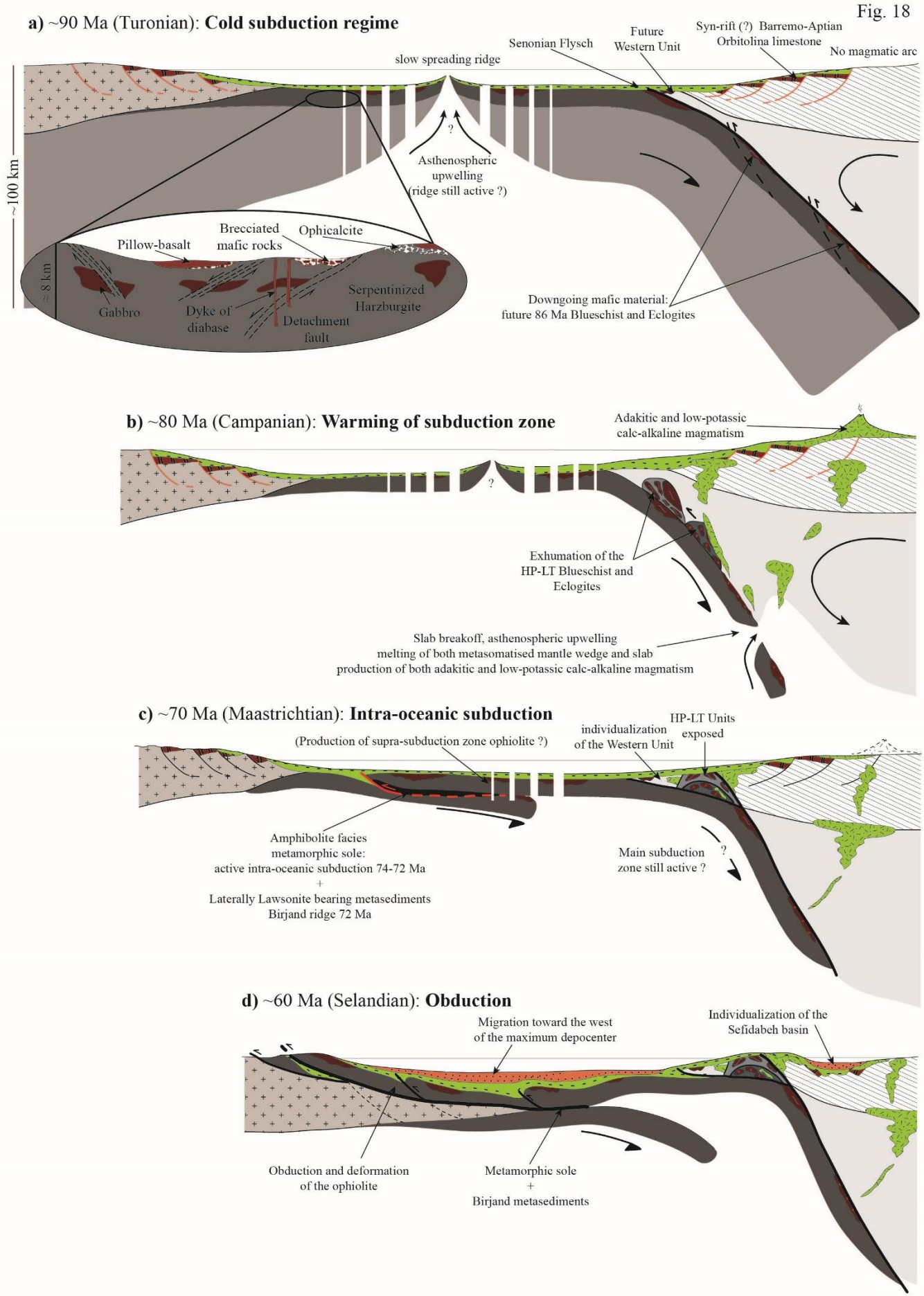
a) ~90 Ma (Turonian): Cold subduction regime
Senonian Flysch
Future Western Unit
Syn-rift (?) Barremo-Aptian Orbitolina limestone
No magmatic arc
slow spreading ridge
?
Asthenospheric upwelling (ridge still active ?)
~100 km
Pillow-basalt
Brecciated mafic rocks
Ophicalcite
≈ 8 km
Gabbro
Dyke of diabase
Detachment fault
Serpentinized Harzburgite
Downgoing mafic material: future 86 Ma Blueschist and Eclogites
b) ~80 Ma (Campanian): Warming of subduction zone
Adakitic and low-potassic calc-alkaline magmatism
?
Exhumation of the HP-LT Blueschist and Eclogites
Slab breakoff, asthenospheric upwelling
melting of both metasomatised mantle wedge and slab
production of both adakitic and low-potassic calc-alkaline magmatism
c) ~70 Ma (Maastrichtian): Intra-oceanic subduction
(Production of supra-subduction zone ophiolite ?)
individualization of the Western Unit
HP-LT Units exposed
Amphibolite facies metamorphic sole:
active intra-oceanic subduction 74-72 Ma
+
Laterally Lawsonite bearing metasediments
Birjand ridge 72 Ma
Main subduction zone still active ?
?
d) ~60 Ma (Selandian): Obduction
Migration toward the west of the maximum depocenter
Individualization of the Sefidabeh basin
Obduction and deformation of the ophiolite
Metamorphic sole
+
Birjand metasediments

Fig. 18-continued

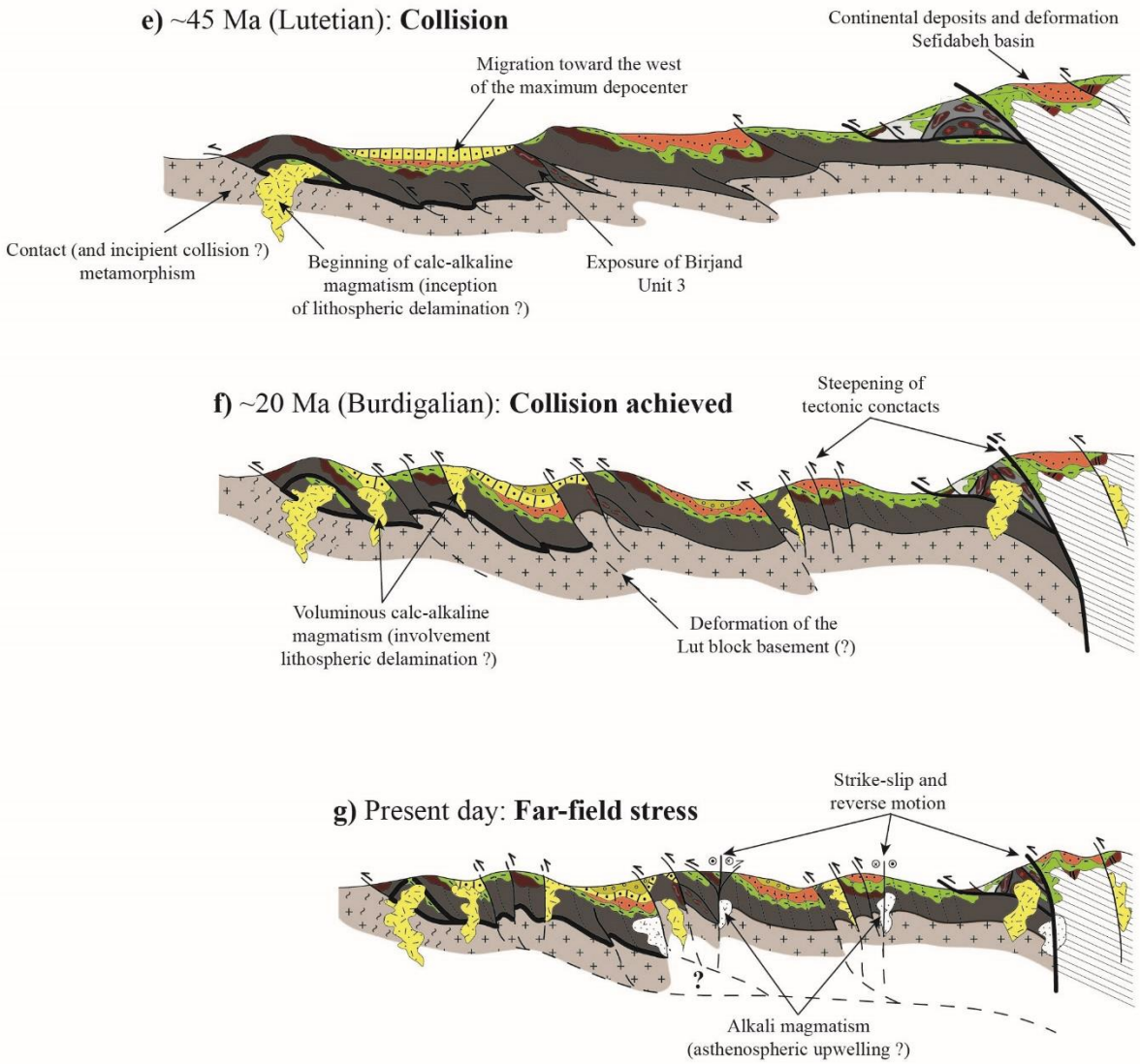

Fig. 19

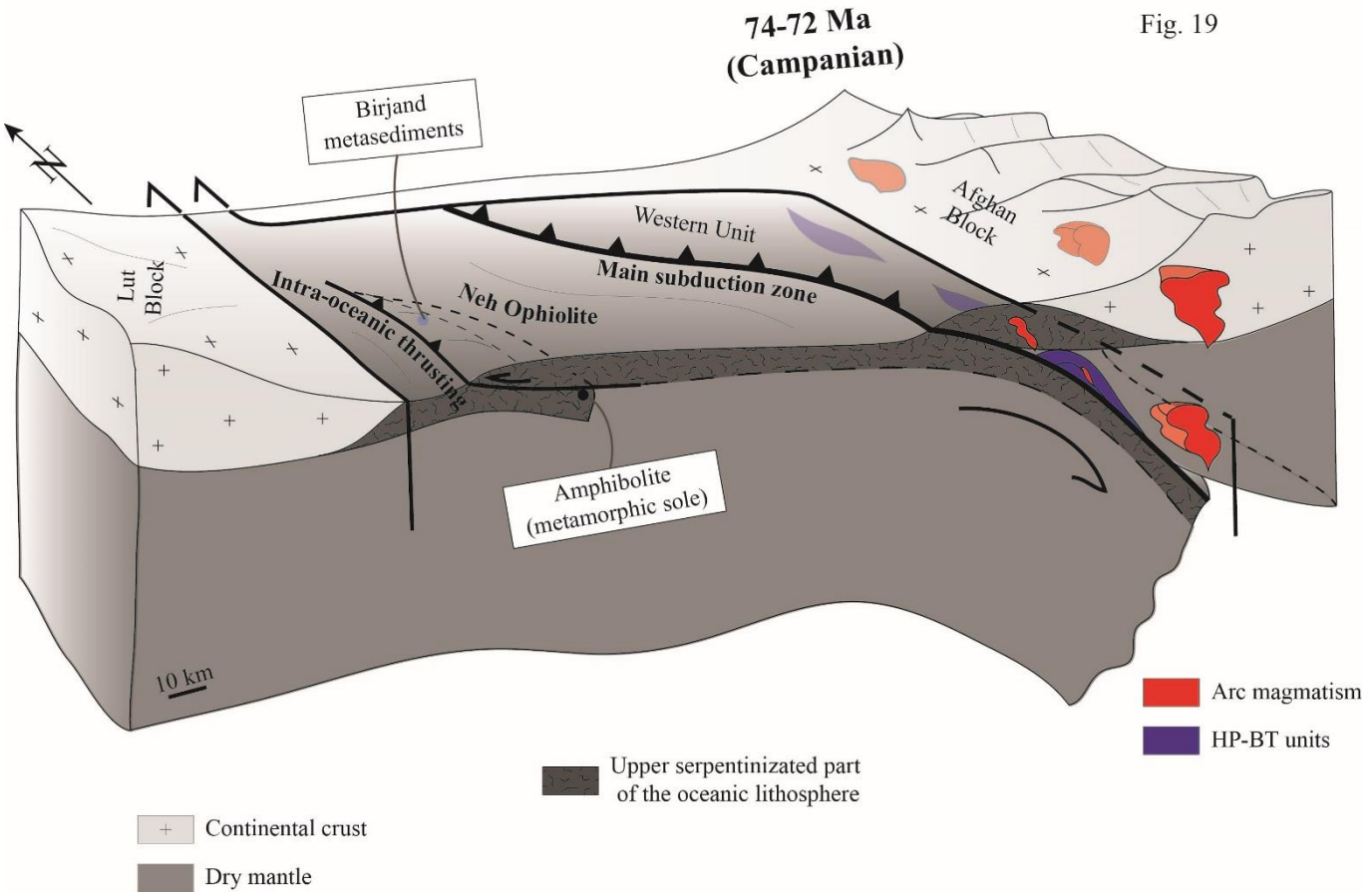
74-72 Ma
(Campanian)
Birjand
metasediments
N
Lut
Block
Intra-oceanic thrusting
Neh Ophiolite
Western Unit
Main subduction zone
Afghan
Block
Amphibolite
(metamorphic sole)
10 km
Arc magmatism
HP-BT units
Upper serpentinizated part
of the oceanic lithosphere
Continental crust
Dry mantle

Fig. 20

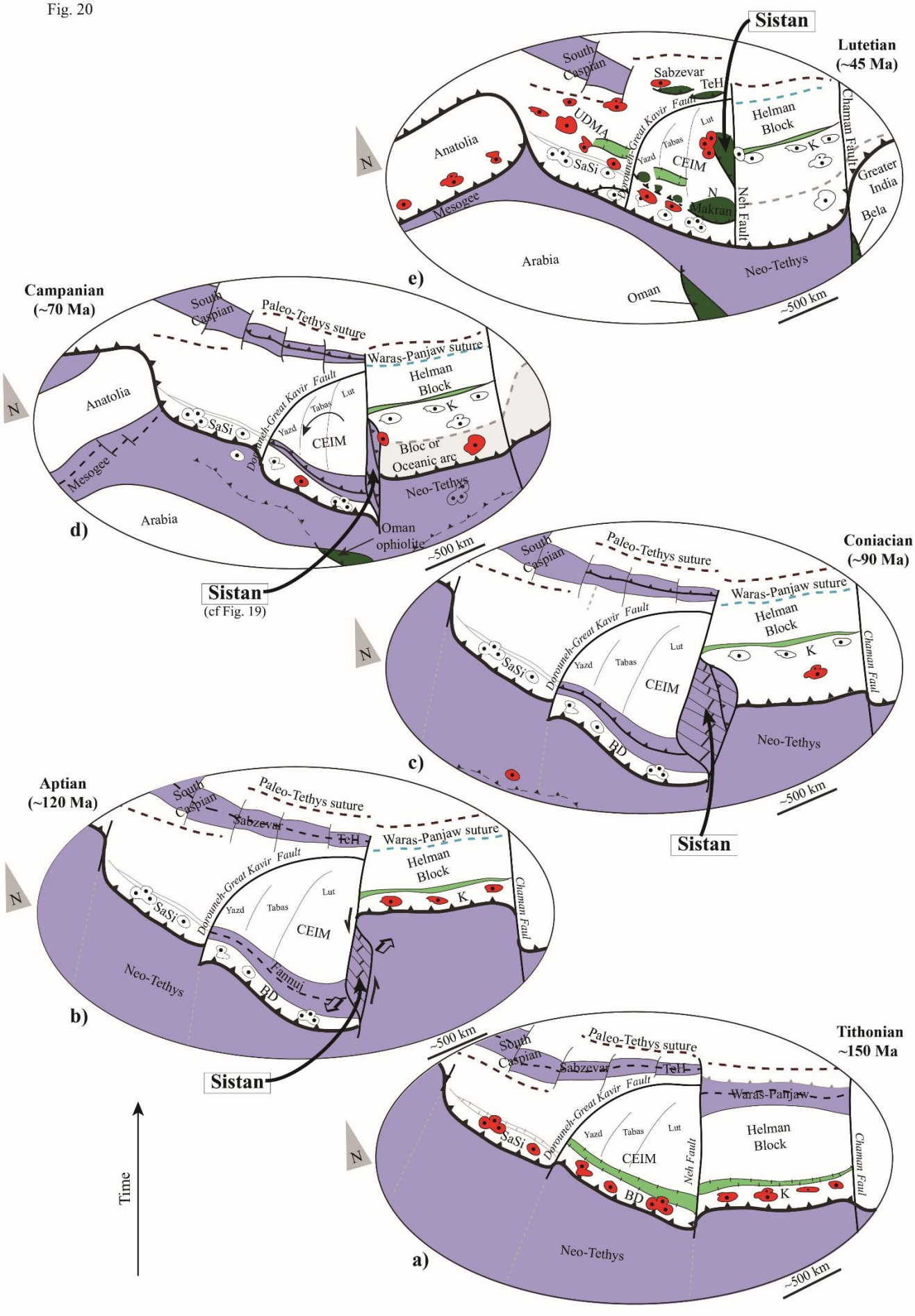
Sistan
Lutetian
(~45 Ma)
South Caspian
Sabzevar
TeH
UDMA
Dorouneh-Great Kavir Fault
Lut
Tabas
Yazd
CEIM
Helman Block
K
Chaman Fault
Greater India
Bela
Anatolia
SaSi
N
Makran
Neh Fault
Mesogee
Arabia
Neo-Tethys
Oman
~500 km
e)
Campanian
(~70 Ma)
Paleo-Tethys suture
Waras-Panjaw suture
Bloc or Oceanic arc
Oman ophiolite
d)
Sistan
(cf Fig. 19)
Coniacian
(~90 Ma)
BD
c)
Aptian
(~120 Ma)
Pannuj
b)
Tithonian
~150 Ma
Waras-Panjaw
a)
Time

Table

Table 1

N°	Name	Latitude	Longitude	Mineralogy											
Ophiolite				**Ol**	**Srp**	**Cpx**	**Opx**	**Pl**	**Amp**	**Ep**	**Ttn**	**Prh**	**Opq**	**Pmp**	**Cal**
14-24	Serpentinite	32°03'13.6"	59°24'42.6"	+++	+	+	++		+++++		+		+		
14-21	Serpentinite	32°17'31.4"	59°51'46.3		+++++								+		
15b-18	Gabbro Amph	32°40'43.7"	59°30'09.0"			++		(+)	++++			++		+	
16-01b	Gabbro Amph	32°40'43.7"	59°30'09.0"					+++	+++						
16-01c	Gabbro Amph	32°40'43.7"	59°30'09.0"			+		++	+++	+	+				
17-01	Gabbro Amph	32°30'4.8"	60°21'4.3"			++		+	+++	+		+			
14b-3	Basalt	32°47'27.0"	59°07'18.8"					++					+	+	+
14b-4	Basalt	32°47'24.5"	59°07'43.4"					++		+			+	+	+
15-39	Basalt	32°49'38.4"	59°08'8.5"			+++		+		+			+		

N°	Name	Latitude	Longitude	Mineralogy														
Birjand metasediment				**Qz**	**Pl**	**Amp**	**Grt**	**Ph**	**Chl**	**Ep**	**Opq**	**Cal**	**Lws**	**Cpx**	**Ap**	**Srp**	**Ttn**	**Pmp**
14-04a	Chert	32°43'42"	59°19'03.6"	++++++	+++	Rbk ++			+	+	ilm +							
14-04b	Chert	32°43'42"	59°19'03.6"	++++++	+++	Rbk ++		+	+	+	+							
14-05	Chert	32°43'07.8"	59°19'42.4"	++++++	+++	Rbk ++	+	+	+	+	ilm +							
14b-14	Chert	32°43'08.2"	59°19'42.2"	++++++	+++	Rbk ++	+	+	+		ilm +							
15b-19	Chert	32° 0'15.50"	59°34'41.40"	++++++	+++	Rbk ++		+	++		ilm +		Omp ++					
15-36	Brecciated gabbro	32°41'39.8"	59°21'11.9"		+++	+++			+	+	+		++	Aeg ++	(+)		+	+
16-24	Brecciated gabbro	32°41'08.5"	59°21'26.8"		+++								++	+++				
16-26	Spilitic-breccia	32°41'08.5"	59°21'26.8"			+						+++	++				+	+
16-21b	Ophicalcite	32°41'08.3"	59°21'24.3"				+				Mag +	++	+		Liz ++			

N°	Name	Latitude	Longitude	Mineralogy																
Deshalm metamorphic complex				**Qz**	**Bt**	**Sil**	**Ky**	**Grt**	**Opq**	**Tur**	**Kln**	**Cal**	**Rt**	**Mnz**	**Pl**	**Chl**	**Amp**	**Ep**	**Ttn**	**Cpx**	**Or**	**Ph**	**OM**
16-57	Micaschist	31°22'16.9"	59°32'18.9"	+++	+++	+++		+	+	+			+	+	+	+							+
16-54	Micaschist	31°21'48.0"	59°32'06.5"	+++	+++	++			+	+	+				+							+	
16-55	Micaschist	31°21'48.0"	59°32'06.5"	+++	+++	++	(+)		+						+	+					+	+	
14-29a	Migmatite	31°21'13.1"	59°31'53.4"	+++	+++	++	+	+	+	+	(+)	(+)		(+)	+							+	
14-29b	Migmatite	31°21'13.1"	59°31'53.4"	+++	+++	++	+		+	+		(+)			+								
14-29c	Migmatite	31°21'13.1"	59°31'53.4"	+++	+++	++	+	+	+	+						+		+					
16-50	Migmatite	31°22'40.6"	59°32'37.3"	+++	+++	++			+						++							+	
16-56	Amphibolite	31°22'16.9"	59°32'18.9"									+			+++		+++	+	+	++			

N°	Name	Latitude	Longitude	Mineralogy														
Contact metamorphism				**Qz**	**Bt**	**And**	**Sil**	**Ph**	**Pl**	**Grt**	**Opq**	**Tur**	**Ap**	**Cal**	**Prh**	**Chl**	**Ttn**	**OM**	**Zrn**
17-26	Micaschist	31°57'51.4"	59°30'42.1"	+++	+++	++	(+)	+	+			+				+			
16-72c	Micaschist	31°58'13.6"	59°29'08.0"	+++	+++	++	+	++	+		(+)		(+)	+		(+)		+++	+
16-74	Micaschist	31°58'29.1	59°29'06.0"	+++	+++	+	++	+	++	(+)					+	+			

Table 1-continued

N°	Name	Latitude	Longitude	Mineralogy																			
Amphibolitic sole				Amp	Pl	Cpx	Ttn	Qz	Ep	Grt	Ph	Opq	Rt	Mag	Bt	Or	Chl	Cal	Pmp	Prh	Ap	Aln	Zrn	OM
14-01	Amphibolite	32°43'33.9"	59°01'59.8"	++++	+++		+	++	+		+	Ilm +					+				(+)	(+)		
14-09	Amphibolite	32°00'04.7"	59°31'01.8"	++++	+++		++	++	+		+	Ilm +	+						+					
14-18	Amphibolite	32°17'30.9"	59°51'44.2"	++++	++++		++	(+)	+			+			(+)									
15b-15a	Amphibolite	31°59'58.7"	59°30'59.7"	++++	++++																			
15b-15b	Amphibolite	31°59'58.7"	59°30'59.7"	++++	++++																			
15b-15c	Amphibolite	31°59'58.7"	59°30'59.7"	++++	++++		+	++				Ilm +		+					+		+	+	+	
16-42	Amphibolite	32°17'40.4"	59°51'16.4"	++++	+++		++	++				+								+				
16-43b	Amphibolite	32°17'33.0"	59°51'04.2"	++++	++++			++																
16-45a	Amphibolite	32°17'32.7"	59°51'03.4"	++++	+			++																
16-45b	Amphibolite	32°17'32.7"	59°51'03.4"	++++			+++																	
14-11b2	Amphibolite	32°00'04.7"	59°31'01.8"	+++	++	(+)		+			+	+						+						
14-20	Amphibolite	32°17'31.4"	59°51'46.3	++++	+++	(+)		+++++				Ilm +	+		+	+	+				+	+		
16-43a	Amphibolite	32°17'33.0"	59°51'04.2"	++++	++	(+)	+	++	++												+			
16-86	Amphibolite	31°59'56.3	59°22'34.7"	++++	+++	(+)	+		+								+	+			(+)			
14-11b	Amphibolite	32°00'04.7"	59°31'01.8"	++++	+++	++	++	+	++	+		+					+	+						
14-26a	Amphibolite	32°02'09.9"	59°24'00.1"	+++	++	++	+	++			+				+	+								
14-26c	Amphibolite	32°02'09.9"	59°24'00.1"	+++	+	++	+	++	+	+	+	+						+						
17-18	Amphibolite	32° 2'13.08"N	59°24'1.02"E	++++	+++	++																		
14-07	Sediment	32°00'56.2"	59°33'19.0"					++++			+++	+					+							
14-23a	Sediment	32°01'08.9"	59°26'12.1"					+++				+			+++		+	+						++
16-80	Sediment	31°59'24.9"	59°29' 58.4"		(+)			+++							++		+	+++						++

Table 2

Location	Name	Size (km²)	Protolith ages (biostrat./radiometric)	Structural organization	Mantle lithology	Crustal Lithology	Chemistry	Intepretation	Metamorphism	Intepretation	Post-ophiolite magmatism	Oldest unconformable sediments	References
E CEIM	Sistan	20 000	124-106 Ma	Kilometer scale slices	Harzburgite	Gabbroic intrusion Pillowed or massive basalt	N-MORB E-MORB OIB CA	Mid oceanic ridge activity Enriched mantle SSZ	1) Amphibolite: 700°C-0.65GPa 74-72 Ma; Lws bearing metasediments: 250°C-0.4GPa 72 Ma 2) HP-LT rocks at 86 Ma	1) Metamorphic sole or lattéral equivalent 2) Subudtion	1) CA and adakite Upper Cretaceous 2) CA Eo-Oligocene 3) Alcaline Miocene	Eocene conglomerate or sandy-limestone	Delaloye et Desmons, 1980 Saccani et al., 2010 Zarrinkoub et al., 2012a Pang et al., 2012 Pang et al., 2013 This study
NW CEIM	Sabzevar Torbat-e-Heydarieh	7 000	Upper Jurrasic; 101-75 up to 52.4 (?) Ma	kilometer scale slices and colored mélange	Harzburgite Wherlite	Gabbro Dikes of diabase Basaltic lavas	N-MORB E-MORB OIB IAT CA	SSZ	1) Blueschist: 420-500°C 1.3-1.55 GPa 54-51 Ma; 2) Granulite: 780°C-1.1-1.2 GPa 105 Ma	1) Blueschist subduction related (age?) 2) Granulite: metamorphic sole	CA and adakite at 45 Ma (flare up?) High Silica Adakite at 58 Ma (partial melting of slab, age?)	Eocene Nummulitic limestone	Lindenberg et Groler, 1984 Ghazi et al., 2004 Nasrabady et al., 2011 Khalatbari Jafari et al., 2013 Moghadam et al., 2014 Rossetti et al., 2014 Moghadam et Stern, 2015 Omrani, 2017 Kazemi et al 2019 Mazhari et al., 2019
SW CEIM	Nain Ashin	600	145-67 Ma or older up to 188 Ma (?)	Small tectonic slices and colored mélange	Harzburgite Lherzolite Dunite	Gabbro Dikes of diabase Massive and pillowed basalt	N-MORB IAT CA	SSZ	Amphibolite 113 Ma	Metamorphic sole	CA Cenozoïc	Paleocene limestone	Sharkovski et al., 1984 Ghazi et al., 2004 Moghadam et al., 2009 Shirdashtzadeh et al., 2010, 2015, 2020 Moghadam and Stern, 2015 Pirnia et al., 2020
SW CEIM	Deshir Shahr-e-Babak	150	101-67	Small tectonic slices and colored mélange	Harzburgite Lherzolite Pyroxenite	Gabbro Dikes of diabase Massive and pillowed basalt	N-MORB IAT CA	SSZ			CA Cenozoïc	Maastrichtian limestone	Ghazi et al., 2004 Moghadam et al., 2009, 2010 Moghadam et Stern, 2015
SW CEIM	Balvard Baft Esfandagheh	3 000	103-72	Small tectonic slices and colored mélange	Harzburgite	Gabbro Dikes of diabase Basaltic lavas	E-MORB CA IAT	SSZ			CA Cenozoïc	Maastrichtian limestone	Moghadam et al., 2009, 2011, 2013 Moghadam et Stern, 2015
N Makran	Bad e Zeyarat Dar Anar	20 000	145-111	Kilometer scale slices	Harzburgite	Gabbro Dikes of diabase Pillowed basalt	N-MORB E-MORB	SSZ	Blueschist: 300-380°C 0.9-1.4 Gpa 100-95 Ma CCW PT path	Blueschist: cold subduction related regime after amphibolitic metamorphism		Maastrichtian limestone	Ghazi et al., 2004 McCall, 1997, 2002 Hunziker et al., 2015, 2017 Omrani et al., 2017 Burg, 2018 Sepidbar et al., 2020
N Makran	Fannuj Maskutan	2 800	<140	Kilometer scale slices	Lherzolite Harzburgite	Gabbro Dikes of diabase Basaltic lavas	IAT (S) E-MORB (N	SSZ				Maastrichtian limestone	McCall, 1997, 2002 Hunziker et al., 2015 Burg, 2018 Sepidbar et al., 2020

Supplementary Interactive Plot Data (CSV)

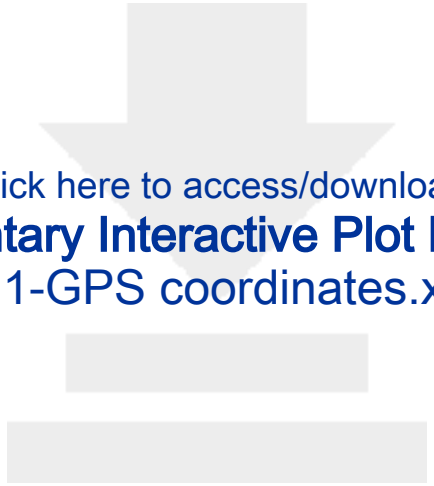

Click here to access/download

Supplementary Interactive Plot Data (CSV)

SM1-GPS coordinates.xlsx

Click here to access/download

Supplementary Interactive Plot Data (CSV)

SM2-chemistry.xlsx

Click here to access/download

Supplementary Interactive Plot Data (CSV)

SM3-pseudosections.xlsx

Declaration of interests

☒ The authors declare that they have no known competing financial interests or personal relationships that could have appeared to influence the work reported in this paper.

☐The authors declare the following financial interests/personal relationships which may be considered as potential competing interests:

Credit Author Statement

This piece of the submission is being sent via mail.